

**Improvement of hybrid supercapacitors
by optimization of electrode design and
material properties**

Dissertation

zur Erlangung des Grades

des Doktors der Naturwissenschaften

der Naturwissenschaftlich-Technischen Fakultät

der Universität des Saarlandes

von

Mathias Widmaier

Renningen

2018

Tag des Kolloquiums: 10.09.2018
Dekan: Prof. Dr. G. Kickelbick
Berichterstatter: Prof. Dr. V. Presser
Prof. Dr. F. Mücklich
Vorsitz: Prof. Dr. E. Arzt
Akad. Mitarbeiter: Dr. F. Soldera

Table of Content

Acknowledgments.....	iii
Zusammenfassung	v
Abstract.....	vi
1. Introduction	1
1.1 Lithium-ion Batteries	3
1.1.1 Cathode Materials for Lithium-ion Batteries	5
1.1.2 Anode Materials for Lithium-ion Batteries	8
1.2 Electrical Double-layer Capacitors	11
1.3 Hybrid Supercapacitors.....	14
2. Approach and Overview	19
3. Results and Discussion.....	24
3.1 Carbon as Quasi-Reference Electrode in Unconventional Lithium-Salt Containing Electrolytes for Hybrid Battery/Supercapacitor Devices	25
3.2 Influence of Carbon Distribution on the Electrochemical Performance and Stability of Lithium Titanate Based Energy Storage Devices	41
3.3 Valence-Tuned Lithium Titanate Nanopowder for High-Rate Electrochemical Energy Storage	59
5. Conclusions and Outlook	80
References	84
Curriculum Vitae	88

Acknowledgments

This thesis was carried out in the Cooperate Sector Research and Advanced Engineering in the Department of Functional Materials (CR/ARM) of the Robert Bosch GmbH in Renningen. It was prepared in close collaboration with the Saarland University and the Energy Materials Group at the Leibniz Institute for New Materials in Saarbrücken under the supervision of Prof. Dr. Volker Presser. The work was funded by the German Federal Ministry for Economic Affairs and Energy (BMWi) in support of the HyBaCap project (award number 03ET6113C). I acknowledge the support of the PhD program of the Robert Bosch GmbH.

I am deeply grateful to Prof. Dr. Volker Presser for supervising my work, his scientific guidance and for all the time spent during the numerous meetings, discussions, and emails throughout the last three years. He always managed to incorporate me into his team and encouraged me to take part in his exciting research, despite the large distance between our workplaces.

I thank Prof. Dr. Frank Mücklich for being my scientific supervisor, the valuable scientific discussions and advice throughout our meetings and that he reviews my thesis.

I am greatly indebted to my mentor and project leader Dr. Lars Bommer for his constant support proofreading of my thesis, and particularly for the productive and pleasant working climate throughout this project. I have learned a lot from him, and I will keep the team events he organized always in good memory.

I sincerely thank Dr. Christine Engel for her valuable input during our regular scientific discussions of my work. Her great experience in the field of electrochemical energy storage highly contributed to the success of this project.

I had the opportunity of working with the Energy Materials Group at the Leibniz Institute for New Materials. During my visits in Saarbrücken, I was always welcome in a highly motivated team, and I thank the entire Energy Materials Group for their support and the inspiring and fruitful discussions. Special thanks to Dr. Daniel Weingarth, Dr. Marco Zeiger, Dr. Soumyadip Choudhury, Dr. Mesut Aslan, Nicolas Jäckel, Simon Fleischmann, Anna Schreiber, Benjamin Krüner, Aura Tolosa, Juhan Lee, Hwirim Shim, and Pattarachai Srimuk.

In the past three years I have met and supervised a large number of students from all across the world, and we have worked together on this exciting topic. I am grateful for the help of all of you, and I thank Kristina Pfeifer, Severin Hahn, Tobias Schonhardt, Parviz Hajiyev, Murad Abuzarli, Claire Barras, Abbos Shodiev, Dianda Guo, Yu-Chuan Chien, Louis Lemarquis, Quentin Lamy and Thu Hien Tran for their support and their valuable contribution to the project.

I want to thank the HSC project team and all the people at the Robert Bosch GmbH who have supported me throughout the last years. Especially the following people I want to express my deepest gratitude: Dr. Jürgen Rapp, Dr. Thomas Wagner, Michael Donotek, Elisabeth Bühler, Veronika Haug, Dr. Pallavi Verma, and Dr. Thomas Eckl.

Many thanks to all the PhD students of the Robert Bosch GmbH I have met during this project. Special thanks to Andreas Gonser, Michael Wehle, and Heiko Gräbe.

I thank Dr. Anne Fuchs, Mario Tuchen, Ingrid Wührl, Dr. Christiane Müller, Monika Wessling and Dr. Thomas Köhler for their support with material characterization and the helpful discussions.

Most of all I thank my family and friends for all the support throughout my life. Thank you for everything.

Zusammenfassung

Lithium-Ionen-Akkumulatoren und Superkondensatoren haben sich zu unverzichtbaren Energiespeichertechnologien in der stetig wachsenden mobilen Elektrifizierung entwickelt. Bedingt durch die grundsätzlich unterschiedlichen Energiespeicherprinzipien, besitzen beide Technologien spezifische Vor- und Nachteile. Hybride Superkondensatoren kombinieren die Vorteile beider Technologien und sind daher in den letzten Jahren in den Fokus zahlreicher wissenschaftlichen Publikationen gerückt. In der vorliegenden Arbeit wurde ein Elektrodenhybridisierungsansatz untersucht, welcher auf einer optimierten und synergetischen Kombination von kommerziell erhältlichen Aktivmaterialien basiert. Durch gezielte Modifizierung der Elektrodenzusammensetzung und der Wahl der verwendeten Aktivmaterialien können die Zellen auf eine bestimmte Anwendung hin ausgelegt werden.

Der Fokus der Arbeit liegt auf der Referenzelektrodenentwicklung zur Charakterisierung von hybriden Superkondensatoren, dem Einfluss der Elektrodenmikrostruktur auf die elektrochemischen Eigenschaften und der Verbesserung der Ratenfähigkeit von hybriden Superkondensatoren durch Erhöhung der elektrischen Leitfähigkeit der Aktivmaterialien. Letzteres konnte durch eine Anpassung der Sauerstoffleerstellenkonzentration und des damit verbundenen Titan-Valenzzustandes von Lithiumtitanat erreicht werden. Dadurch wurde die Kohlenstoffkonzentration der Lithiumtitanat-Elektroden auf 5 Masse% verringert und gleichzeitig eine hohe Elektrodenkapazität von ca. 70 mAh/g (82 mAh/g bezogen auf Aktivmasse) unter extrem hohen C-Raten von 100 C erreicht. Durch Kombination dieser Elektroden mit Kompositelektroden aus Aktivkohle und Lithiummanganoxid konnten eine vielversprechende Energie- und Leistungsdichte von ca. 70 Wh/kg beziehungsweise 47 kW/kg erreicht werden (82 Wh/kg und 55 kW/kg bezogen auf Aktivmasse). Gleichzeitig konnte 83 % der Ausgangsenergie nach 5.000 Zyklen bei 10 C beibehalten werden (78 % nach 15.000 Zyklen unter 100 C).

Abstract

Lithium-ion batteries and supercapacitors have become indispensable energy storage devices for the steadily growing electrification. Both technologies possess unique advantages and disadvantages due to the inherently different energy storage principles involved. Hybrid supercapacitors (HSC) combine the advantages of the individual devices and have thus attracted considerable attention in recent years. In this thesis, electrode hybridization was investigated based on an optimized and synergetic combination of commercial lithium-ion battery and supercapacitor materials. This cost-effective approach is highly versatile since the electrode recipe can be precisely adjusted to a certain application via simple variation of the active material ratio or active material combination.

A special focus of this thesis was set on the reference electrode design for HSC characterization, the influence of electrode microstructure on the electrochemical performance and the improvement of the rate performance of hybrid supercapacitors via enhancing the electrical conductivity of the active material. The latter was achieved via adjustment of the oxygen defect concentration and the associated titanium valence state of lithium titanate. This enabled the reduction of the carbon concentration of lithium titanate electrodes to 5 mass%, while yielding a high electrode capacity of about 70 mAh/g (82 mAh/g normalized to the active mass) at ultra-high C-rates of 100 C. When combined with an activated carbon / lithium manganese oxide composite cathode, an excellent energy and power performance of 70 Wh/kg and 47 kW/kg, respectively, was obtained (82 Wh/kg and 55 kW/kg normalized to the active mass), while maintaining 83 % of its energy ratings after 5,000 cycles at 10 C (78 % after 15,000 cycles at 100 C).

1. Introduction

The improving living standards of industrial and emerging countries and the rapid growth of the world population have led to a continuously growing demand for electrical energy in today's society. Common energy sources, like oil and coal, are gradually depleting, while their usage is limited by more and more strict environmental legislation. Therefore, renewable energy conversion technologies, like solar cells or wind turbines, are crucial for a sustainable future. Since the energy output of these technologies is strongly fluctuating (e.g., during the night or during dead calm), the usage of electrochemical energy storage (ESS) devices becomes inevitable.[1] Moreover, the success of today's mobile electronics and the emerging electrification of motor vehicles is based on efficient EES devices.[2]

Conversion of chemical energy into electrical energy was explored centuries ago by Alessandro Volta in 1780.[3] Modern EES devices, like lithium-ion batteries (LIB) or electrical double-layer capacitors (EDLCs) have not been realized until the last decades. The first LIBs were commercialized in the 1990s by the Sony Corporation, while the first commercial successful EDLCs were produced by NEC during the 1970s with the license of SOHIO.[4] Both technologies are characterized by distinct electrochemical properties due to the inherently different energy storage principles involved. LIBs store charge via Li^+ intercalation/de-intercalation into host materials and associated reversible Faradaic reactions.[1] As opposed to this, the charge storage process of EDLCs involves ion electrosorption at the interface of high surface area electrodes and an electrolyte.[5] The different charge storage mechanisms also result in different electrochemical properties of both types of devices. A LIB is characterized by high specific energy, typically over 100 Wh/kg, a moderate specific power below 1000 W/kg (**Figure 1**) and a low cycle life of only a few thousand cycles with a limited depth of discharge.[3,5,6] An EDLC, in contrast, is a high power device with specific power over 10,000 W/kg and cycle life of millions of cycles (depending on the operation condition).[5] The resulting specific energy is relatively low and usually below 5 Wh/kg.[5]

An ongoing task is the combination of the advantages of both technologies to outweigh the main drawbacks of the individual device. One of the first considerations of combining high power and high energy EES devices were done by David Vincent Ragone (name giver of the so-called Ragone Plots) in 1968.[7] Most combinations were made on an external level, by the hardware connection of a conventional EDLC with a lead acid battery or a LIB. The main

outcomes are: The size of the battery can be reduced [8,9], enhanced cycle life (especially for pulsed applications),[10,11] and a broader operating temperature range [10] compared to the battery alone. These ways of external hybridization have a drawback owing to the electrochemical nature of the two different devices: A conventional LIB is normally used at a narrow potential range of 3-4.2 V, while an EDLC is typically cycled over a large range of 0-2.7 V.[12] To compensate this voltage mismatch, complex serial or parallel connections of multiple EDLCs and LIBs and supplementary control electronics have to be utilized.[12]

These drawbacks can be resolved by combining LIB and EDLC materials in a single device. Such devices are generally referred to as hybrid supercapacitors (HSCs) and were first proposed by Amatucci et al.[13] in 2001. In this work, an asymmetric HSC was constructed by combining an EDLC cathode with a LIB anode. Since then, HSCs have attracted considerable attention in the scientific community, and several material combinations have been proposed.[14–22] Additionally, it was observed that such combinations could lead to beneficial synergistic effects between both material classes since the EDLC material (carbon) can significantly enhance the electrode conductivity and act as a shock absorber for high currents.[15,20]

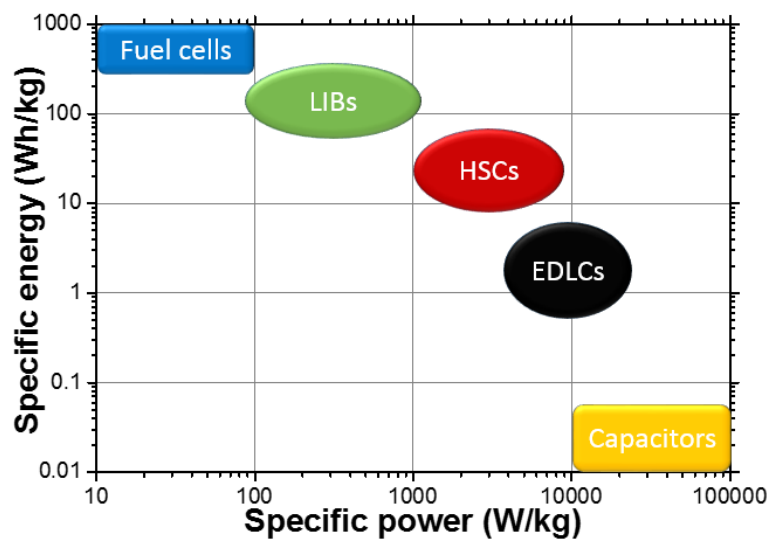


Figure 1: Ragone-chart of energy storage devices based on entire cell mass (adapted from Ref. [5,6,23]).

The HSC technology is still in an early stage of development, with only limited commercialized applications.[24] Only a few companies like JM Energy, FDK, NCC, or Yunasko have recently started to produce HSC devices.[5,25] Commercial/prototype HSC cells usually possess a higher specific power and cyclability as compared to LIBs (up to 10 kW/kg and several

thousand cycles), while simultaneously delivering higher specific energy as compared to EDLCs (between 10-30 Wh/kg).[5,25] Possible application areas of HSCs are start/stop coasting coupled with recuperation systems or as a high power component for electrical vehicles. Additionally, the scope of HSC applications may extend to stationary power supplies, wireless sensor nodes, windmills, electric busses, and trams.

This thesis aims to establish a deeper understanding of the cell chemistry to improve HSCs concepts and further advance this technology towards commercialization. Special attention will be given to proper reference electrode design for HSC electrode characterization, detection and prevention of rate limitations and the influence of the electrode microstructure on the electrochemical performance. This chapter will introduce basic principles and the state-of-the-art of LIBs, EDLCs, and HSCs.

1.1 Lithium-ion Batteries

The concept of lithium-based batteries was first introduced during a conference talk by Chilton Jr. and Cook at the Electrochemical Society fall meeting in Boston in 1962.[26] Since then, this technology has been constantly refined, particularly by Armand,[27] Goodenough,[28] and Lazzari & Scrosati,[29] until the first modern lithium-ion battery was commercialized by Sony in 1991.[3,24] State-of-the-art LIBs use a graphite negative electrode and a lithium-containing transition metal oxide (e.g., LiCoO_2 , LiMn_2O_4 or LiFePO_4) as the positive electrode.[3] In the following, the negative electrode will be referred to as the anode, while the positive electrode will be referred to as the cathode. Note that this definition should not be confused with general electrochemistry nomenclature (i.e., the anode is the electrode where oxidation takes place, and the cathode is the electrode where the reduction takes place) since anode and cathode would reverse their position in this case during cell charging and discharging. In state-of-the-art LIB nomenclature “anode” and “cathode” have become synonyms for “negative electrode” and “positive electrode” and are being used in this context for brevity.

Both electrodes are kept at a distance by a separator soaked with an organic electrolyte (Li-salt dissolved in an organic solvent) to prevent an electrical short. During charging, a current flows between the electrodes, leading to the oxidation of the transition metal in the cathode and the de-intercalation of Li-ions from the cathode into the electrolyte (**Figure 2A**).

Simultaneously the anode material (e.g., graphite) is reduced while it intercalates Li-ions from the electrolyte into its lattice (**Equation 1**). The quantity of passed electrons/charge is proportional to the yield of the electrochemical reaction and follows Faraday's laws of electrolysis.[30] By definition, such reactions are defined as Faradaic reactions and LIB materials are often referred to as Faradaic charge storage materials.[30] During discharging all processes are reversed (transition metal reduced, anode material oxidized) leading to the flux of electrons from anode to the cathode (**Figure 2B** and **Equation 2**).[3,31]

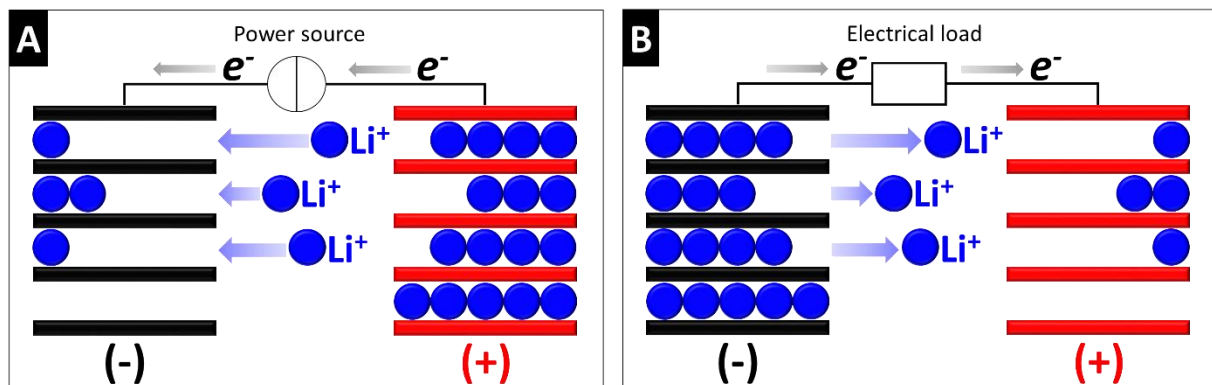


Figure 2: Schematic operating principle of a LIB during charging (A) and discharging (B). The movement direction of electrons " e^- " and Li-ions is indicated by the colored arrows (adapted from Ref. [32]).

In case of a graphite anode and a layered transition metal oxide cathode, these processes can be expressed by the following equations:



where M is a transition metal (e.g., Mn, Co, Fe, or Ni). The transfer of Li-ions from the cathode to the anode during charging increases the voltage difference between both electrodes. This difference is caused by the higher chemical potential of Li-ions contained in the anode as compared to the cathode.[24,33] Both effects, the transfer of charge via Li-ion/electron migration and the associated polarization between the electrodes, determines how much electrical energy can be converted into chemical energy during cell charging. Accordingly, the specific energy E (energy per mass) reads:[3]

$$E = Q\bar{V} \quad (3)$$

where Q is the transferred charge per mass and \bar{V} is the average potential between anode and cathode. In the following, this charge will be referred to as capacity according to the common LIB nomenclature.[3] The theoretical gravimetric capacity Q (charge per mass) that can maximal be stored inside the bulk of the active material is given by Faraday's first law of electrolysis:

$$Q = \frac{zeN_A}{M} \quad (4)$$

where z is the amount of lithium intercalated/de-intercalated per formula unit, e is the elementary charge, N_A is the Avogadro constant and M is the molecular weight of one formula unit. Accordingly, materials which intercalate large amounts of Li-ions (i.e., possess high Q) at a high polarization are generally preferred to obtain high energy (**Equation 3-4**).

1.1.1 Cathode Materials for Lithium-ion Batteries

The cathode of a conventional LIB is the source of Li-ions since the cells are assembled in a discharged state with Li-free graphite as an anode.[33] Li-ion-containing transition metal oxides remain at the focal point of LIB cathode material application since LiCoO_2 was first introduced in the groundbreaking study of Mizushima et al. in 1980.[28] The enormous scientific effort during the subsequent decades resulted in the discovery of a wide variety of alternative cathode materials with distinct electrochemical properties (e.g., cycling stability, capacity, lithiation/de-lithiation plateau). These materials can be classified according to the crystal structure and chemical composition into layered LiMO_2 , olivine LiMPO_4 , spinel LiM_2O_4 , silicate Li_2MSiO_4 , tavorite LiMPO_4F , and borate LiMBO_3 compounds (where M can be Co, Ni, Mn, Fe, or V).[33] While most of the cathode materials possess unique features, only a few are characterized by a well-balanced electrochemical performance all across the board and have reached commercial status today. Since these cathode materials are also most promising for hybridization, only these will be discussed in the following.

Lithium cobalt oxide (LiCoO_2 , LCO) has a layered crystal structure with 2D Li-ion diffusion paths and was the first commercially used cathode material for LIBs.[3] Electrochemical extraction of Li-ions from the LCO structure leads to a voltage plateau at 4 V vs. Li/Li^+ attributed to the redox pair $\text{Co}^{4+}/\text{Co}^{3+}$ (**Figure 3**).[3] It is generally possible to de-intercalate almost all Li-ions from the LCO structure and consequently reach the theoretical capacity of 274 mAh/g. Even

after almost three decades of extensive research, the capacity of this material has remained limited to about 140 mAh/g for practical applications.[3,33] This is because of structural instabilities of the crystal lattice after Li-ion extraction beyond a critical limit since excessive de-lithiation leads to oxygen release from the material.[3,34] The liberated oxygen can then further exothermically react with the organic electrolyte and lead to the ignition or explosion of the cell.[3,34]

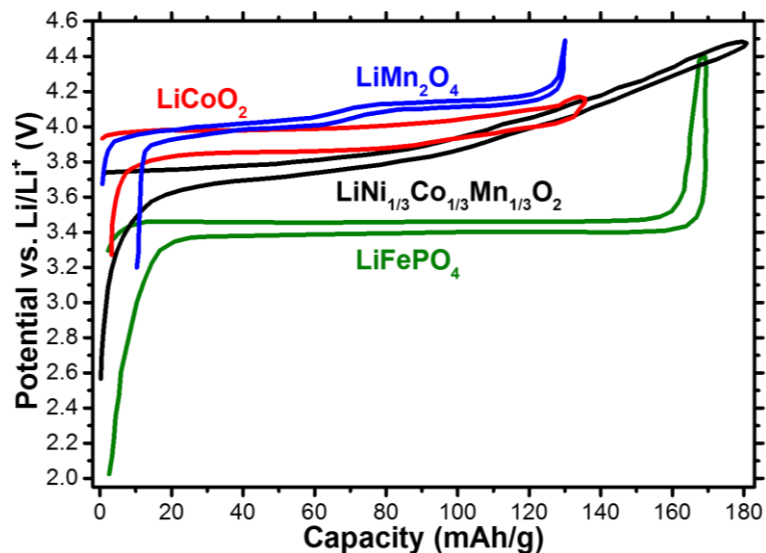
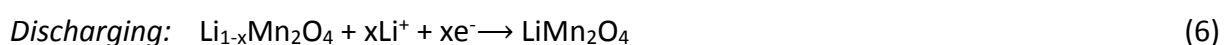
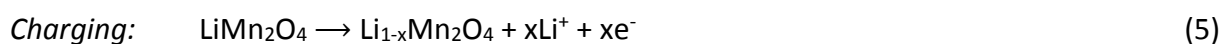


Figure 3: Characteristic charging/discharging curves of the most important positive electrode materials LMO, LCO and LFP vs. Li/Li⁺ at 20 °C and C/5 (data of curves from Ref [35] and [3]).

Follow-up work on layered compounds studied Ni- and Mn-ion-containing LCO derivatives to improve the safety of the cells and to decrease the overall amount of expensive Co.[3,33] This research gave rise to the development of LiNi_{1/3}Co_{1/3}Mn_{1/3}O₂ (NCM) and similar compounds, which are widely used in today's state-of-the-art LIBs.[3] Similar to LCO, NCM possesses a layered structure with 2D Li-ion diffusion channels.[3] The de-lithiation of NCM leads to a sloped voltage profile at 3.8-4.3 V vs. Li/Li⁺ due to the sequential oxidation of Ni²⁺ to Ni³⁺, Ni³⁺ to Ni⁴⁺, and finally Co³⁺ to Co⁴⁺ (**Figure 3**).[3,33] Manganese-ions are electrochemically inactive and are solely incorporated to stabilize the crystal structure and to improve the electrochemical cycling stability.[3] The NCM structure is more resilient to de-lithiation, leading to improved practically usable gravimetric capacities of up to 160 mAh/g (theoretical value 274 mAh/g).[3] Nevertheless, oxygen release at a high degree of de-lithiation cannot fully be avoided and is still a major safety concern for NCM-based LIBs.[3] Since most HSCs applications impose abusive conditions to the cells (e.g., high currents) and the used

electrolyte (i.e., acetonitrile) is highly flammable, LCO and derivatives thereof were not studied in this thesis.

A safer alternative to layered transition metal oxides is lithium iron phosphate (LiFePO₄, LFP). This material was first proposed by Padhi et al. in 1998,[36] has an olivine crystal structure and a voltage plateau at about 3.4 V vs. Li/Li⁺ due to the redox couple Fe²⁺/Fe³⁺ (**Figure 3**).[3] The theoretical capacity of LFP upon complete Li⁺-extraction is 170 mAh/g.[37] Since LFP exhibits no oxygen evolution and no exothermic effects during charging/discharging, it allows full de-lithiation without the risk of cell ignition or explosion.[3] Additionally, LFP is not toxic, cheaper as compared to LCO or NCM and has an excellent cycle life of several thousand cycles.[3] The high cycle life is attributed to the stability of the delithiated phase (FePO₄) and the low volume difference of about 7 vol% between the lithium rich and lithium poor phases.[3] Nevertheless, the low de-lithiation plateau position decreases the overall cell voltage and thus the specific energy (**Equation 3**). Additionally, the 1D Li-ion diffusion paths and the low electrical conductivity can severely deteriorate the rate performance and generally limit the practical capacity of LFP to about 100-110 mAh/g.[36] To circumvent these limitations, the use of nanosized electrode material particles and carbon coatings have been proposed to decrease the solid Li-ion diffusion paths and increase the electrical conductivity, respectively. Such nanocomposites can enable gravimetric capacities of up to 165 mAh/g.[3] Another promising alternative to LCO and NCM is lithium manganese oxide (LMO, LiMn₂O₄). This material was first introduced as possible LIB cathode by Thackeray et al. in 1983,[38] is not toxic, less expensive, and safer as compared to LCO/NCM.[39] LMO has a spinel crystal structure with a three-dimensional network for Li-ion diffusion.[3] These cross-linked Li-ion diffusion channels allow fast Li-ion extraction/insertion kinetics and enable a superior high-rate performance as compared to LCO or LFP.[3,24] During de-lithiation Mn³⁺ ions are oxidized into Mn⁴⁺ in a voltage range of 3.8-4.25 V vs. Li/Li⁺ (**Figure 3**). This leads to the following electrochemical reaction during charging and discharging:



The theoretical capacity of LMO upon entire Li⁺-extraction is 148 mAh/g.[40] Nevertheless, only 0.8 Li⁺-ions per formula unit can be maximally extracted, which corresponds to a specific capacity of about 120 mAh/g.[41] The main drawback of LMO is its high capacity fading during

cycling, especially at elevated temperatures of about 50 °C.[3,31] This fade was well investigated in literature and several failure mechanisms were proposed: (i) Fracture of the LMO surface in deeply discharged cells caused by a Jan-Teller distortion,[42] (ii) dissolution of Mn-ions into the electrolyte,[43,44] or (iii) the oxidation of the electrolyte at the LMO surface.[45] The latter two have an important implication for the conventional particle-size-reduction-approach of high power concepts since the area for side reactions (i.e., surface area) increases with shrinking particle size. Accordingly, nanosizing of LMO particles can have a detrimental effect on the cell lifetime and has to be considered with caution.[24]

1.1.2 Anode Materials for Lithium-ion Batteries

Initially, lithium metal foil was used as the anode for the first lithium-based secondary batteries due to its high gravimetric capacity of 3860 mAh/g and its low reduction voltage.[3,46] This anode was then abandoned due to the poor cycle life and lithium dendrite growth, which can lead to a short-circuit and a thermal runaway of the cells.[3] The risk of lithium dendrite formation is drastically reduced when replacing the lithium metal by an intercalating anode material like graphite[26] or lithium titanate ($\text{Li}_4\text{Ti}_5\text{O}_{12}$, LTO)[47]. Graphite is by far the most widespread anode material in state-of-the-art LIBs. This is due to its high capacity of about 370 mAh/g and low Li-ion intercalation potential below 0.3 V vs. Li/Li^+ (**Figure 4**). Such a low Li-intercalation potential exceeds the electrochemical stability of all organic electrolytes, which start to decompose at potentials below about 0.8 V vs. Li/Li^+ (**Figure 4**).[48]

Reliable cycling performance of conventional LIBs is only possible when passivizing the graphite surface by formation of the so-called solid electrolyte interphase (SEI).[48] The SEI is a Li-ion permeable surface layer which is formed during the first charge/discharge cycles of the cell and consists of organic and inorganic electrolyte decomposition precipitates.[48] Further electrolyte decomposition can largely be avoided since the SEI is electrically insulating.[48] Conventional LIBs are generally limited to carbonate-based electrolytes, which are known to form a stable and dense SEI.[49] Additionally, multiple electrolyte additives (e.g., vinylene carbonate, fluoroethylene carbonate, or lithium bis(oxalate) borate) are needed to modify the chemical composition of the SEI and to improve the electrochemical cycling stability of graphite based cells.[50] The high charge transfer resistance of the SEI and the

generally low ionic conductivity of carbonate-based electrolytes can impair the electrochemical kinetics and the rate performance of the cells.[51]

Anode materials, which operate within the electrochemical stability boundary of organic electrolytes are promising for high rate application since SEI formation can be avoided and highly Li-ion conductive electrolytes become accessible (e.g., Li-salt containing acetonitrile). The most important example of such a high-voltage anode is LTO with a voltage plateau at about 1.55 V vs. Li/Li⁺ (**Figure 4**). While the high lithiation potential of LTO effectively circumvents SEI formation, it also decreases the specific energy compared to a graphite electrode.[3] Therefore, commercial LTO-based cells are mainly limited to niche applications which require a high power performance.

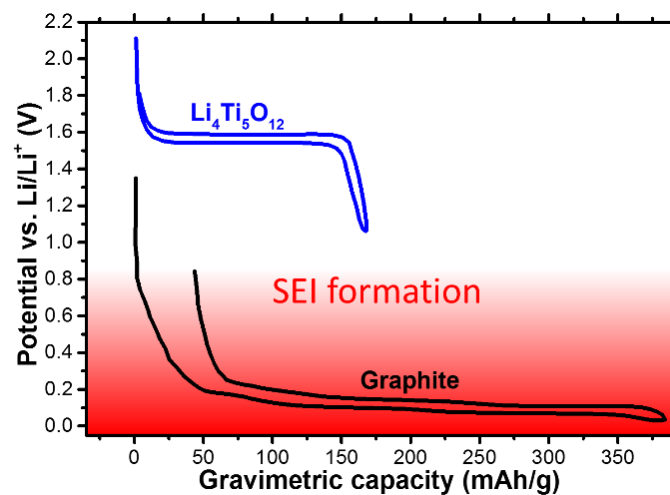
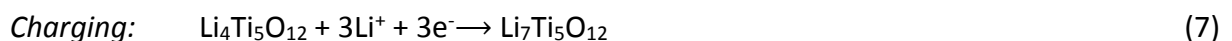


Figure 4: Charging/discharging curve of LTO and graphite vs. Li/Li⁺ at 20 °C and C/20 (data from Ref. [35])

LTO is characterized by several properties like inherent safety,[52] high Coulombic efficiency,[47] negligible volume expansion during lithiation,[47] and the cost-attractive raw materials for synthesis [53]. The Li-intercalation reaction takes place according to the following reaction:



The theoretical capacity of LTO is 175 mAh/g, and practical values of about 160 mAh/g can be achieved for commercial materials.[54] According to the Gibbs phase rule, the constant voltage plateau of LTO indicates that two separate phases must be present during lithiation

since the electrochemical potential (i.e., the potential of the anode) is fixed Li-ion insertion/extraction.[55] This so-called two-phase lithiation/de-lithiation mechanism assumes the simultaneous existence of a Li-poor ($\text{Li}_4\text{Ti}_5\text{O}_{12}$) and a Li-rich ($\text{Li}_7\text{Ti}_5\text{O}_{12}$) phase, sharply separated by a physical phase boundary.[55] By contrast, the de-lithiation of cathode materials like LCO, NCM, or LMO is carried out by cumulative Li-ion depletion of a single phase (solid-solution mechanism) as can be deduced from their sloped voltage profiles (**Figure 3**). The two-phase mechanism of LTO is supported by electron microscopic studies of partially lithiated LTO.[56] During lithiation, the Li-rich phase is initially formed at the outer shell of the LTO particles according to the core-shell model of Takami and co-workers (**Figure 5**).[57] With continued lithiation, the Li-rich phase propagates further into the particle, thereby transforming the entire particle into the Li-rich phase. During de-lithiation, the Li-rich phase is transformed into the Li-poor phase according to the same principles.

The low intrinsic electronic conductivity of $\text{Li}_4\text{Ti}_5\text{O}_{12}$ (10^{-13} S/cm) impairs the Li-ion intercalation/de-intercalation reactions of LTO-based cells.[58] Substantial experimental efforts have been devoted to increasing the electronic conductivity of LTO anodes, for example by adding conductive carbon into LTO electrodes. In this context, a variety of LTO-carbon nanocomposites have been proposed, such as LTO confined in nanopores of activated carbon (AC),[59] or LTO-grafted on carbon nanotubes,[60–64] carbon nanofibers,[53,65–67] or graphene.[68–72] LTO-doping is another effective way to improve the intrinsic electronic conductivity of LTO, for example with Cu^{2+} ,[73] Mg^{2+} ,[74] Zn^{2+} ,[75] Fe^{3+} ,[76] Cr^{3+} ,[77] Al^{3+} ,[78] Sn^{4+} ,[79] Zr^{4+} ,[80] Ta^{5+} ,[81] V^{5+} ,[82] Nb^{5+} ,[83] or W^{6+} [84]. Such doping elements have been reported to reduce a fraction of Ti^{4+} to Ti^{3+} and increase the overall electron concentration.[85]

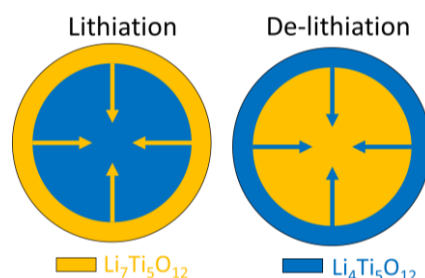


Figure 5: Simplified core-shell model of the spatial positioning of the present two phases in an LTO particle during lithiation and de-lithiation according to Takami et al. [57]. The propagation direction of the respective phase is indicated by the colored arrows. Copyright by Elsevier, reprinted from Ref. [22] with permission.

At temperatures exceeding 50 °C, LTO-based cells are reported to display severe swelling effects originating from gas evolution at the LTO anode.[86–90] Up to now the root cause of this gas evolution is blurred and several mechanisms have been proposed: i) Electrochemical decomposition of trace water and electrolyte decomposition catalyzed by trace water,[87] ii) electrochemical electrolyte decomposition catalyzed by the LTO surface,[88] iii) intrinsic electrochemical electrolyte decomposition caused by the low potential and the temperature independent of the electrode material,[90] and iv) continuous electrolyte decomposition during cycling due to ineffective passivation of the LTO surface.[86]

1.2 Electrical Double-layer Capacitors

A conventional EDLC is constructed by two porous carbon electrodes, which are separated by a separator soaked with an electrolyte. When a current is applied between both electrodes, the accompanied voltage difference causes a net diffusion of positively charged electrolyte ions to the negative electrode, while negatively charged species migrate to the positive electrode (**Figure 6A**).[91] The ions are physically adsorbed at the electrodes and their charge is counterbalanced by electrons (negative electrode) respectively holes (positive electrode).[91] According to the Helmholtz model, ions and their respective countercharge (electrons or holes) are accumulated in the vicinity of the electrode surface in a static, few nanometer thick layer, the so-called electrical double-layer.[91] During discharging, these processes are reversed, leading to the flux of electrons from the negative electrode to the positive electrode, while ions diffuse into the electrolyte (**Figure 6B**). This energy storage mechanism does not involve Faradaic reactions or solid-state diffusion, occurs rapidly, and is highly reversible. Because of these reasons, EDLCs can be charged much faster (higher specific power) and have superior cycle life compared to batteries.[6]

The energy storage principle of an EDLC is like the one of a parallel plate capacitor (energy storage through charge separation). On first approximation, the same equations can be applied to calculate the capacity and energy of the device.[23,92,93] With two electrical double-layers being formed (one on each electrode), the overall capacitance C (measure of a capacitor's ability to store an electrical charge) results after simple series connection of two capacitors in the following expression:[91]

$$\frac{1}{C} = \frac{1}{C_1} + \frac{1}{C_2} \quad (9)$$

where C_1 and C_2 are the capacitances of the first and second electrode respectively. The capacitance of one electric double layer C^* (C_1 or C_2) can be expressed as:

$$C^* = \frac{\epsilon_r \epsilon_0}{d} A \quad (10)$$

where ϵ_r is the electrolyte dielectric constant, ϵ_0 is the permittivity of vacuum, d the charge separation distance (thickness of the electrical double-layer), and A the electrode surface area accessible for electrolyte ions. The energy E is given by:

$$E = \frac{1}{2} C U^2 \quad (11)$$

where U is the potential window of the cell. The energy ratings are improved compared to a parallel plate capacitor because the area for charge accumulation is much higher and the charge separation distance is smaller (high A and low d , **Equation 10**).

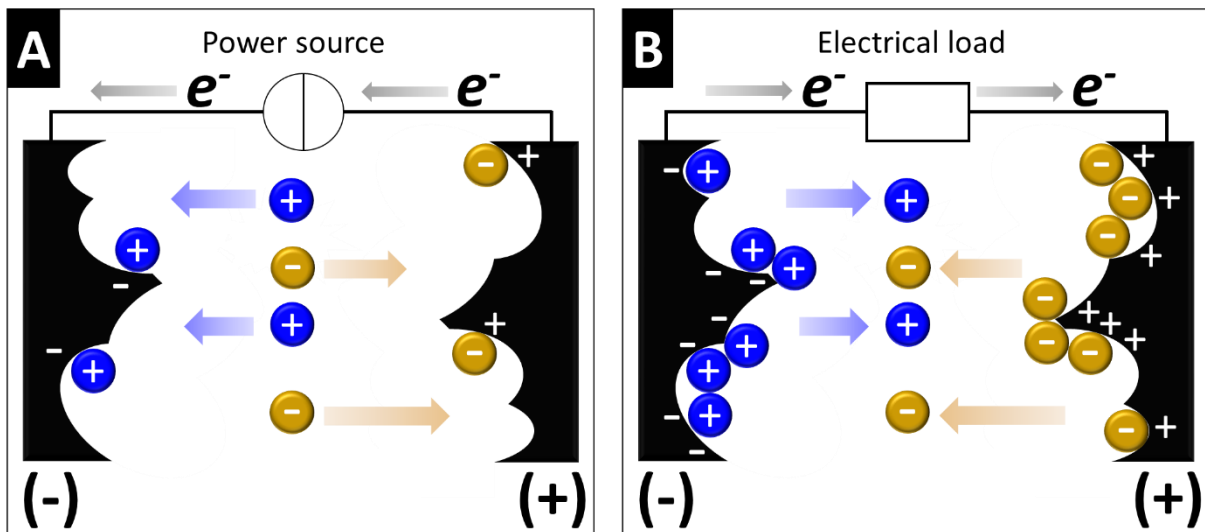


Figure 6: Schematic operating principle of an EDLC during charging (A) and discharging (B). The movement direction of electrons " e^- " and Li-ions is indicated by the colored arrows (adapted from Ref. [6]).

An ideal EDLC with no resistive losses would deliver the complete stored energy, independent of the discharging rate. However, a real EDLC is discharged with increasing discharging rates will show a fading of the recoverable/storable energy. This fading is caused by the equivalent series resistance (ESR) of the EDLC. The ESR is a complex combination of different parallel and serial contributions like particle-particle resistance, contact resistance, and/or ionic resistance of the electrolyte and the separator.[5] At match impedance, when the ESR is equal to the

resistance of the electrical load (connected between both poles to discharge the cell), the specific power decreases, even though the discharging rate is increased. At this point the supercapacitor possesses its highest power P_{max} while coinstantaneous delivering only half of the stored energy [5,94]:

$$P_{max} = \frac{U^2}{4R_s} \quad (12)$$

where U is the applied voltage and R_s is the ESR of the EDLC.[5]

The most important requirements of the active material for an EDLC is a large surface area accessible to ions and high electronic conductivity. Both of these requirements can be matched by using high porous carbons since carbon is electrically conductive and one of the most structural versatile elements in the world.[91] The tremendous research efforts in the last years gave rise to the development of a vast number of different carbon materials like AC,[95,96] onion-like carbon,[97] templated carbon,[98] carbon nanotubes,[99] carbon aerogels,[100] or graphene[101].

Today, ACs are the primarily commercially used carbon active material for EDLCs due to their large specific surface area (1000-3000 m²/g), good electrical conductivity, and cost efficiency.[5,91] These carbons are derived through a carbonization-activation process of carbon-rich precursors like coconut shells, wood, pitch, or synthetic polymers.[102] This carbonization/activation process leads to the development of highly porous AC materials containing a network of macropores (>50 nm), mesopores (2-50 nm), and micropores (<2 nm).[91] The mesopores and macropores act as transportation channels for ion diffusion from the electrolyte bulk to the electrode-electrolyte interface, whereas micropores are responsible for ion electrosorption and the associated charge storage.[103] Accordingly, the pore size distribution of the AC highly impacts the performance of the EDCL and needs to be carefully adjusted.[91] The latter applies in particular to careful matching of the pore structure to the size and mobility of anions and cations (including different optimum parameters for the positive and negative electrode).

Since EDLCs are generally operated within the electrochemical stability boundaries of the electrolyte, elaborate SEI engineering can be avoided, and a wide variety of electrolytes can be applied. Electrolytes for EDLCs can generally be divided into systems with aqueous and organic solvents or neat ionic liquids. Aqueous electrolytes provide a high conductivity

combined with high safety and low cost.[5] Yet, their low potential window limits their industrial usability, since the energy and the specific power both depend on the cell voltage (**Equation 11-12**).[104] While ionic liquids may provide high electrochemical stability windows above 3 V, the low ionic conductivity and high price generally is insufficient for most applications.[5,105] By contrast, organic electrolytes offer a high electrochemical stability window of up to 2.7 V and a superior conductivity as compared to ionic liquids.[5,105] Nowadays, commercial supercapacitors are commonly operated with organic electrolytes (e.g., tetraethylammonium tetrafluoroborate salt dissolved in acetonitrile or propylene carbonate).[5]

This distinct difference between Faradaic Li-ion intercalation and capacitive charge storage mechanisms is only a simplistic image and does not include pseudocapacitive charge storage. Alike for LIBs, pseudocapacitive charge storage originates from reversible Faradaic reactions at the surface or in the volume of the active materials. These processes are, however, extremely fast and generally not distinguishable from EDLC materials in their electrochemical signature (e.g., charge/voltage profiles).[106] Typical pseudocapacitive materials are metal oxides (e.g., ruthenium oxide or birnessite-type MnO_2), transition metal dichalcogenides, transition metal carbides, and conducting polymers (e.g., polyaniline).[107] Pseudocapacitance can also originate from heteroatoms (especially oxygen and nitrogen) contained in surface groups of AC [108] or be provided by the electrolyte [109]. It remains important to label materials and electrodes only pseudocapacitive if i) the energy storage and recovery mechanism is not dominated by electrical double-layer formation, and ii) the observed charge/discharge behavior truly is capacitor-like (i.e., no battery-like behavior with pronounced redox peaks).

1.3 Hybrid Supercapacitors

Hybrid supercapacitors aim to combine the advantages and energy storage principles of LIBs and EDLCs in one device (i.e., high cycle life, specific energy and power) and were first introduced 2001 in a pioneering study of Amatucci et al.[13] In this work, HSCs were constructed by combining an AC cathode with a LTO anode (**Figure 7C**, left side). During charging, an electrical double-layer forms at the AC-electrolyte interface (EDLC charge storage mechanism), while Li-ions diffuse from the Li-ion containing electrolyte and intercalate into

the crystal structure of LTO (LIB charge storage mechanism). It is generally conceivable to reverse this electrochemical setup and construct an HSC with a LIB positive electrode and an AC negative electrode (**Figure 7C**, right side). However, such a concept is not popular due to the associated lower cell voltage in this case.[110] In the following, the electrochemical setup will be referred to as asymmetric HSC, whereby one electrode exclusively stores charge via ion electrosorption and one electrode exclusively stores charge via Faradaic Li-intercalation reactions (**Figure 7B**). The best-known example of an asymmetric HSC is the so-called lithium-ion capacitor (LIC). These devices are already commercially available and employ graphite anodes and AC cathodes in a carbonate-based organic electrolyte.[5] Since the graphite anode of LICs is operated outside of the electrochemical stability window of organic electrolytes, the operating voltage of LIC is drastically enhanced to about 4 V.[110,110] Similar to conventional LIBs, a stable SEI at the anode surface is required to prevent a continuous electrolyte decomposition. In case of LICs, the occurring irreversibly Li-loss during SEI formation cannot be compensated by a higher cathode loading, since the AC cathode does not contain Li-ions (in contrast to LIBs). Therefore, pre-lithiation of the graphite anode is mandatory to prevent Li-ion depletion of the electrolyte during SEI formation.[110,111] Such a pre-lithiation is usually carried out with a sacrificial Li-metal electrode and requires elaborate current collector pretreatment (i.e., defined perforating) and/or complex formation cycles.[5,110] All these factors negatively affect the cost-effectiveness of LICs and therefore limit its attractiveness for a wider range of applications. Cell concepts based on low voltage anodes and associated SEI formation are not part of this thesis.

Hybridization can also be realized by combining Faradaic charge storage and highly porous carbon materials within the same electrode. This electrode hybridization can be accomplished according to two inherently different approaches: Hybrid materials or composite electrodes. In the former case Faradaic energy storage materials are directly deposited during material synthesis onto AC,[59] carbon nanotubes,[60–64] carbon nanofibers,[53,65–67] onion-like carbons,[112] or graphene.[68–72] For this purpose, several synthesis routes were proposed like wet processes,[112,113] atomic layer deposition,[114,115] electrochemical deposition [116,117] or drop casting.[118] Generally, the carbon substrates can be divided into endohedral and exohedral carbons. Endohedral carbons are porous materials with their surface area primarily located inside of the particles (e.g., AC), while exohedral carbons are non-porous nanomaterials with surface area localized at the particle outer surface (e.g.,

carbon onions, closed-capped carbon nanotubes, or graphene).[119] The carbon substrate increases the electronic conductivity and provides a large surface area for ion electrosorption and a large solid-electrolyte interface (beneficial to decrease the diffusion distance of Li-ions in the solid phase). Simultaneously the capacity/energy is enhanced by the Faradaic charge storage material.

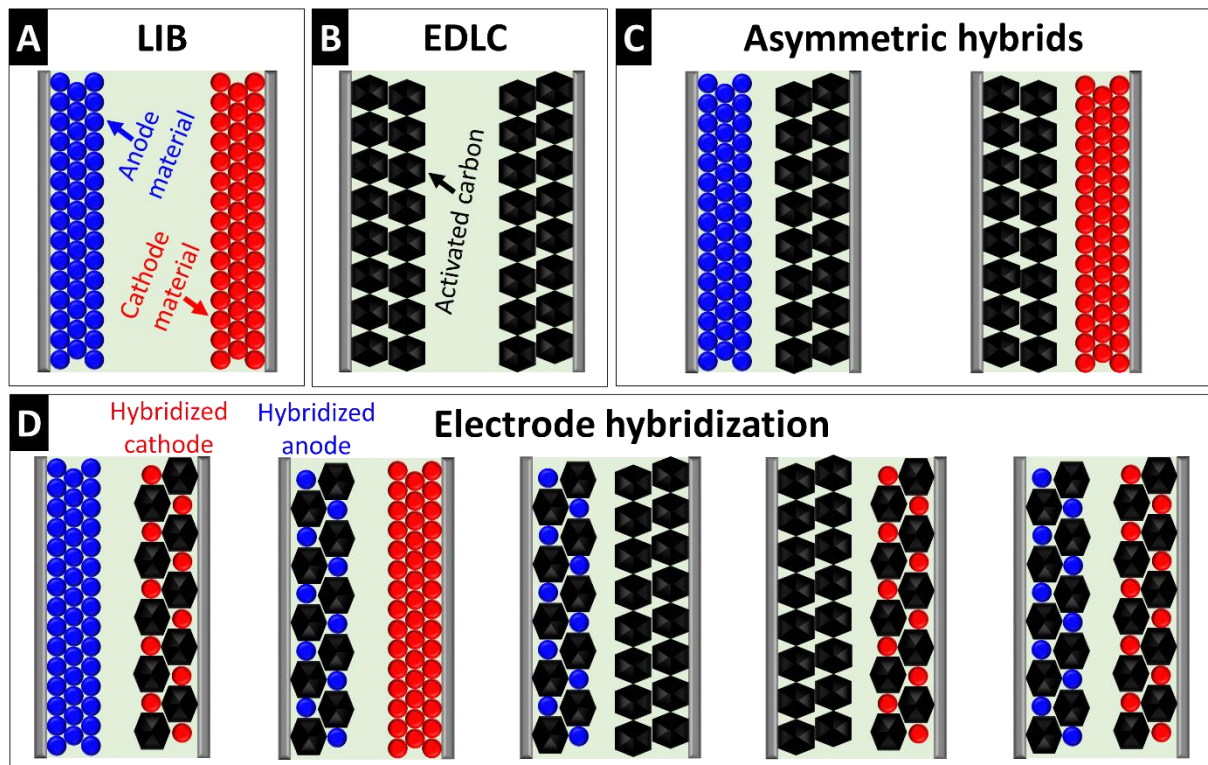


Figure 7: Schematic examples of a LIB (A), EDLC (B), asymmetric hybrid (C) and hybridization of the electrode (D). Anode/cathode LIB active material particles are indicated by blue/red spherical particles, while AC is depicted as regular black hexagons.

The hybrid material approach allows precise control of the electrochemical performance by modifying the process parameters and/or the used materials and to tune the charge storage mechanisms as was previously demonstrated by Fleischmann et al. [112]. There is a risk of blocking the surface area and internal pores of the carbon substrate (especially in case of endohedral carbons) for high loadings of Faradaic charge storage materials.[113] Additionally, efficient synthesis processes and protocols, which are already established and optimized for large-scale production of commercial materials, have to be altered and precisely adjusted for the production of novel hybrid materials. This is usually connected to several time-consuming and costly upscaling phases and preferably avoided from an industrial point of view.

Electrode hybridization can also be achieved by combining commercial LIB materials and AC within the same electrode by mechanical mixing (**Figure 7D**). Such composite electrodes largely avoid pore blocking of the AC, while being based on cost-effective commercially available materials. These electrodes have attracted considerable interest in the scientific community, and several material combinations have been proposed.[14–21] It is possible to hybridize both electrodes simultaneously or to combine one composite electrode with either a LIB or an EDLC electrode (**Figure 7D**). Hybrid devices based on such composite electrode systems are highly versatile and can be adjusted to a certain application by optimization of the electrode recipe (via variation of active material ratio or active material combination). For example, high power applications might require higher amounts of AC to increase the overall amount of charge stored via fast ion electrosorption. By contrast, if a higher specific energy is desired, the LIB material concentration of the electrodes should be increased. This simplified picture is only partially valid as will be shown in the subsequent sections.

The electrochemical signature of a composite electrode is the superposition of EDLC and LIB contributions, weighted with their respective mass fraction (**Figure 8**).[16,18] For example, during charging at constant current, a LIB electrode will show a voltage plateau at a certain voltage, while an EDLC shows a linearly sloped potential curve over the entire charging range.[16,18] Accordingly, the charge/discharge profile a composite electrode exhibits a voltage plateau caused by Faradaic Li-intercalation of the LIB material, and additionally a sloped area due to double layer formation at the AC-electrolyte interface.[16,18] When polarizing with a constant voltage ramp, for example during cyclic voltammetry experiments, similar considerations can explain the electrochemical behavior of composite electrodes (**Figure 8F**).

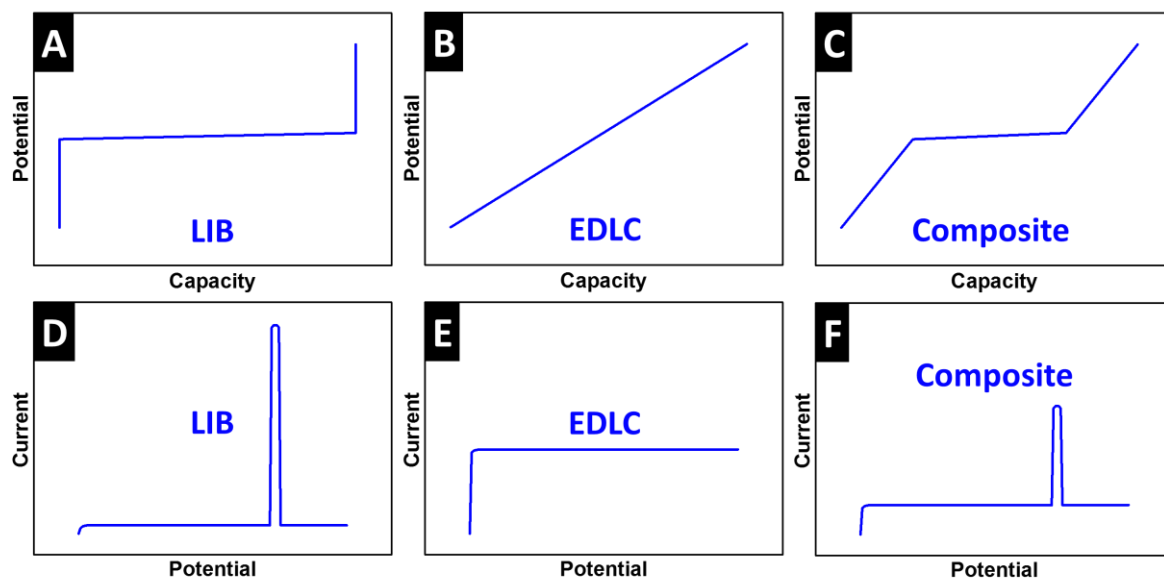


Figure 8: Schematic electrochemical response of LIB, EDLC and composite during charging under constant current (A-C) or at a constant voltage ramp (D-F). For simplicity, the potential profiles of positive electrodes were chosen.

2. Approach and Overview

As discussed in the previous section, hybridization can be carried out according to different strategies. In this thesis, the composite electrode approach was chosen due to its superior cost-effectiveness. Accordingly, constructed HSCs solely employ commercially available materials, which were further optimized via post-treatment as described in *Section 3.3*. In the following, the results of pre-investigations will be discussed to deduce cell design criterions and elucidate the research direction presented in *Section 3*.

As a starting point the electrochemical set-up proposed by Cericola et al. [19] was chosen due to its promising electrochemical performance (e.g., 53 Wh/kg, 27 kW/kg, based on active material mass). In this study, AC/LTO composite anodes and AC/LMO composite cathodes were employed as electrodes. For this purpose, two distinct composite electrode set-ups were assembled to evaluate their rate performance: i) Cells employing anodes with an AC:LTO ratio of 81:19 and cathodes with an AC:LMO ratio of 72:28 and ii) cells employing anodes with an AC:LTO ratio of 50:50 and cathodes with an AC:LMO ratio of 50:50. The power performance scaled with the AC content (i.e., i>ii) and the energy performance scaled with the LIB material content (i.e., i<ii). Asymmetric HSCs with LTO anodes combined with AC cathodes or AC anodes combined with LMO cathodes possess a much lower power capability (<2 kW/kg) as compared to the cells employing composite electrodes (>10 kW/kg). The underpinning mechanisms determining the electrochemical kinetics of the single electrodes remain blurred with this experimental approach. Uncovering such effects requires a systematic investigation of the single electrode behavior, which will be presented in the next sections.

The behavior of an individual electrode can be investigated in a three-electrode set-up, whereby the electrode of interest, the so-called working electrode (WE), is polarized versus a counter electrode (CE). The latter can be an arbitrary electrode, with the sole purpose of counterbalancing the charge of the WE. During the measurement, the voltage is measured between the WE and a reference electrode (RE), which possesses a stable and known potential. Since the RE provides the reference potential, its voltage must not change during the measurement. For organic electrolytes, the variety of RE candidates is highly limited. Only in some special cases, stable REs are available, which motivated a comprehensive study of carbon-based quasi-reference electrodes (QRE) in Li-containing organic electrolytes (*Section 3.1*). This research was mainly inspired by the unique electrochemical properties of

acetonitrile (ACN) since the high ionic conductivity of ACN is unmatched amongst all organic electrolytes.[105]

Although organic ammonium-salt containing ACN (e.g., tetraethylammonium tetrafluoroborate dissolved in ACN) is widely used and already established for commercial EDLCs, few studies considered Li-salt containing ACN as an electrolyte for LIBs or HSCs. Particularly in case of LTO-based cells, such novel electrolyte formulations are attractive and could replace conventional carbonate electrolytes, since SEI-engineering is not required in this case (*Section 1.1.2*). By using ACN-based electrolytes, ultra-high rate performance of LTO based HSCs can be enabled, which were superior to cells based on carbonate mixtures (**Figure 9A**). Additionally, ACN possesses superior electrochemical stability when used in LTO-based HSC cells (**Figure 9B**). This inferior stability of carbonates is likely connected to the well-known gas formation when cycling LTO in such electrolytes (*Section 1.1.2*).

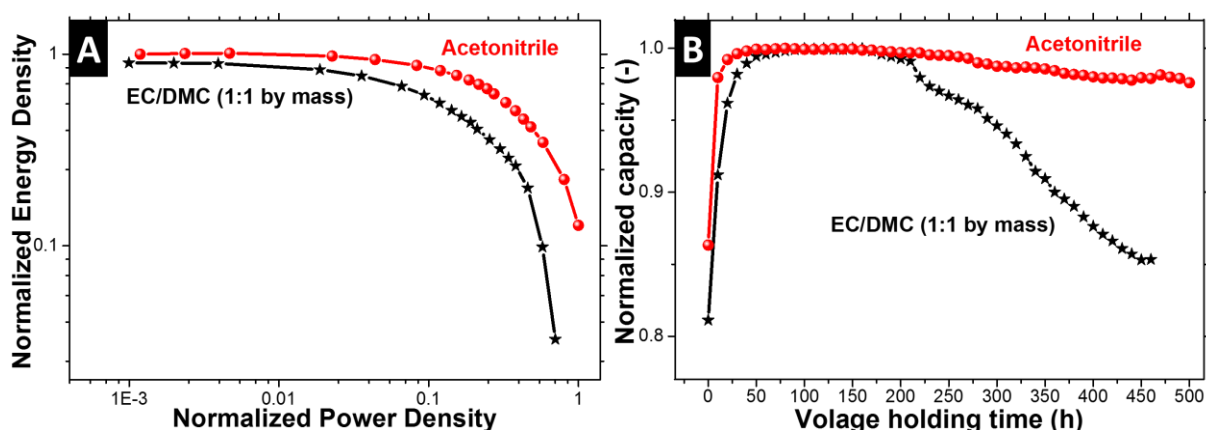


Figure 9: Ragone performance (A) and voltage hold experiments at 2.8 V and a temperature of 23 °C (B) of HSC full cells employing LTO anodes and AC/LMO composite electrodes. For all electrolytes, LiClO₄ salt was used. EC and DMC stand for ethylene carbonate and dimethyl carbonate respectively.[120]

From a cell design point of view, ACN is irreplaceable for LTO-based HSCs and was selected as the electrolyte for all follow-up measurements. However, this electrolyte severely aggravates the electrochemical characterization in a three-electrode set-up: For Li-salt containing organic electrolytes the most widespread RE is metallic lithium, but its reactivity limits its use primarily to carbonates. When Li-metal is exposed to ACN, a chemical reaction takes place which leads to formation of gas and to the entire dissolution of the Li-metal after only a few days (**Figure 10**). Thus, ACN does not allow the utilization of a Li-metal-based RE. In such a case, the lack of other non-polarizable RE alternatives requires the employment of a calibrated,

polarizable QRE. Polytetrafluoroethylene bound AC is frequently used as QRE for tetraethylammonium tetrafluoroborate containing organic electrolyte.[121–126] Although being very stable in such electrolytes, high voltage shifts of around 10 mV per day were observed when using lithium salts instead.[121] Therefore, AC-based QREs were investigated in the first part of this thesis (*Section 3.1*) to gain a better understanding of this voltage shift phenomena and to determine possible influencing factors like carbon surface area, surface functional groups and electrolytes employed.

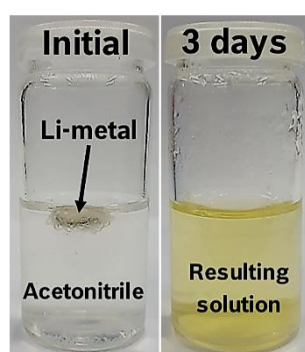


Figure 10: Reaction of lithium metal with acetonitrile (99.9 %, water content <10 ppm, Acros Organics) directly after insertion (left) and resulting solution after 3 days (right).

Like the electrolyte, also the electrode active materials highly impact the electrochemical cell performance. In case of composite electrodes based on commercial materials, there is a limited amount of choices for the active material. The challenge with this approach is to design advanced HSC via a highly optimized and synergetic combination of commercial materials. As described in *Section 1*, three inherently different electrode active materials are distinguished in this work: EDLC, anode LIB, and cathode LIB active materials. As EDLC active material, only AC is commercially utilized and is considered as irreplaceable in the following. Since SEI formation must be avoided, LTO was selected as anode LIB material due to its material properties and the high lithiation voltage (*Section 1.1.2*).

By contrast, a larger variety of commercial LIB materials is theoretically viable. Most HSCs applications impose abusive conditions on the cells (e.g., high currents) and ACN is highly flammable. Hence LCO and derivatives (e.g., NCM) thereof were not studied in this thesis due to the safety concerns connected to this material class (*Section 1.1.1*). Following the exclusion principle, the cathode LIB material choice reduces to LMO and LFP. Interestingly, composite electrodes based on LFP and LFP-derivatives showed inferior electrochemical cycling stability as compared to AC/LMO composite electrodes (**Figure 11**). These results are in contrast to the state-of-the-art literature (*Section 1.1.1*), and thus incompatibilities/side reactions of LFP with the ACN-based electrolyte are very likely. Accordingly, LMO was selected as LIB cathode material.

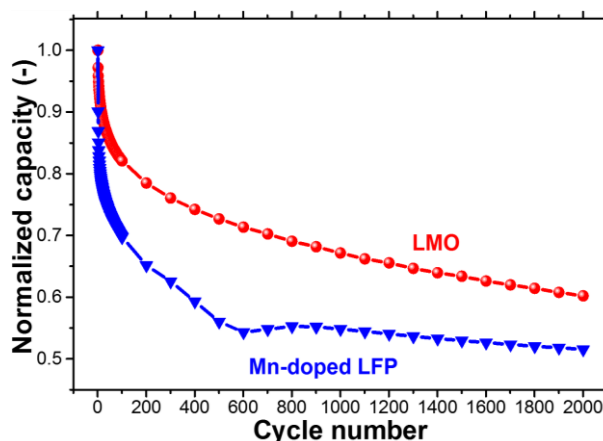


Figure 11: Galvanostatic cycling stability of AC/LMO and AC/LFP composite electrodes at 10 C in a voltage range of 3.3-4.3 V vs. Li/Li⁺. Electrodes contain 60 mass% AC, 35 mass% LMO or Mn-doped LFP and 5 mass% PVdF.[127]

Summarizing these results, the following cell design criteria were identified: .i) Highly conductive Li-salt containing ACN as an electrolyte, ii) AC as EDLC active material, iii) LTO as anode LIB material to avoid SEI formation and enable ACN electrolytes and iv.) LMO as cathode material due to its high safety and good compatibility with ACN electrolyte.

To understand the rate limitations of LTO/AC and AC/LMO composite electrodes, the LIB material content of the electrodes was incrementally raised from 10 to 40 mass% and the results are shown in **Figure 12**. The cathode follows the expected behavior, since a rising LMO content increases the electrode capacity, while coincidentally decreasing the rate capability of the electrode (**Figure 12A**). For composite anodes, a different result is observed, as an increasing LTO fraction enhances the rate capability and electrode capacity at the same time.

This can be explained with the inherently different LIB material particle size for commercially LTO and LMO: LTO is usually nano-sized with particle sizes below 100 nm, while the particle size of commercial LMO is commonly about 1-10 μm . Generally, nano-sized LIB materials are preferable for high power EES devices to decrease the Li-ion diffusion distance in the solid phase. In case of LMO, side reactions with the electrolyte prohibit such nanosizing approaches for LMO (*Section 1.1.1*). Therefore, the HSC cathode requires drastically higher AC contents as compared to HSC anodes to counterbalance the sluggish electrochemical kinetics of the micrometer-sized LMO-particles.

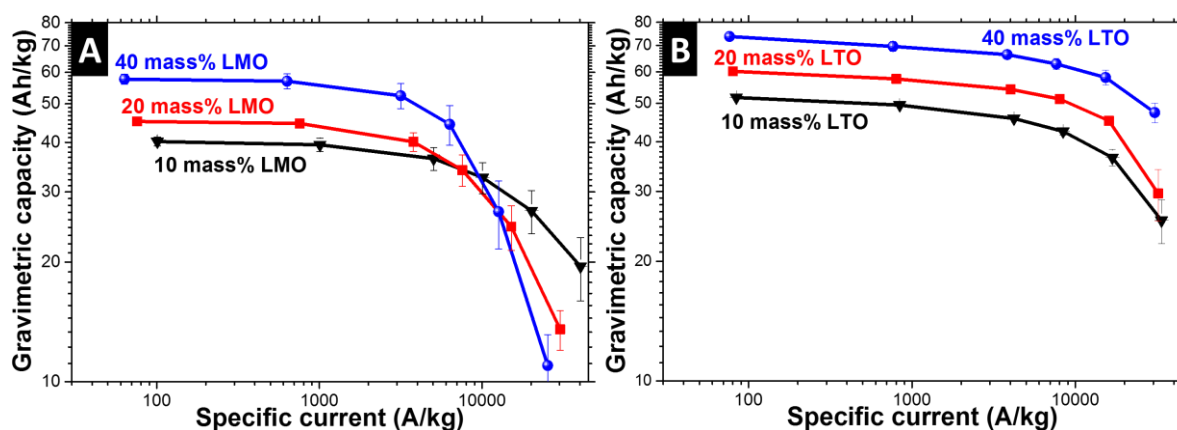


Figure 12: Rate capability measurement of AC/LMO cathodes in a voltage window of 3-4.3 V vs. Li/Li⁺(A) and AC/LTO anodes in a voltage window of 1.2-3 V vs. Li/Li⁺ with different ratios of LIB material content. All electrodes contain 10 mass% PTFE and the denoted LIB material content (the remaining electrode mass fraction is AC).[128]

Considering this background, anodes with high LTO content might be an effective approach to enhance the specific energy of HSCs without impairing the rate performance of the cells. Increasing the LTO content does drastically change the electrochemical behavior of the LTO/AC composite electrode. A detailed study of the influence of the LTO content on the composite electrode microstructure, electrolyte stability window, and electrochemical cycling stability can be found in *Section 3.2*.

At very high LTO contents the insulating nature of LTO severely deteriorates the electrochemical performance. Accordingly, high amounts of carbon are required to enable high-rate performance of LTO electrodes. This comes at the expense of a decreased overall electrode capacity. Therefore, increasing the intrinsic electronic conductivity of LTO via modification of the oxygen defect concentration is the best solution, as will be shown in *Section 3.3*.

3. Results and Discussion

This thesis includes the following papers as subchapters of the results and discussion section:

3.1 Carbon as Quasi-Reference Electrode in Unconventional Lithium-Salt Containing Electrolytes for Hybrid Battery/Supercapacitor Devices

3.2 Influence of Carbon Distribution on the Electrochemical Performance and Stability of Lithium Titanate Based Energy Storage Devices

3.3 Valence-Tuned Lithium Titanate Nanopowder for High-Rate Electrochemical Energy Storage

3.1 Carbon as Quasi-Reference Electrode in Unconventional Lithium-Salt Containing Electrolytes for Hybrid Battery/Supercapacitor Devices

M. Widmaier^{1,2}, B. Krüner^{2,3}, N. Jäckel^{2,3}, M. Aslan³, S. Fleischmann², C. Engel¹, V. Presser^{2,3}

¹ Robert Bosch GmbH, Postfach 10 60 50, 70049 Stuttgart, Germany

² Saarland University, Campus D2 2, 66123 Saarbrücken, Germany

³ INM – Leibniz Institute for New Materials, Campus D2 2, 66123 Saarbrücken, Germany

Citation:

M. Widmaier, B. Krüner, N. Jäckel, M. Aslan, S. Fleischmann, C. Engel, V. Presser, *J. Electrochem. Soc.* 163 (2016) A2956-A2964.

Own Contribution:

Planning, writing, electrochemical measurements

Abstract

Metallic lithium is the most widespread reference electrode in lithium-ion battery research, but its high reactivity limits the usage primarily to conventional carbonate-based electrolytes. Novel high power concepts, like hybrid supercapacitors, require lithium-containing electrolytes with high ionic conductivity (e.g., acetonitrile), which are not always stable versus lithium. In the current work, we face this issue by refining activated carbon as a quasi-reference electrode originally employed for conventional supercapacitors. Different commercially available carbon powders were examined as reference electrode materials and calibrated in lithium-salt containing acetonitrile versus Li⁺ intercalation/de-intercalation reaction of nanoparticulate Li₄Ti₅O₁₂. The stability of the activated carbon reference electrode is highly affected by the salt employed and decreases in the following order: LiTFSI > LiClO₄ > LiPF₆ > LiBF₄. Only a negligible impact of electrolyte solvent, pore size distribution and reference electrode binder was observed. Furthermore, activated carbon was functionalized (HNO₃ treated) and de-functionalized (thermal annealing in vacuum or hydrogen) to investigate the impact of carbon functionalization on the reference electrode stability. Nitrogen and oxygen-containing surface groups have been found to drastically improve the long-term stability of activated carbon quasi-reference electrodes. Even after 1 days exposed to the electrolyte, the potential of HNO₃ treated activated carbon is only marginally altered by 10 mV.



Carbon as Quasi-Reference Electrode in Unconventional Lithium-Salt Containing Electrolytes for Hybrid Battery/Supercapacitor Devices

M. Widmaier,^{a,b} B. Krüner,^{b,c} N. Jäckel,^{b,c} M. Aslan,^c S. Fleischmann,^b C. Engel,^a and V. Presser^{b,c,z}

^aRobert Bosch GmbH, 70049 Stuttgart, Germany

^bDepartment of Materials Science and Engineering, Saarland University, 66123 Saarbrücken, Germany

^cINM - Leibniz Institute for New Materials, 66123 Saarbrücken, Germany

Metallic lithium is the most widespread reference electrode in lithium ion battery research, but its high reactivity limits the usage primarily to conventional carbonate based electrolytes. Novel high power concepts, like hybrid supercapacitors, require lithium containing electrolytes with high ionic conductivity (e.g., acetonitrile), which are not always stable versus lithium. In the current work we face this issue by refining activated carbon as a quasi-reference electrode originally employed for conventional supercapacitors. Different commercially available carbon powders were examined as reference electrode materials and calibrated in lithium-salt containing acetonitrile versus Li^+ intercalation/de-intercalation reaction of nanoparticulate $\text{Li}_4\text{Ti}_5\text{O}_{12}$. The stability of the activated carbon reference electrode is highly affected by the salt employed and decreases in the following order: $\text{LiTFSI} > \text{LiClO}_4 > \text{LiPF}_6 > \text{LiBF}_4$. Only a negligible impact of electrolyte solvent, pore size distribution and reference electrode binder was observed. Furthermore, activated carbon was functionalized (HNO_3 treated) and de-functionalized (thermal annealing in vacuum or hydrogen) to investigate the impact of carbon functionalization on the reference electrode stability. Nitrogen and oxygen containing surface groups have been found to drastically improve long-term stability of activated carbon quasi-reference electrodes. Even after 15 days exposed to the electrolyte, the potential of HNO_3 treated activated carbon is marginally altered by 10 mV.
© 2016 The Electrochemical Society. [DOI: 10.1149/2.0421614jes] All rights reserved.

Manuscript submitted August 26, 2016; revised manuscript received October 4, 2016. Published November 4, 2016.

Lithium ion batteries remain at the focal point of research for advanced energy storage devices with high capacity.¹ State-of-the-art lithium-ion batteries (LIBs) employ cyclic carbonates (e.g., ethylene carbonate) based electrolytes to form a stable and dense solid-electrolyte interphase (SEI) on the graphite anode to prevent further electrolyte decomposition.² The SEI is formed during the first cycle of the cell and is a consequence of the lacking stability of all organic electrolytes at very low potentials. This SEI and the generally low ionic conductivity of the cyclic carbonates pose limitations to the power capability, especially at very high rates.³ New concepts based on anodes operating at higher potentials (>1 V vs. Li/Li^+), like LIB-supercapacitor hybrids⁴⁻⁷ or even $\text{Li}_4\text{Ti}_5\text{O}_{12}$ (LTO) based high power LIBs⁸ can effectively circumvent the SEI formation and enable the utilization of electrolytes with a high lithium-ion conductivity. Lithium-salt containing acetonitrile (ACN) as an example of such an unconventional electrolyte shows a unique combination of high dielectric constant and very low viscosity.² The result is an up to five-fold increased lithium-ion conductivity compared to the carbonate equivalent.⁹ The electrochemical reactions are further accelerated by the low charge transfer resistance, leading to very high rate capabilities of ACN-based charge storage devices.³ Additionally, the cyano group of ACN has been reported to beneficially inhibit aluminum current collector corrosion.¹⁰ Nevertheless, fundamental and quantitative investigations of these systems are severely aggravated by the lacking stability of lithium metal,^{2,11} which is usually employed as a reference electrode (RE) in conventional carbonate based electrolytes. A RE with a known and stable potential is indispensable for the investigation of the electrochemical behavior of the single electrodes, as potentials can only be registered with respect to a certain reference value.

A reliable RE needs its potential to be stable with time, temperature and small disturbances of the systems (e.g., passage of a small current).¹² An ideal RE is non-polarizable to assure a stable potential of the RE.^{13,14} However, the lack of ideally non-polarizable RE in non-aqueous electrolytes (other than Li/Li^+) often requires the employment of a calibrated, polarizable quasi-reference electrode (QRE) like platinum or silver wire.^{12,13} Although such wires do have a very high electrical conductivity, their potential can vary in the range of 10

to 20 mV and long-term stability of these QREs is usually not well investigated.¹² For example, Amatucci et al.⁴ employed a silver-wire QRE for characterization of organic electrolytes (1 M LiPF_6 in a mixture of ethylene carbonate and dimethyl carbonate and 1.5 M LiPF_6 in acetonitrile) and concluded an “excellent stability for one month”, although no data of the RE-potential dependent on time was shown. In that study, a potential drift of the Ag-QRE was observed, which was ascribed to reactions of the Ag with electrolyte oxidation byproducts, formed on the activated carbon electrodes. Another route was chosen by Censo et al.¹⁰ by using charged LTO as RE due to its flat voltage plateau at 1.55 V to investigate different nitrile-based electrolytes. The need to pre-charge the RE before the actual electrochemical investigation presents high additional experimental efforts. Also, this work did not investigate the stability of the RE over time.

Polytetrafluoroethylene (PTFE) bound activated carbon (AC) is frequently used as QRE for tetraethylammonium tetrafluoroborate (TEA-BF_4) containing ACN- or PC-based electrolytes¹⁴⁻¹⁹ and ionic liquids.²⁰ Such AC QREs have been reported to be less sensitive to occasional charging events and electrolyte impurities, compared to metallic wire based QREs.^{14,20} Although being very stable in organic electrolytes using TEA-BF_4 , high voltage shifts in the order of 10 mV per day were observed when using lithium salts.¹⁴ The mechanism behind this phenomenon is still under investigation and specific adsorption of Li^+ by surface functional groups has been suggested, for example by lithiation of carbonyl functionalities.¹⁴ Still, AC QREs have been employed for the characterization of LIB-supercapacitor hybrid devices operating in lithium containing organic electrolyte,^{5,21} often resulting in inconsistent reports. For example, Lane et al.²² mentioned “highly inconsistent results” for the AC-QRE when using ACN with bis(trifluoromethyl sulfonyl)imide anion (TFSI^-) and alkali or alkaline earth metal cations. They attributed this inconsistency to the anion rather than to the alkali metal cation. The voltage shift of AC in lithium-containing electrolytes was connected with the capacity fading of an AC-LTO hybrid supercapacitor operating in 1 M LiPF_6 in ethylene carbonate/dimethyl carbonate (EC/DMC, 1:1 by mass) electrolyte.²³ Similar effects were observed with symmetrical AC-AC cells employing various Li-salt containing electrolytes.²⁴ Both observation were linked to the voltage drift of AC in lithium-containing electrolyte, but the origin of this drift was not uncovered.

^zE-mail: volker.presser@leibniz-inm.de

Considering the inconsistencies in the literature and the high demand for a stable QRE, we revisited the suitability of AC based QREs for lithium-salt containing electrolytes, which are unstable versus lithium metal. We present comprehensive data to serve as a guideline for the selection (and limitation) of different carbon materials used as QRE. It is the purpose of this study to gain a better understanding of the phenomena involved and to determine possible influencing factors like surface functional groups or electrolytes employed. For that reason, we explored modifications of the carbon surface to enhance the QRE stability.

Experimental

Electrode materials and preparation.—Two commercially available steam-activated, coconut-derived activated carbon powders YP-50F and YP-80F were purchased from Kuraray Chemicals and will be referred to as AC1 and AC2, respectively. The two different carbon blacks BP2000 (Cabot) and C-ENERGY C65 (Imerys Graphite & Carbon) are referred to as CB1 and CB2, respectively. Commercial nanometer-sized (d_{50} : 1.5 μm) and carbon-coated lithium titanate oxide (LTO) T2-C1 was provided by Johnson Matthey Battery Materials.

AC1 was de-functionalized in a high temperature furnace (G-2200-91, Thermal Technology Inc.) by heating with $10^\circ\text{C}/\text{min}$ from room temperature to 1200°C . Intermediate temperature holding steps of 15 min were conducted at 120°C and 500°C in order to ensure a high vacuum at the subsequent higher temperatures. After holding the temperature at 1200°C for 5 min, the samples were cooled to room temperature with a cooling rate of $20^\circ\text{C}/\text{min}$. This treatment was performed under vacuum (~ 1 mbar) or under hydrogen flow and the samples are labelled AC1-V or AC1-H, respectively. After heat-treatment, both samples were immediately transferred into an Ar-filled glove box (MBraun, O_2 and $\text{H}_2\text{O} < 1$ ppm) to avoid re-functionalization. Functionalization of AC1, labelled AC1-N, was conducted in a nitric acid solution at 95°C for 5 h. For this purpose, 200 mL of a 62.2 mass% nitric acid solution (Sigma Aldrich) was mixed with 5 g of AC1. After the reaction, the residue was filtrated and washed several times until a pH of 6 was reached. The resulting filtrate was dried over night at 120°C in a vacuum furnace.

The counter electrode (CE) and the working electrode (WE) were prepared by using a solvent based wet process. Therefore, AC1 was mixed with isopropanol (ratio 1:2) in a DAC400 FVZ speedmixer at 2500 rpm. For the WE preparation a mixture of AC1 and LTO (ratio 5:1) was used instead of pure AC1. This treatment was followed by 7 min ultrasonic treatment and subsequent 4 min supplementary mixing at 2500 rpm. Afterwards, the slurry was transformed to a paste by adding 10 mass% (dry mass) of dissolved polytetrafluoroethylene (PTFE, 60 mass% solution in water from Sigma Aldrich) combined with speed-mixing at 800 rpm for 5 min. This paste was manually kneaded on a glass plate until the consistency of the paste was sufficiently viscous for further processing. An appropriate amount of electrode paste was placed between two untreated aluminum foils. This stack was then calendared down in a BLE682 battery lamination machine by applying a weight of 70 kg and a forward speed of 10 mm/s. The final electrode thickness was adjusted to 175 ± 20 μm for the WE and 525 ± 20 μm for CE. The CE was 2.5-times oversized (based on mass) to reduce unwanted influences of side reactions occurring at the CE.

A dry electrode preparation process inside an Ar-filled glove box (MBraun, O_2 and $\text{H}_2\text{O} < 1$ ppm) was used for all PTFE bound reference electrodes (RE). This was done to avoid re-functionalization of the de-functionalized AC1. For comparability, all PTFE-bound carbon REs were produced this way. The respective carbons and PTFE powder (PTFE 6 CN X, DuPont) were dried before they were introduced into the glove box at 120°C under vacuum (10^{-4} mbar) for 12 h. Afterwards, 0.45 g carbon powder was mixed with 0.05 g PTFE and grinded in a mortar until a “dry paste” forms. Small parts of “dry paste” were then cut out and used as RE. Additionally, polyvinylpyrrolidone (PVP) was used as a binder for RE fabrication to investigate the impact of the binder.²⁵ 0.3 g of PVP (Alfa Aesar, molecular mass 1,300,000)

was mixed with 2.7 g of AC1 and 5 g of ethanol in a DAC400 FVZ speedmixer at 2500 rpm for 6 min. The slurry was then casted on a glass plate, dried overnight in a fume hood, cut in small RE pieces and introduced into the glove box after 12 h at 120°C drying in the oven.

Cell preparation and electrochemical measurements.—For electrochemical testing, we employed a custom-built polyether ether ketone (PEEK) cell with spring loaded titanium pistons as a three-electrode system, as described elsewhere.²⁶ Electrode discs with 12 mm diameter and a typical mass of 11 ± 2 mg for the WE and 29 ± 2 mg for the CE were punched out of the free standing electrode film, separated by a glass-fiber separator (GF/D from Whatman) and placed on a carbon-coated aluminum foil current collector (Ranafoil from Toyo Aluminium K.K.). The assembled cells were dried at 120°C for 12 h at 10^{-4} mbar inside an oven and then transferred to an Ar-filled glove box (MBraun, O_2 and $\text{H}_2\text{O} < 1$ ppm). After cooling down, the RE was placed on a compressed glass-fiber separator (GF/D from Whatman) in a cavity close to the WE-CE electrode stack and contacted by a titanium wire. Afterwards the cells were vacuum-filled with either 1 M LiClO_4 , LiPF_6 or lithium bis(trifluoromethyl sulfonyl)imide (LiTFSI; battery grade from Sigma Aldrich) dissolved in acetonitrile (99.9%, extra dry over molecular sieves, water content < 10 ppm from Acros Organics) or with 1 M LiPF_6 dissolved in EC/DMC (1:1 by mass, LP30 from BASF).

Electrochemical measurements were carried out using a potentiostat/galvanostat CTS LAB from BaSyTec. Cyclic voltammetry (CV) was recorded with a sweep rate of 1 mV/s either from 0 to -1.8 V vs. RE (based on AC1, AC1-V, AC1-H, AC2, CB1, or CB2), from 0.4 to -2.2 V vs. RE (based on AC1-N) or from 3 to 1.2 V vs. RE (Li/Li⁺ RE). The first five CV cycles were measured in sequence, afterwards CVs were recorded every two hours to monitor the change of the RE potential as a function of time. Consequently, the shifted potential was calculated from the obtained LTO half wave potential (HWP). All electrochemical measurements were conducted at 23°C if not otherwise mentioned.

Porosity analysis.—Nitrogen gas sorption measurements of the carbon powders were carried out with an Autosorb iQ system (Quantachrome), at the temperature of liquid nitrogen (-196°C) after outgassing (at 300°C for 24 h) at about 10^2 Pa. The relative pressure range was varied from $5 \cdot 10^{-7}$ to 1.0 in 68 steps. The specific surface area (SSA) was calculated with the ASiQwin-software using the Brunauer-Emmett-Teller (BET) equation²⁷ in the linear pressure range from 0.01–0.2. We also calculated the SSA and pore size distribution (PSD) via quenched-solid density functional theory (QSDFT) of the absorption branch with a slit model and pore size between 0.56 and 37.5 nm.²⁸ Values for the total pore volume correspond to $p/p_0 = 0.95$.

Structural and chemical characterization.—For the modified powders care was taken to keep the time spend in ambient air at minimum (to avoid re-functionalization). Therefore, the samples were stored in an inert glove box and transferred into the respective characterization device just before the measurement.

Raman spectra were recorded with a Renishaw inVia Raman system using a Nd-YAG laser (532 nm) with 0.2 mW power at the sample's surface. The spectral resolution of ~ 1.2 cm^{-1} corresponds to a grating with 2400 lines/mm and the spot size on the sample was in the focal plane ~ 2 μm (numeric aperture = 0.9). The acquisition time was 30 s and 10 accumulations were recorded. Peak analysis and peak fitting were performed assuming one Lorentzian peak for each the D-mode and the G-mode.

Elemental chemical analysis was performed with a vario Micro Cube (Elementar) by pressing the powder samples into tin boats. An average chemical composition of three measurements was determined for each powder. The oxygen content was calculated by difference. Calibration was performed by five times measuring sulfanilamide with known elemental composition.

X-ray photoelectron spectroscopy (XPS) was carried out with a PHI Quantera SXM utilizing monochromatic $Al_{K\alpha}$ emission with an energy of 1486.6 eV for excitation (50 W, 200 μ m spot diameter) and an angle between sample and analyzer of 45°. Survey spectra were recorded with a step size of 0.8 eV and a pass energy of 224 eV. For high resolution C1s and O1s spectra a step size of 0.05 eV and a pass energy of 55 eV were used instead. The intensities were normalized with respect to the C1s maximum, which was shifted to 285 eV to calibrate the binding energies of all recorded spectra. Before the measurement, the powder samples were pressed with a steel roller onto indium foils. Immediately afterwards, the samples were introduced into an ultrahigh vacuum (UHV). Aged electrodes (stored in 1 M $LiClO_4$ ACN solution for 1 h and for 15 d) were rinsed with ACN and dried for three days at room temperature in an inert glove box. Afterwards they were pressed onto indium foil and immediately introduced into UHV for the XPS measurement.

Thermogravimetry combined with Fourier transform–infrared spectroscopy (TG–FT–IR) was performed with a NETZSCH Perseus

STA 449. Powder samples of about 250 mg were weighted in a 5 ml Al_2O_3 crucible and heated with 10°C/min from 35°C to 1200°C in an argon flow (argon 5.0) of 40 mL/min. Before the measurement the samples were flushed with argon for 15 min at 35°C within the TG–FT–IR–device. FT–IR traces of CO_2 or CO were calculated by integration of the IR spectra from 2200–2450 cm^{-1} or 2000–2250 cm^{-1} , respectively, and normalized with respect to the sample mass.²⁹

Results and Discussion

Pore structure, carbon structure, and composition of the powder materials.—Nitrogen sorption isotherms of AC1 and the modified AC1 powders show a type Ia shape with a small H4 hysteresis (Figures 1A–1B) and AC2 shows type Ib shape with very small H4 hysteresis. This is typically observed for a microporous material with narrow slit-like pores.³⁰ Contrary, the isotherm of CB1 is a mixture of type I and type II, indicating the simultaneous presence of micro

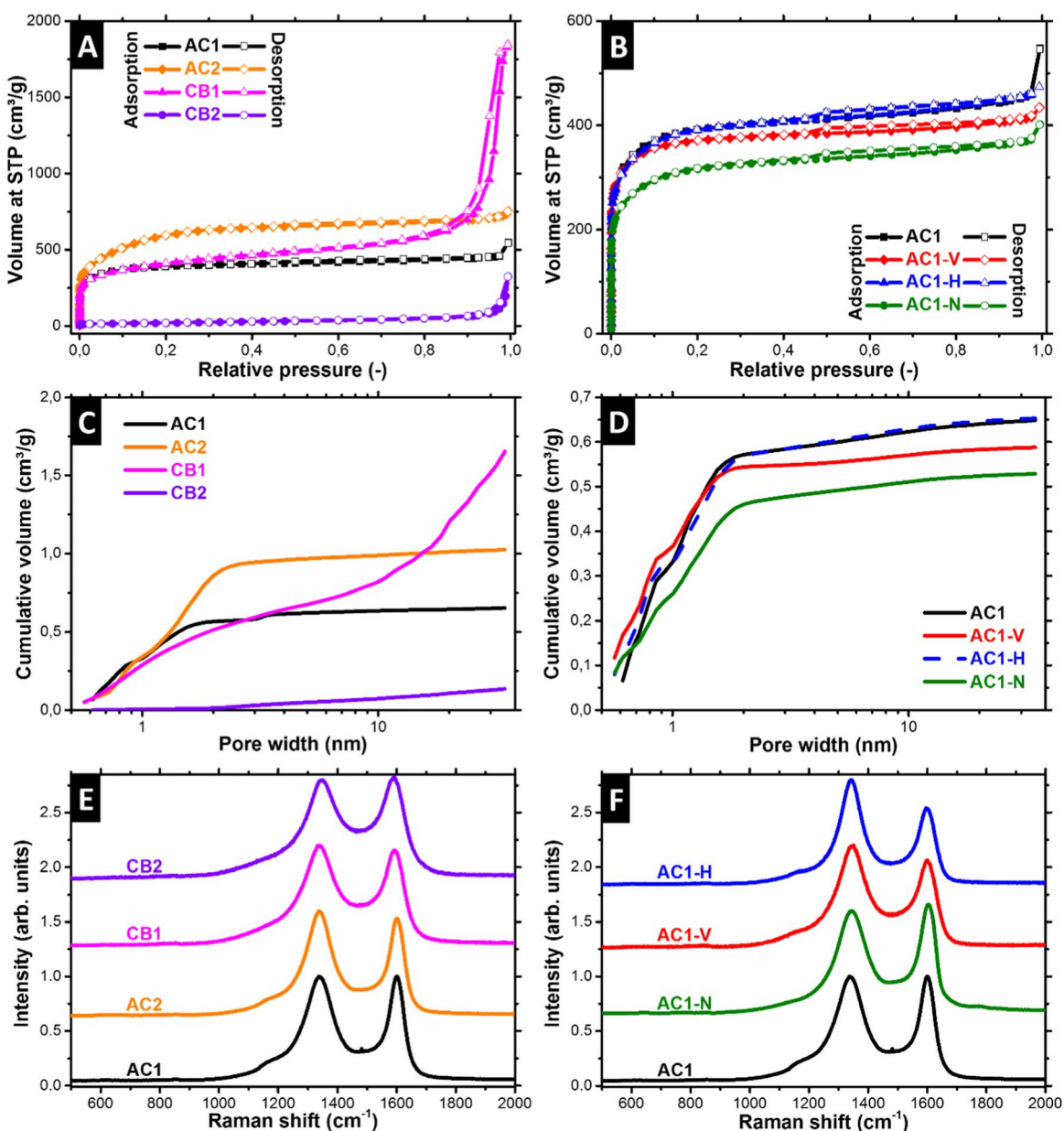


Figure 1. (A–B) Gas sorption isotherms, (C–D) pore volume distribution and (E–F) Raman spectra of the pristine carbon powders AC1, AC2, CB1, CB2 and of the modified carbon powders AC1–V, AC1–H, and AC1–N.

Table I. Specific surface area (BET and QSDFT), pore volume and average pore size of carbon materials used.

Material	BET SSA (m ² /g)	QSDFT SSA (m ² /g)	Pore volume (cm ³ /g)	Average pore size (nm)
AC1	1485	1293	0.697	0.98
AC2	2173	1687	1.094	1.33
CB1	1467	1345	1.488	10.2
CB2	75	61	0.126	8.97
AC1-N	1176	1090	0.568	1.02
AC1-V	1419	1382	0.635	0.79
AC1-H	1458	1350	0.702	0.97

and mesoporosity resulting from internal microporosity and external interparticle voids.³⁰ CB2 is a predominantly non-porous to macroporous material (type II shape).³⁰ The surface area of AC1 (QSDFT SSA: 1293 m²/g), AC2 (QSDFT SSA: 1687 m²/g) and CB1 (QSDFT SSA: 1345 m²/g) is about two orders of magnitude higher compared to CB2 (QSDFT SSA: 61 m²/g; Table I).

AC1-H possesses a similar surface area and pore volume than the pristine sample AC1 (Table I). For AC1-V, a decrease of nitrogen adsorption becomes evident, owing to a decrease of total pore volume to 0.635 cm³/g (Figure 1B, Table I). Hence the vacuum atmosphere causes a minor restructuring of the carbon surface, as both de-functionalized AC1 powders were treated under equal temperature conditions. This restructuring is accompanied by blocking/closing of micropores in the range of 1.5–2 nm as can be seen in Figure 1D. The pore volume reduction is even more pronounced for AC1-N. Nitric acid treatment leads to a pore volume decrease to 0.568 cm³/g, mainly caused by the loss of microporosity in the region of 1–2 nm. Possible reasons include the decomposition of thin pore walls^{31,32} or partial blocking of pores by functional groups created during HNO₃ treatment. Nitric acid treatment introduces nitrogen and oxygen functional groups onto the carbon surface (see chemical characterization below). Hence the pore volume reduction of AC1-N might also be affected by the resulting mass increase during HNO₃ treatment (due to the additional surface groups).

All Raman spectra of the carbon powders (Figures 1E–1F) are characterized by well separated and distinct D- and G-modes at 1338–1350 cm⁻¹ and 1586–1601 cm⁻¹, respectively, with integral I_D/I_G-ratios of 1.8–2.2 (Table II). The D-mode is caused by the breathing of sp² carbon in rings in the presence of defects³³ and the G-mode to bond stretching of sp² carbon in rings and in chains.³⁴ In agreement with Ferrari et al.,³⁵ the measured Raman spectra indicate the presence of nanocrystalline graphite. With the small variations between the different samples, we conclude that the applied treatments did only marginally influence the degree of carbon ordering/carbon structure and the primarily nanocrystalline graphite structure is effectively maintained after all investigated treatment conditions.

Elemental chemical analysis was performed to quantitatively compare the purity of the carbon powders (Table III). The amount of

Table II. Raman data of the carbon materials used. The data was fitted with one Lorentzian peak for D-mode and G-mode, respectively.

Sample	D-mode position (cm ⁻¹)	G-mode position (cm ⁻¹)	FWHM D-mode (cm ⁻¹)	FWHM G-mode (cm ⁻¹)	I _D /I _G ratio
AC1	1338	1598	133	60	2.2
AC2	1337	1599	121	59	2.1
CB1	1339	1589	166	81	2.1
CB2	1350	1586	172	90	1.8
AC1-N	1345	1601	126	62	1.9
AC1-V	1345	1596	139	75	2.1
AC1-H	1342	1596	99	65	2.0

Table III. Elemental chemical (CHNS) analysis data of the carbon powders used. Three measurements of each powder were used to calculate the average chemical composition and the standard deviation. "n.d." stands for: not detectable.

Sample	C content (mass%)	H content (mass%)	N content (mass%)	S content (mass%)	Rest (O) (mass%)
AC1	94.4 ± 1.6	0.80 ± 0.03	≤0.2	n.d.	~5–5.2
AC2	94.0 ± 0.6	0.72 ± 0.06	n.d.	n.d.	~5.3
CB1	95.4 ± 1.4	0.64 ± 0.10	n.d.	n.d.	~4.0
CB3	99.4 ± 2.0	n.d.	n.d.	n.d.	~0.6
AC1-N	78.7 ± 0.7	1.91 ± 0.09	1.03 ± 0.02	n.d.	~18.4
AC1-V	96.5 ± 0.4	0.67 ± 0.02	≤0.3	n.d.	~2.5–2.8
AC1-H	97.0 ± 0.9	0.60 ± 0.03	≤0.3	n.d.	~2.1–2.4

oxygen is indicative of the various functional groups present on the carbon surface. All pristine high surface area carbons showed relatively high oxygen contents in the range of 4–5 mass%. By contrast, the oxygen content of the low surface area carbon black CB2 was negligible (0.6 mass%). Thermal treatment of AC1 at 1200°C in H₂ atmosphere or under vacuum caused a reduction of overall oxygen content to 2–3 mass%. Nitric acid treatment led to a severe increase of oxygen content to 18 mass% due to the formation of additional surface groups as described earlier.^{31,32,36–39}

While elemental analysis is an appropriate tool to quantitatively compare carbons with relatively high elemental variations, it is not accurate enough to clearly distinguish between very similar carbons like AC1-V and AC1-H. Therefore, a more rigorous characterization of surface functionalities was performed for the modified carbons via XPS and TG-IR measurements. The XPS elemental analysis (Table IV) reveals the presence of carbon and oxygen for all investigated samples. Additionally, 1 mass% nitrogen can be detected in case of HNO₃ treatment. Compared to the CHNS elemental analysis, the same trends are confirmed by XPS characterization (taking into account the inability of XPS to measure hydrogen).⁴⁰

All C1s spectra (Figure 2A) show a main peak at 285 eV attributed to sp²-hybridized carbon and a broad peak at 291.2 eV assigned to the characteristic π→π* shake-up satellite for carbon in aromatic compounds.⁴¹ The peak at 285 eV shows a pronounced asymmetric shape to higher binding energies due to quantum mechanical coupling of core electrons with conduction electrons (comparable to XPS spectra of pure metals).⁴¹ It is well-known that more conductive (graphite-like) materials yield a stronger transition from a Gaussian-like shape to an asymmetric peak shape.³⁸ Therefore, the observed asymmetry confirms the high degree of crystallization already observed via Raman spectroscopy. Yet, it aggravates the analysis of the C1s spectra, as the influence of surface groups superimposes with the asymmetric peak shape. Nevertheless, a distinct shoulder at 289.5 eV, assigned to carboxylic or lactone groups,^{39,42,43} clearly can be observed after HNO₃ treatment. Compared to the pristine sample, the C1s intensity at binding energies between 286 to 290 eV increases for AC1-N and decreases AC1-H and AC1-V. This can be associated with a different degree of graphitization and/or to the influences of the surface groups.

The shape of the oxygen peak does not change after modification and consists of at least two components, one at about 532.0 eV and one at about 533.5 eV (Figure 2B). Generally lower binding energies

Table IV. XPS elemental analysis of pristine and of the modified AC1 powders. The average value and the standard deviation refer to measurements at three different local positions.

Sample	C content (mass%)	N content (mass%)	O content (mass%)
AC1	92.7 ± 0.6	n.d.	7.3 ± 0.6
AC1-V	97.5 ± 0.1	n.d.	2.5 ± 0.1
AC1-H	98.3 ± 0.6	n.d.	1.7 ± 0.6
AC1-N	78.7 ± 0.1	1.3 ± 0.1	20.0 ± 0.1

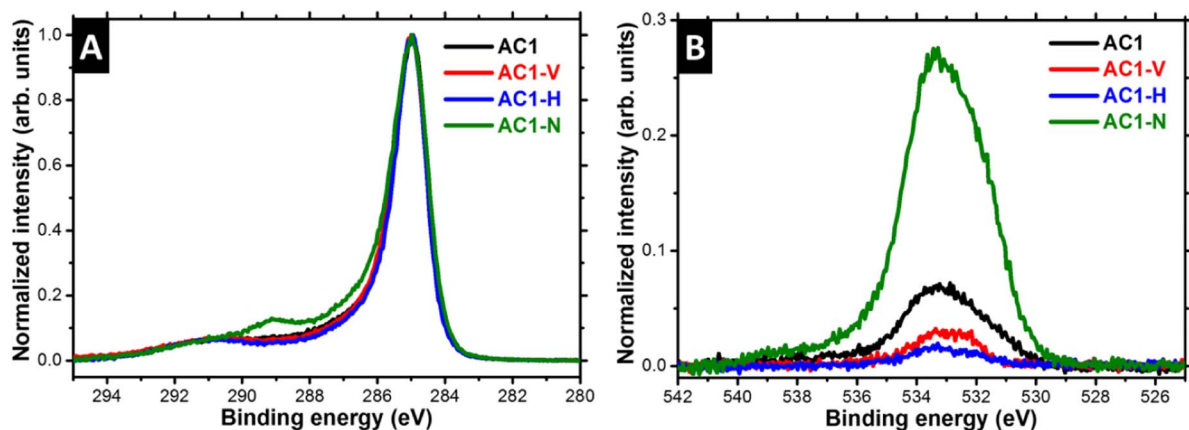


Figure 2. (A) C1s and (B) O1s high-resolution XPS-spectra of AC1, AC1-V, AC1-H, and AC1-N. The spectra were normalized with respect to the C1s peak maximum intensity.

are related to C=O double bonds, while higher binding energies are ascribed to C-O single bonds.⁴⁴ The ratio of single to double bonded oxygen atoms does not or only negligible change during the modification. The absence of the carboxylic contribution in the C1s spectra for AC1, AC1-V and AC1-H suggests that the single and double bonds found in the O1s spectra of these samples are mainly attributed to phenols, carbonyls, ethers, hydroxyls, quinones, or hydroquinones. After HNO₃ treatment, the increase of single and double bonds is attributed to the introduction of carboxylic groups. Accordingly, the degree of functionalization increases in the following order: AC1-H < AC1-V < AC1 < AC1-N. The nitrogen signal of AC1-N at 406.0 eV (Figure S1) can be assigned to nitro groups or nitrite ion residues which are characteristic for HNO₃ treated carbon.^{31,39,45}

After thermal annealing at 1200°C in argon, the mass of AC1 had decreased to 95.49% of its initial value (Figure 3A). By contrast, a higher mass for AC1-H (98.60%) and a lower value for AC1-N (73.10%) remained after annealing. Typically, the mass loss is caused by thermal decomposition of surface oxygen groups into CO and CO₂.^{38,39,42,46–48} Therefore, the residual mass reflects the carbon content of each sample and confirms the trend of elemental analysis and XPS measurements.

Desorption data of CO and CO₂ recorded by IR are shown in Figures 3B–3C. CO₂ is generally desorbed in a lower temperature regime (200–800°C, Figure 3B) than CO (400–1100°C, Figure 3C). The temperature of desorption is connected to the bonding strength of carbon atoms, affiliated in functional groups, to the graphene lattice.⁴⁶ Since chemisorbed oxygen weakens the bonds, surface functional groups containing high amounts of oxygen like carboxylic acids, lactones, and lactols are decomposed to CO₂ at relatively low temperatures.⁴⁶ No CO₂ was detected for AC1, AC1-V and AC1-H. After HNO₃ treatment, a main peak at 300°C with a shoulder at 400°C and a tail up to 800°C was seen (Figure 3B). This indicates the formation of additional surface groups and supports the conclusions drawn from the XPS analyses. The main peak can be ascribed to strongly acidic carboxyl groups.^{32,42} Higher temperature CO₂ desorption indicates additional groups like less acidic carboxyl groups, lactones, and anhydrides.^{32,42} We also have to consider that anhydrides can be formed during the measurement due to dehydration of two adjacent carboxyl groups at elevated temperatures.³²

As opposed to CO₂ formation, the release of CO at higher temperatures (>500°C, Figure 3C) originates from groups containing individual oxygen atoms like phenols, carbonyls, hydroxyls, quinones, or hydroquinones.⁴² Two main contributions to the CO profile of AC1 can be identified: one at around 700°C and one at 900°C. According to literature, the lower temperature desorption can be ascribed to phenols and hydroquinones, while higher temperature CO formation generally corresponds to carbonyl and quinone functionalities.⁴² The same peaks are also visible for AC1-N, however much more

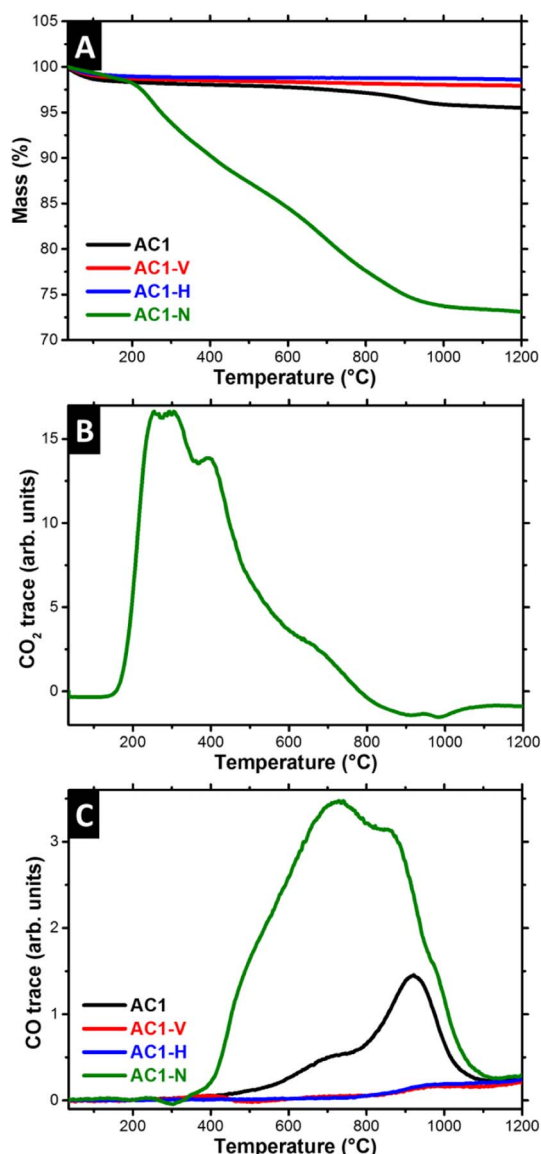


Figure 3. (A) Percentage mass change of AC1, AC1-V, AC1-H and AC1-N during thermal annealing in argon atmosphere. (B) Calculated CO₂ trace of AC1-N versus respective temperature. (C) CO trace of pristine and modified carbon powders during thermal annealing.

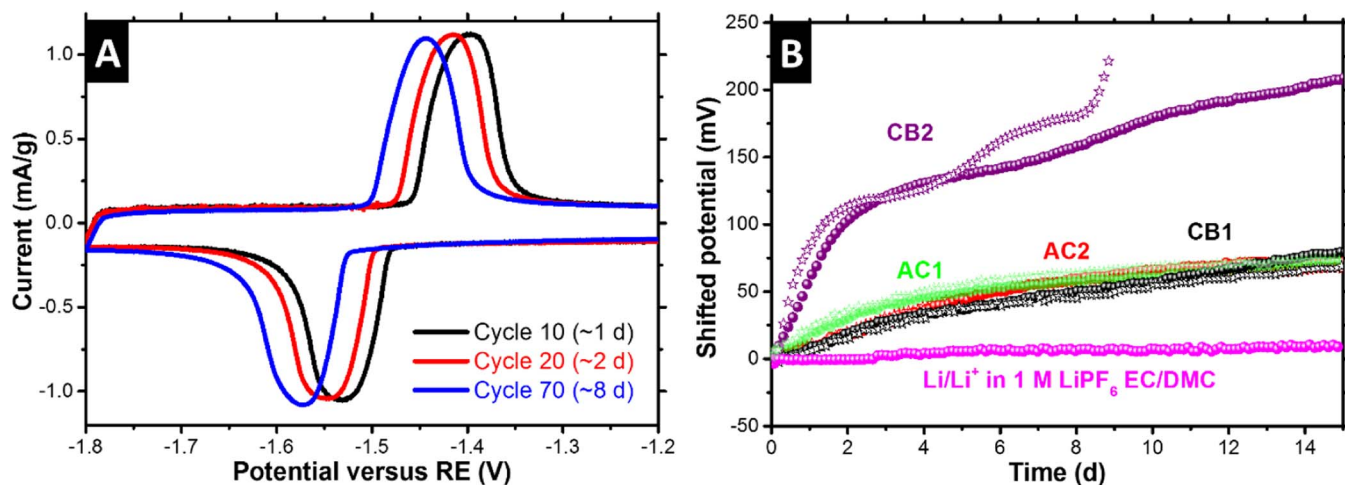


Figure 4. (A) Cyclic voltammograms measured with 1 mV/s at different points in time of a LTO doped AC WE in 1 M LiClO₄ ACN. (B) Shifted potential of different AC-QREs in dependence of time in LiClO₄ ACN. Li/Li⁺ reference electrode in 1 M LiPF₆ EC/DMC is employed to show the reliability of the chosen electrochemical set-up. Two cells were measured with each RE to account for the necessity of reproducibility.

pronounced. Furthermore, a more distinct tailing to lower temperatures (~350–500°C) is visible. This might be caused by the Boudouard reaction or by lactols respectively carboxyl anhydrides.⁴⁸ Only negligible CO evolution was detected for AC1-V and AC1-H. Possible origins could be unavoidable oxygen traces in the carrier gas, minor re-functionalization due to exposure to environment during sample transfer, or by small amounts of leftover surface groups after treatment (e.g., functional groups present in the interior of small pores).

From these data, we clearly see that bespoke surface functionalization and de-functionalization was successfully attained, while simultaneously only marginally affecting other important parameters like graphitization or porosity. Thermal annealing led to a reduction of existing surface groups (phenols, carbonyls, hydroxyls, quinones, or hydroquinones), while HNO₃ treatment increased the number of these functionalities with simultaneous introduction of additional surface groups (i.e., carboxylic and nitro groups).

Electrochemical benchmarking of different carbons utilized as QRE.

The HWP of Li⁺ insertion/extraction into nanoparticulate LTO was chosen to determine the change of the RE potential. For this purpose, the AC WE was mixed with 10 mass% of LTO. The porous activated carbon matrix of the WE enables a high contact area of LTO with electrolyte, while simultaneously providing favorable electron and ion conduction paths. This assures fast lithiation/delithiation kinetics and a precise determination of the HWP due to the resulting sharp redox peaks (see Figure 4A). Furthermore, it obviates the addition of a calibration substance, like ferrocene,^{14,20} into the electrolyte, which might influence the behavior of the RE. The stability of the LTO HWP is shown in Figure 4B for a Li/Li⁺ RE in 1 M LiPF₆ EC/DMC. Only a minor potential change of about 10 mV is observed after 15 days. Table V summarizes the initial RE potential measured versus HWP of LTO and the calculated potential of the RE versus Li/Li⁺ of the different materials in the respective electrolyte. The initial potentials center at around 3 V versus Li/Li⁺, with variations of up to 60 mV between the different carbons investigated. These results are in general agreement with previously reported data of AC QRE in 1 M LiClO₄ EC/DMC (3.07 V vs. Li/Li⁺) and 1 M LiClO₄ PC (3.03 V vs. Li/Li⁺) electrolytes.¹⁴ However, deviations are expected due to the different solvents and carbons used and illustrate the importance of a calibration of the QRE for a given electrochemical system.

The Li⁺ insertion/extraction peaks of LTO measured versus a PTFE bound AC1 in 1 M LiClO₄ ACN solution at different times are shown in Figure 4A. With increasing time of exposure to the electrolyte, a peak shift to lower potentials versus RE becomes evident. This can be associated with an increase of the overall RE potential,

as illustrated in Figure S2. We observed the same general trend for all investigated carbons. However, a massive difference in the degree of potential shift severity is visible between low surface area carbons like CB2 and high surface area carbons like AC1, AC2, and CB1 (see Figure 4B). After 5 d subjected to the electrolyte, CB2 shows typical shift values of 140 mV, whereas the potential of the AC1-, AC2-, and CB1-based QRE shifted only about 40–50 mV. Evidently, the shift behavior of all high surface area carbons is very uniform and reproducible with only minor differences between the high surface carbons (i.e., after 15 d, the potential of the high surface area carbons has shifted about 70–80 mV). No influence of the carbon pore size distribution can be verified, as mesoporous CB1 possesses the same stability as microporous AC1 and AC2 (Figure 1C, Table I, Figure 4B). The low surface area carbon, however, was plagued by sudden and arbitrary changes of the drift behavior and high deviations. This indicates the importance of the surface area on the stabilization of the potential and confirms the assumption made by Ruch et al.,¹⁴ postulating a high stability of AC-QRE due to the high inner surface area.

Two regions with different slopes can be seen for the high surface area carbons: (1) an initial region of increased slope up to 4 d and (2) a region with mitigated slope from 4–15 d. These two regions are less

Table V. Measured initial potential of the carbon QRE versus HWP of LTO for different reference electrode materials in various electrolytes. The values are determined from the first cyclic voltammogram recorded. The potential versus Li/Li⁺ was calculated by adding 1.55 V to the respective RE potential.

RE material	Electrolyte	Initial potential RE vs. HWP LTO (V)	RE vs. Li/Li ⁺ (V)
AC1	LiClO ₄ -ACN	+1.454 ± 0.003	+3.004 ± 0.003
AC2	LiClO ₄ -ACN	+1.480 ± 0.001	+3.030 ± 0.001
CB1	LiClO ₄ -ACN	+1.462 ± 0.002	+3.012 ± 0.002
CB2	LiClO ₄ -ACN	+1.422 ± 0.007	+2.972 ± 0.007
AC1-N	LiClO ₄ -ACN	+1.892 ± 0.002	+3.442 ± 0.002
AC1-V	LiClO ₄ -ACN	+1.401 ± 0.003	+2.951 ± 0.003
AC1-H	LiClO ₄ -ACN	+1.322 ± 0.003	+2.872 ± 0.003
AC1 (PVP)	LiClO ₄ -ACN	+1.463 ± 0.004	+3.013 ± 0.004
AC1	LiTFSI-ACN	+1.441 ± 0.001	+2.991 ± 0.001
AC1	LiPF ₆ -ACN	+1.461 ± 0.001	+3.011 ± 0.001
AC1	LiPF ₆ -EC/DMC	+1.492 ± 0.007	+3.042 ± 0.007
AC1	LiBF ₄ -ACN	+1.585 ± 0.004	+3.135 ± 0.004
AC1-H	LiPF ₆ -ACN	+1.332 ± 0.005	+2.882 ± 0.005
AC1-N	LiPF ₆ -ACN	+1.907 ± 0.002	+3.457 ± 0.002

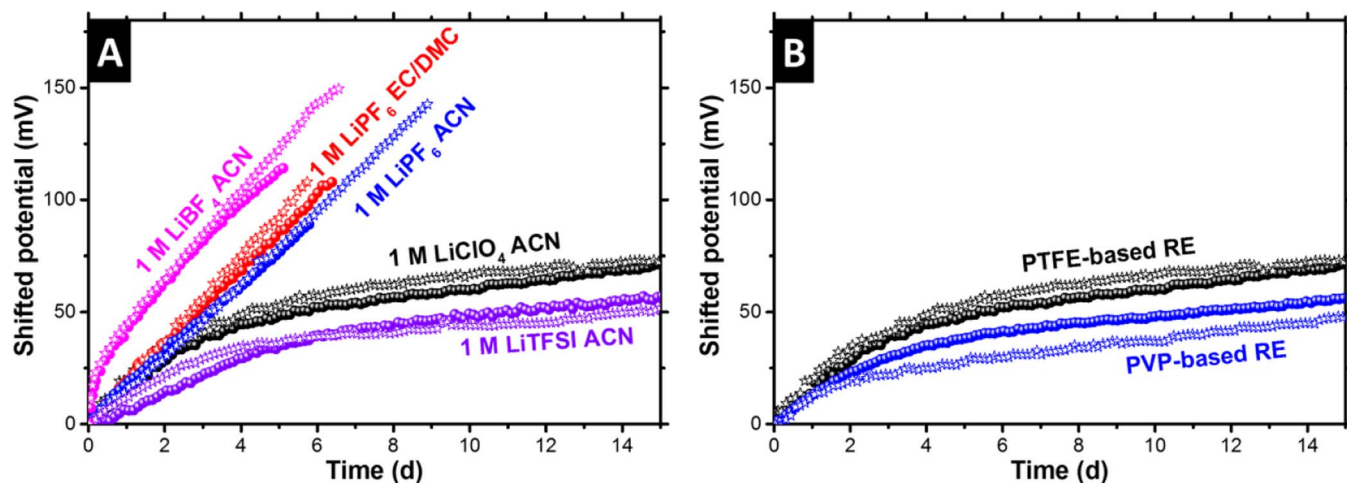


Figure 5. (A) Shifted potential of pristine AC1 based PTFE-bound QRE in various electrolytes. (B) Comparison of potential shift of a PTFE-based and a PVP-based QRE in 1 M LiClO₄ ACN. Two cells with each RE are shown to account for the necessity of reproducibility.

evident for CB2 due to the mentioned arbitrary changes of drift behavior. From the above observations it can be concluded that the cause of the shift is similar for all investigated carbons. Furthermore, when comparing the accelerated shift of the negligibly functionalized carbon CB2 (see Table III) with the lower shift of the ACs with a higher degree of functionalization, the elsewhere suggested connection¹⁴ between surface groups and specific adsorption of Li⁺ cannot be verified. The surface area difference complicates a direct comparison between these carbons. However, in the case of a specific adsorption of Li⁺, the low amount of surface groups of CB2 should be saturated rapidly, followed by equilibrium (constant potential in dependence of time). As such a behavior is not observed, a different reaction or absorption site with high concentration will be postulated later.

Carbon QRE shift characteristics in dependence of electrolyte and binder.—Further experiments were conducted with AC1, since the differences of the shift behavior between the various high surface area carbons were found to be negligible (see Figure 4B). Furthermore, the focus of the subsequent measurements was to derive qualitative understanding of the processes occurring and the respective influencing factors involved.

Only a slight influence of the anion type on the RE initial potential was seen when comparing LiClO₄, LiPF₆ and LiTFSI dissolved in ACN (Table V). The deviations of LiBF₄ in ACN and LiPF₆ in EC/DMC indicate differences of the electrical double-layer formed on the AC surface (for example due to different amount of ions adsorbed) immediately after immersion.¹⁴ A tremendous impact of the type of anion becomes evident when considering the long-term stability of the RE (Figure 5A). The stability decreases in the following order: LiTFSI > LiClO₄ > LiPF₆ > LiBF₄. Only slight differences were observed when replacing ACN with EC/DMC. It is rather surprising that LiBF₄ shows the lowest stability of all salts investigated, even though AC-QRE operating in TEA-BF₄ based electrolytes are reported to be very stable with drifts in the range of 0.2 mV per day.¹⁴ Only LiTFSI- and LiClO₄-based electrolytes show the characteristic decay of the potential shift after about 4 d, whereas LiPF₆ and LiBF₄ leads to ongoing high rates of shifting. PF₆⁻ and BF₄⁻ are both known to react with residual water in organic electrolytes to form HF and the presence of HF could explain the behavior of the RE shift.^{49,50} The same trends were also seen for different AC, as can be seen in Figure S3A and Table S1.

Because of the detrimental effect of fluorine containing anions, side reactions with fluorine of the binder or with contaminations of the binder (e.g., manufacturing process residues) of the RE (PTFE) have to be precluded. The shifted potential of the alternative binder PVP based RE in 1 M LiClO₄ ACN is shown in Figure 5B. It can be seen

that the stability is slightly increased, but still a similar shift with the same characteristic decay after four days is observed. It is difficult to quantitatively compare the results of both binders due to the necessary different production methods: PTFE-based REs were manufactured dry in an inert atmosphere and the PVP-based RE employed ethanol as a solvent. Nevertheless, fluorine originating from the binder as main cause of the reference shift can be excluded due to the marginal changes observed when exchanging the binder. Following experiments were conducted with dry fabricated PTFE REs, as this precludes changes of the carbon surface.

Coherences of carbon surface functionalization and QRE shift behavior.—It is apparent that the amount of oxygen surface groups drastically affects the initial potential of the carbon RE (Table V). Surface functionalization (AC1-N) increases the potential, while defunctionalization (AC1-V, AC1-H) reduces it. According to Tobias et al.,⁵¹ the immersion potential of high surface electrodes coincides with the potential of zero charge and can be approximated as (Eq. 1):

$$E_i = E_0 + \chi + \chi_s \quad [1]$$

where E_0 is the sum of the potential differences at the interfaces other than the high surface electrode-solution interface, χ is the surface potential due to surface dipoles like functional groups and χ_s is the surface potential due to solvent polarization. The different potentials measured can directly be correlated to variations of χ and χ_s due to different quantities of surface functionalities. High amounts of electron-withdrawing oxygen groups explain the increase of the potential of AC1-N, while removal of these groups is accompanied by a decrease of the potential (AC1-V and AC1-H). Although both defunctionalized carbons were treated at equal temperature conditions and show only negligible differences in chemical composition (see Pore structure, carbon structure, and composition of the powder materials section), a large 80 mV variation of the potential was measured. A similar effect had been reported by Tobias et al.⁵¹ for modified carbon black electrodes in 0.1 M NaCl aqueous solutions. It was proposed that this could be explained by the electron donating effect of chemisorbed hydrogen. It is also well-known that the defect structure of thermally treated activated carbon is drastically affected by the treatment atmosphere.^{46,52,53} The thermal removal of oxygen groups in inert atmosphere results in high energy (isolated unpaired electron sites) and low energy dangling bonds (divalent in-plane sigma pairs at the edges of graphene layers).^{46,52} Contrary, methanation typically removes high-energy sites in hydrogen atmosphere.^{46,52} Different types and amounts of dangling bonds present in AC1-V and AC1-H might also explain the different potentials measured (due to the electron-withdrawing ability of these sites).

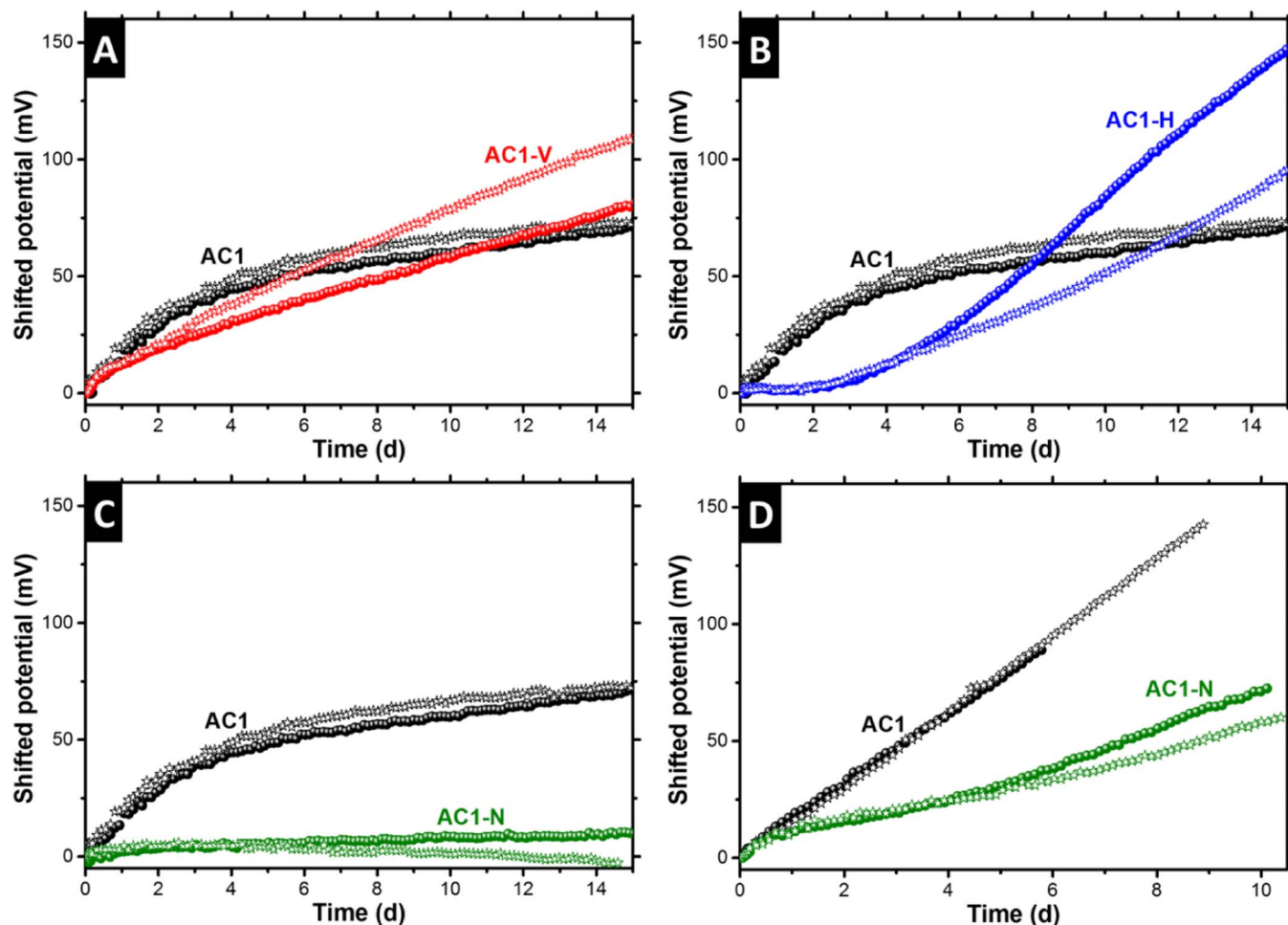


Figure 6. (A-C) Shifted potential of AC1, AC1-V, AC1-H and AC1-N based RE in 1 M LiClO₄ ACN. (D) Comparison of potential shift of AC1 and AC1-N in 1 M LiPF₆ ACN. Two cells with each RE are shown to account for the necessity of reproducibility.

The stability of AC1-V based RE in 1 M LiClO₄ did only slightly improve during the first five days compared to the RE produced with pristine AC1 (Figure 6A). Additionally, no decline of the shifted potential for AC1-V was observed after four days. Although chemically very similar, a completely different behavior occurred for AC1-H (Figures 6A–6B). During the first two days, the potential shift was completely suppressed. The different defect structure developed during annealing in hydrogen atmosphere^{46,52} might also explain this different behavior of AC1-V and AC1-H. Defects like dangling bonds are highly reactive sites and it is very likely that the presence of such defects is also correlated to the stability of the RE. Clearly, the stabilizing effect of AC1-H started to vanish after two days. Afterwards, high shifts were observed, comparable to AC1-V. Counter-intuitively, heavily functionalized AC1-N based RE are remarkably resistant with the lowest potential shift amongst all investigated REs (Figure 6C). The presence of nitrogen- and oxygen-containing surface groups inhibited the RE shift in such a way that the potential was solely increased by 10 mV, even after 15 d exposed to the electrolyte. Even in case of demanding 1 M LiPF₆ ACN electrolytes, a significant improvement of stability was visible for AC1-N (Figure 6D), while no suppression of potential shift was retained for AC1-H (Figure S3B). Moreover, first measurements indicate that the remarkable stability of AC1-N is even maintained at elevated temperatures of 40°C (see Figure S4). At such temperatures untreated AC1-N shows only a slightly increased rate of shifting compared to the measurement at 23°C, while AC1 appears to be less reproducible with high deviations from cell to cell.

These observations suggest that the origin of the shift is an interaction between electrolyte species and the carbon surface. A fresh,

hydrogen treated carbon surface is kinetically stabilized during the first days in 1 M LiClO₄ ACN, but a shift of potential is inevitable. While the mechanism behind this is still unclear, it could be argued that highly reactive carbon sites are decreased or passivated during annealing in hydrogen atmosphere. Surface groups probably act as a barrier between the electrolyte-carbon interface, as can be deduced from the behavior of AC1-N based RE. Therefore, the interaction between the electrolyte and the carbon surface will attenuate in the presence of surface groups. It is impossible that the entire carbon surface area is fully saturated by functional groups, even in case of highly functionalized AC1-N. Hence, the inhibitory effect of surface functionalities might arise due to blocking/eliminating of specific (highly reactive) surface sites. For example, it is known that surface functional groups of activated carbon are predominantly located at the edges of the graphene layers.^{46–48} Moreover, basic behavior of oxygen deficient activated carbon was connected to specific absorption of protons at Lewis basic sites, mainly at localized π electron pairs at the edges of graphene sheets.⁴⁶ Such sites might also attract Li⁺ ions of the electrolyte and it could be argued that a similar mechanism involving Li⁺ ions (with supplementary protons in case of LiPF₆ and LiBF₄ based electrolytes) leads to the observed potential shift of the RE in our case. Physisorbed cations would act as electron-withdrawing entities, which would increase the potential with increasing amounts of cations absorbed (similar to the influence of surface groups on the potential explained above). Hence, an accumulation of absorbed cations at the carbon surface can explain the increase of RE potential in dependence of time. Typically, the surface basicity of the carbon is lost after re-functionalization with oxygen surface groups.⁴⁶

Consequently, the affinity of Li^+ to the carbon surface should also decrease with increasing amount of surface groups (and therefore improve the QRE stability).

The chemical composition of PTFE-bound electrodes stored for 1 h and 15 d in 1 M LiClO_4 ACN electrolyte changed only insignificantly (Table S2). Minor differences of the fluorine content were observed, which are most likely caused by an inhomogeneous PTFE distribution becoming apparent by the high standard deviation of the measurement (Table S2). The electrolyte does not contain fluorine and a reaction of fluorine from the binder as the main reason of the potential shift was already precluded (see Electrochemical benchmarking of different carbons utilized as QRE section). The ratio of C/O and C/Cl of the electrodes stored in the electrolyte stays almost constant (within the error range) and no nitrogen was measurable. Hence a chemical reaction of the carbon electrodes with lithium containing electrolyte is highly improbable. This supports the hypothesis of Li^+ adsorption at specific carbon sites.

Conclusions

In the present study we investigate carbon based QRE for lithium-salt containing electrolytes, which are reactive toward lithium metal. PTFE-bound, carbon based QREs were employed and calibrated in various electrolytes utilizing high and low surface area carbons. An increase of reference electrode potential is characteristic for all studied carbons. However, a drastic difference between low and high surface area carbons was observed. Low surface area carbon based QREs are impaired by high rates of potential shift (140 mV after 5 d) with additional sudden and arbitrary fluctuations. On the other hand, all high surface area carbon based QREs show very low, uniform and reproducible rates of potential shift (40–50 mV after 5 d). Compared to LiTFSI and LiClO_4 based electrolytes, a drastically increased RE potential shift was observed in LiPF_6 and LiBF_4 electrolytes. Contrary, only a negligible impact of carbon pore size distribution, electrolyte solvent and binder on the potential shift of the QRE was found.

Activated carbon was functionalized via HNO_3 treatment and de-functionalized via thermal annealing in vacuum and hydrogen atmosphere to investigate the role of surface functionalities on the RE shift. The degree of surface functionalization was validated via elemental chemical analysis, XPS and TG-FT-IR characterization. Other important material parameters like graphitization, surface area, and porosity were only marginally affected as confirmed by Raman and gas sorption measurements. Heavily functionalized (HNO_3 treated) AC based RE showed drastically improved long-term RE stability. Even after 15 days of continuous measurement, the potential of the functionalized AC based QRE was only marginally altered by 10 mV. Therefore, we consider functionalized AC as a very promising QRE for the characterization of novel energy storage devices employing lithium-salt containing electrolytes, unstable versus lithium metal.

Acknowledgments

The authors thank A. Fuchs, A. Gonser, M. Tuchen, and A. Jung for the support and helpful discussions of XPS, TG-FT-IR, and CHNS measurements. We acknowledge the support and discussions with J. Lee and S. Choudhury (INM). We thank Johnson Matthey Battery Materials for kindly providing $\text{Li}_4\text{Ti}_5\text{O}_{12}$ and Prof. Eduard Arzt (INM) for his continuing support.

References

1. B. Serosati and J. Garche, *Journal of Power Sources*, **195**(9), 2419 (2010).
2. K. Xu, *Chemical reviews*, **114**(23), 11503 (2014).
3. Q. Wang, S. M. Zakeeruddin, I. Exnar, and M. Grätzel, *J. Electrochem. Soc.*, **151**(10), A1598 (2004).
4. G. G. Amatucci, F. Badway, A. Du Pasquier, and T. Zheng, *J. Electrochem. Soc.*, **148**(8), A930 (2001).
5. D. Cericola, P. Novák, A. Wokaun, and R. Kötz, *Journal of Power Sources*, **196**(23), 10305 (2011).

6. E. Zhao, C. Qin, H.-R. Jung, G. Berdichevsky, A. Nese, S. Marder, and G. Yushin, *ACS nano*, **10**(4), 3977 (2016).
7. K. Naoi, K. Kisu, E. Iwama, S. Nakashima, Y. Sakai, Y. Orikasa, P. Leone, N. Dupré, T. Brousse, P. Rozier, W. Naoi, and P. Simon, *Energy Environ. Sci.*, **9**(6), 2143 (2016).
8. T. Ohzuku, *J. Electrochem. Soc.*, **142**(5), 1431 (1995).
9. F. Béguin and E. Frackowiak, *Supercapacitors: Materials, systems, and applications*/ edited by François Béguin and Elżbieta Frackowiak, Weinheim, Wiley-VCH (2013).
10. D. Di Censo, I. Exnar, and M. Graetzel, *Electrochemistry Communications*, **7**(10), 1000 (2005).
11. D. Orbakh, *Nonaqueous electrochemistry*, New York, Dekker (1999).
12. C. M. A. Brett and A. M. O. Brett, *Electrochemistry: Principles, methods, and applications* / Christopher M. A. Brett and Ana Maria Oliveira Brett, Oxford, Oxford University Press (1993).
13. A. J. Bard and L. R. Faulkner, *Electrochemical methods: Fundamentals and applications* / Allen J. Bard and Larry R. Faulkner, New York, Chichester, John Wiley (2001).
14. P. W. Ruch, D. Cericola, M. Hahn, R. Kötz, and A. Wokaun, *Journal of Electroanalytical Chemistry*, **636**(1–2), 128 (2009).
15. N. Jäckel, D. Weingarh, A. Schreiber, B. Krüner, M. Zeiger, A. Tolosa, M. Aslan, and V. Presser, *Electrochimica Acta*, **191**, 284 (2016).
16. M. Hahn, O. Barbieri, F. P. Campana, R. Kötz, and R. Gallay, *Appl. Phys. A*, **82**(4), 633 (2006).
17. P. W. Ruch, D. Cericola, A. Foelske-Schmitz, R. Kötz, and A. Wokaun, *Electrochimica Acta*, **55**(15), 4412 (2010).
18. P. W. Ruch, D. Cericola, A. Foelske, R. Kötz, and A. Wokaun, *Electrochimica Acta*, **55**(7), 2352 (2010).
19. D. Weingarh, H. Noh, A. Foelske-Schmitz, A. Wokaun, and R. Kötz, *Electrochimica Acta*, **103**, 119 (2013).
20. D. Weingarh, A. Foelske-Schmitz, A. Wokaun, and R. Kötz, *Electrochemistry Communications*, **18**, 116 (2012).
21. D. Cericola, P. Novák, A. Wokaun, and R. Kötz, *Electrochimica Acta*, **56**(24), 8403 (2011).
22. G. H. Lane and E. Jezek, *Electrochimica Acta*, **150**, 173 (2014).
23. S. Dsoke, B. Fuchs, E. Gucciardi, and M. Wohlfahrt-Mehrens, *Journal of Power Sources*, **282**, 385 (2015).
24. T. Zhang, B. Fuchs, M. Secchiarioli, M. Wohlfahrt-Mehrens, and S. Dsoke, *Electrochimica Acta*, **218**, 163 (2016).
25. M. Aslan, D. Weingarh, N. Jäckel, J. S. Atchison, I. Grobelsek, and V. Presser, *Journal of Power Sources*, **266**, 374 (2014).
26. D. Weingarh, M. Zeiger, N. Jäckel, M. Aslan, G. Feng, and V. Presser, *Adv. Energy Mater.*, **4**(13), 1400316 (2014).
27. S. Brunauer, P. H. Emmett, and E. Teller, *J. Am. Chem. Soc.*, **60**(2), 309 (1938).
28. G. Y. Gor, M. Thommes, K. A. Cychosz, and A. V. Neimark, *Carbon*, **50**(4), 1583 (2012).
29. A. Schindler, G. Neumann, A. Rager, E. Füglein, J. Blumm, and T. Denner, *J Therm Anal Calorim*, **113**(3), 1091 (2013).
30. M. Thommes, K. Kaneko, A. V. Neimark, J. P. Olivier, F. Rodriguez-Reinoso, J. Rouquerol, and K. S. Sing, *Pure and Applied Chemistry*, **87**(9) (2015).
31. C. Moreno-Castilla, M. A. Ferro-García, J. P. Joly, I. Bautista-Toledo, F. Carrasco-Marín, and J. Rivera-Utrilla, *Langmuir*, **11**(11), 4386 (1995).
32. C. Moreno-Castilla, F. Carrasco-marín, F. J. Maldonado-hódar, and J. Rivera-Utrilla, *Carbon*, **36**(1–2), 145 (1998).
33. Thomsen and Reich, *Physical review letters*, **85**(24), 5214 (2000).
34. A. C. Ferrari and J. Robertson, *Philosophical transactions. Series A, Mathematical, physical, and engineering sciences*, **362**(1824), 2477 (2004).
35. A. C. Ferrari and J. Robertson, *Phys. Rev. B*, **61**(20), 14095 (2000).
36. Y. Otake and R. G. Jenkins, *Carbon*, **31**(1), 109 (1993).
37. G. S. Szymański, Z. Karpiński, S. Biniak, and A. Świątkowski, *Carbon*, **40**(14), 2627 (2002).
38. J. Figueiredo, M. Pereira, M. Freitas, and J. Órfão, *Carbon*, **37**(9), 1379 (1999).
39. C. Moreno-Castilla, M. López-Ramón, and F. Carrasco-Marín, *Carbon*, **38**(14), 1995 (2000).
40. N. Stojilovic, *J. Chem. Educ.*, **89**(10), 1331 (2012).
41. J. F. Moulder, J. Chastain, and R. C. King, *Handbook of X-ray photoelectron spectroscopy: A reference book of standard spectra for identification and interpretation of XPS data*, Eden Prairie, Minn., Physical Electronics (1995).
42. U. Zielke, K. J. Hüttinger, and W. P. Hoffman, *Carbon*, **34**(8), 983 (1996).
43. Z. R. Yue, W. Jiang, L. Wang, S. D. Gardner, and C. U. Pittman, *Carbon*, **37**(11), 1785 (1999).
44. S. Dalavi, P. Guduru, and B. L. Lucht, *J. Electrochem. Soc.*, **159**(5), A642 (2012).
45. P. Chingombe, B. Saha, and R. J. Wakeman, *Carbon*, **43**(15), 3132 (2005).
46. J. A. Menéndez, B. Xia, J. Phillips, and L. R. Radovic, *Langmuir*, **13**(13), 3414 (1997).
47. C. Leon y Leon, J. Solar, V. Calemma, and L. Radovic, *Carbon*, **30**(5), 797 (1992).
48. H. Boehm, *Carbon*, **40**(2), 145 (2002).
49. T. R. Jow, K. Xu, O. Borodin, and M. Ue, *Electrolytes for Lithium and Lithium-Ion Batteries*, New York, NY, Springer New York (2014).
50. P. Kurzweil and M. Chwistek, *Journal of Power Sources*, **176**(2), 555 (2008).
51. H. Tobias and A. Soffer, *Journal of Electroanalytical Chemistry and Interfacial Electrochemistry*, **148**(2), 221 (1983).
52. J. A. Menéndez, J. Phillips, B. Xia, and L. R. Radovic, *Langmuir*, **12**(18), 4404 (1996).
53. B. Dyatkin and Y. Gogotsi, *Faraday discussions*, **172**, 139 (2014).

**CARBON AS QUASI-REFERENCE ELECTRODE
IN UNCONVENTIONAL LITHIUM-SALT CONTAINING ELECTROLYTES
FOR HYBRID BATTERY/SUPERCAPACITOR DEVICES**

M. Widmaier^{1,2}, B. Krüner^{2,3}, N. Jäckel^{2,3}, M. Aslan³, S. Fleischmann², C. Engel¹, V. Presser^{2,3,*}

¹ Robert Bosch GmbH, Postfach 10 60 50, 70049 Stuttgart, Germany

² Department of Materials Science and Engineering, Saarland University, Campus D2 2, 66123 Saarbrücken, Germany

³ INM – Leibniz Institute for New Materials, Campus D2 2, 66123 Saarbrücken, Germany

* corresponding author's email: volker.presser@leibniz-inm.de

Supporting Information

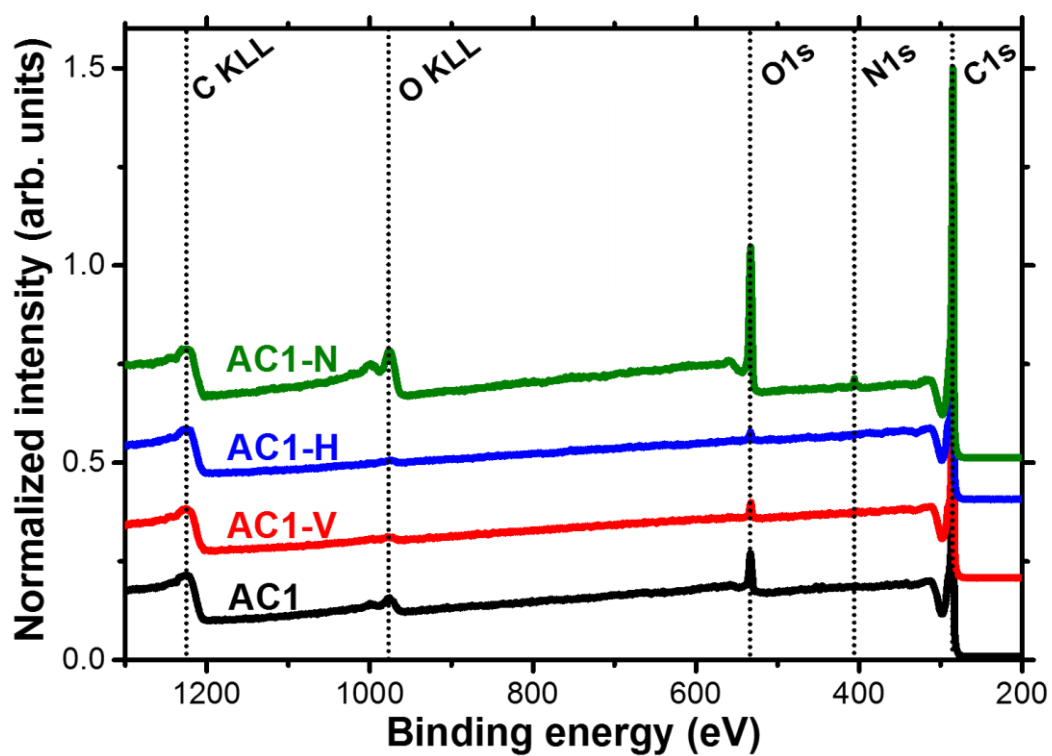


Fig. S1: XPS survey scan of pristine and modified AC1. The spectra were normalized with respect to the C1s peak.

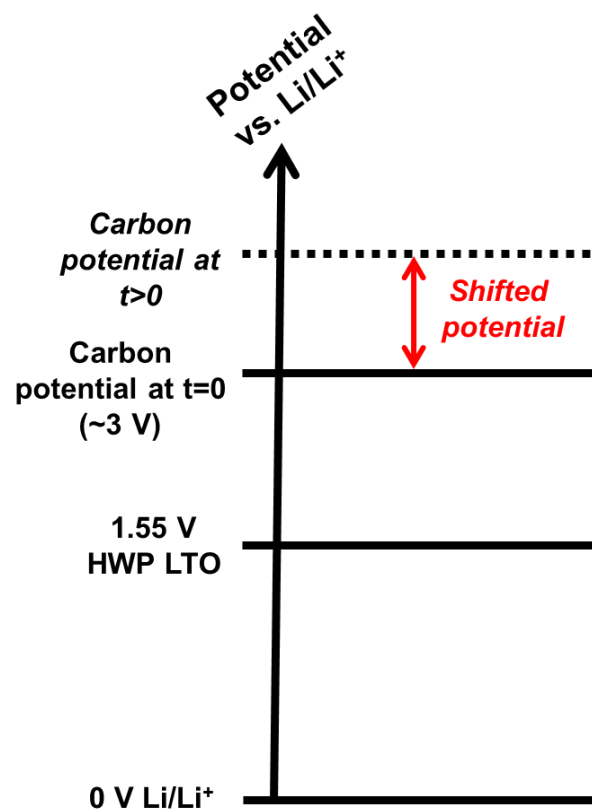


Fig. S2: Illustration of the voltage shift observed in carbon QRE.

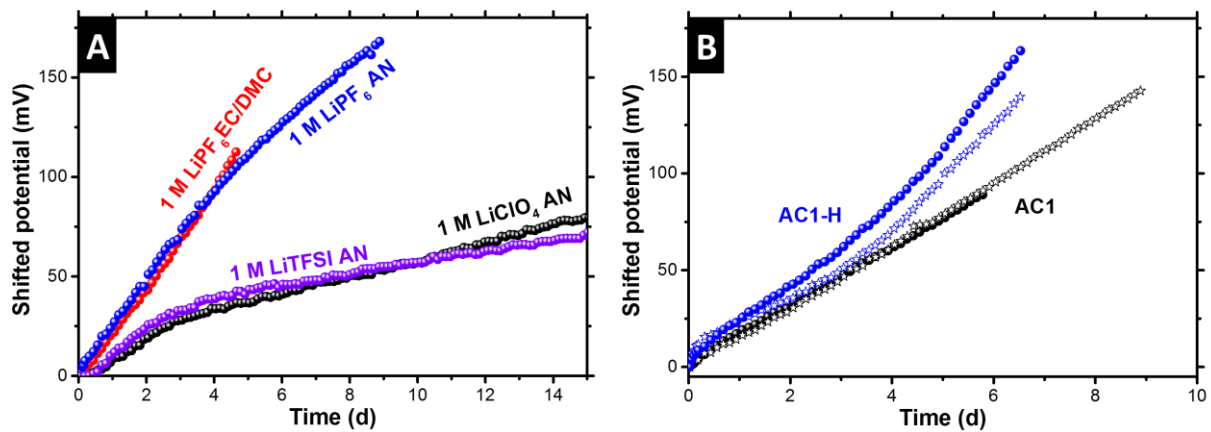


Fig. S3: (A) Shifted potential of CB1 based PTFE-bound QRE in various electrolytes. (B) Comparison of potential shift of AC1 and AC1-H in 1 M LiPF₆ ACN. Two cells were measured with each RE to account for the necessity of reproducibility.

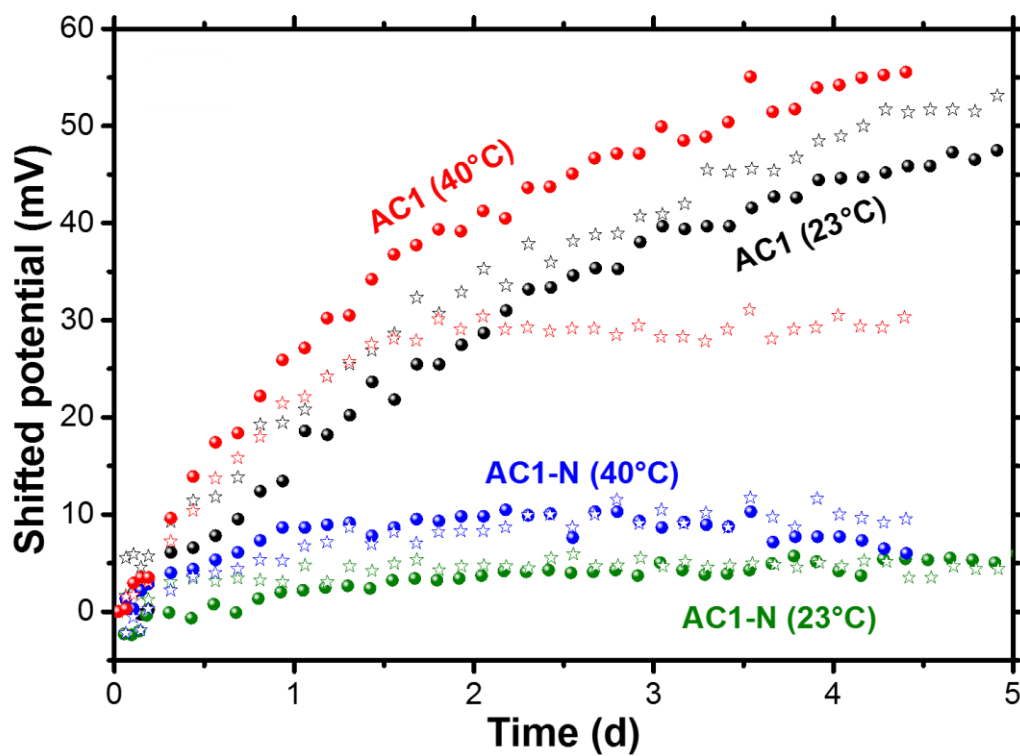


Fig. S4: (A) Shifted potential of AC1 and AC1-N based PTFE-bound QRE in 1 M LiClO₄ ACN at 23 °C and at 40 °C. For the 40 °C measurement the cells were placed for 2 h in a climate chamber prior to the measurement (in order to reach temperature equilibrium inside the cell). Two cells were measured with each RE to account for the necessity of reproducibility.

Tables

Table S1: Measured initial potential of REs versus HWP of LTO for different reference electrode materials in various electrolytes. For the 40 °C measurement the cells were placed for 2 h in a climate chamber prior to the measurement (in order to reach temperature equilibrium inside the cell). The values are determined from the first cyclic voltammogram recorded. The potential versus Li/Li⁺ was calculated by adding 1.55 V to the respective RE potential.

RE material	Electrolyte	Average RE vs. LTO first half-wave potential (V)	RE vs. Li/Li ⁺ (V)
CB1	LiClO ₄ -ACN	+1.462±0.002	+3.012±0.002
CB1	LiTFSI-ACN	+1.448±0.003	+2.998±0.003
CB1	LiPF ₆ -ACN	+1.482±0.006	+3.032±0.006
CB1	LiPF ₆ -EC/DMC	+1.498±0.005	+3.048±0.005
Li/Li ⁺	LiPF ₆ -EC/DMC	-1.549±0.006	+0.001±0.006
AC1 (40 °C)	LiClO ₄ -ACN	+1.444±0.002	+2.994±0.002
AC1-N (40 °C)	LiClO ₄ -ACN	+1.887±0.001	+3.437±0.002

Table S2: XPS elemental analysis of pristine PTFE-bound electrodes and of electrodes stored for 1 h respectively 15 d in 1 M LiClO₄ ACN solution. The average value and the standard deviation refer to measurements at three different local positions.

Sample	Average C (atom%)	Average F (atom%)	Average O (atom%)	Average Cl (atom%)	Ratio C/O (-)	Ratio C/F (-)	Ratio C/Cl (-)
pristine	73.3±1.6	22.0±1.9	4.4±0.3	Not traceable	16.6	3.3	-
1 h	63.4±4.5	28.9±5.8	6.6±1.1	0.5±0.2	9.6	2.2	125.2
15 d	73.9±5.9	16.7±6.9	8.2±0.9	0.6±0.0	9.1	4.4	127.4

3.2 Influence of Carbon Distribution on the Electrochemical Performance and Stability of Lithium Titanate Based Energy Storage Devices

M. Widmaier^{1,2}, N. Jäckel^{2,3}, M. Zeiger^{2,3}, M. Abuzarli⁴, C. Engel¹, L. Bommer¹, V. Presser^{2,3}

¹ Robert Bosch GmbH, Postfach 10 60 50, 70049 Stuttgart, Germany

² Saarland University, Campus D2 2, 66123 Saarbrücken, Germany

³ INM – Leibniz Institute for New Materials, Campus D2 2, 66123 Saarbrücken, Germany

⁴ ESPCI Paris, PSL Research University, 10 rue Vauquelin, 75231 Paris Cedex 05, France

Citation:

M. Widmaier, N. Jäckel, M. Zeiger, M. Abuzarli, C. Engel, L. Bommer, V. Presser, *Electrochimica Acta* 247 (2017) 1006-1018

Own Contribution:

Planning, writing, electrochemical measurements

Abstract

We explore different electrode microstructures and the associated implications on the electrochemical stability of activated carbon/ lithium titanate ($\text{Li}_4\text{Ti}_5\text{O}_{12}$, LTO) composite electrodes by incrementally increasing the LTO content. At low LTO concentrations, the electrochemical stability is progressively improved with respect to neat activated carbon-based electrodes. This trend is abruptly changed for high LTO concentrations (72 mass%) as the electrolyte starts to decompose unexpectedly far below the electrochemical stability boundaries of the single materials. We attribute this to a loss of electrical percolation and local degradation spots caused by peculiarities of the carbon distribution: Initially the sub-micrometer-sized LTO solely occupies spaces between the large, micrometer-sized activated carbon. With increasing LTO content, the activated carbon particles get separated in an insulating LTO matrix. Electrochemical stability can be reestablished with electronic conduction paths of well distributed sub-micrometer-sized carbon black particles. By this way, cell degradation can be reduced, and the cycle life of cells with high LTO concentration is prolonged from 10 to >36,000 cycles. Finally, we propose a simple method to distinguish cell fading caused by electrolyte decomposition from cell fading caused by poor electrical percolation.



Influence of carbon distribution on the electrochemical performance and stability of lithium titanate based energy storage devices



Mathias Widmaier^{a,b}, Nicolas Jäckel^{b,c,1}, Marco Zeiger^{b,c}, Murad Abuzarli^d,
Christine Engel^a, Lars Bommer^a, Volker Presser^{b,c,*}

^a Robert Bosch GmbH, Postfach 10 60 50, 70049 Stuttgart, Germany

^b Department of Materials Science and Engineering, Saarland University, Campus D2 2, 66123 Saarbrücken, Germany

^c INM – Leibniz Institute for New Materials, Campus D2 2, 66123 Saarbrücken, Germany

^d ESPCI Paris, PSL Research University, 10 rue Vauquelin, 75231 Paris Cedex 05, France

ARTICLE INFO

Article history:

Received 27 June 2017

Accepted 11 July 2017

Available online 12 July 2017

Keywords:

electrochemical energy storage

hybrid electrodes

lithium titanate

nanoporous carbon

electrode microstructure

ABSTRACT

We explore different electrode microstructures and the associated implications on the electrochemical stability of activated carbon/lithium titanate ($\text{Li}_4\text{Ti}_5\text{O}_{12}$, LTO) composite electrodes by incrementally increasing the LTO content. At low LTO concentrations, the electrochemical stability is progressively improved with respect to neat activated carbon based electrodes. This trend is abruptly changed for high LTO concentrations (72 mass%) as the electrolyte starts to decompose unexpectedly far below the electrochemical stability boundaries of the single materials. We attribute this to a loss of electrical percolation and local degradation spots caused by peculiarities of the carbon distribution: Initially the sub-micrometer-sized LTO solely occupies spaces between the large, micrometer-sized activated carbon. With increasing LTO content the activated carbon particles get separated in an insulating LTO matrix. Electrochemical stability can be reestablished with electronic conduction paths of well distributed sub-micrometer-sized carbon black particles. By this way, cell degradation can be reduced and the cycle life of cells with high LTO concentration is prolonged from 10 to >36,000 cycles. Finally, we propose a simple method to distinguish cell fading caused by electrolyte decomposition from cell fading caused by poor electrical percolation.

© 2017 Elsevier Ltd. All rights reserved.

1. Introduction

Energy storage devices, like supercapacitors or lithium-ion batteries, have evolved to vital components for the steadily growing electrification [1]. Conventional supercapacitors consist of two opposing activated carbon (AC) electrodes and store energy via ion electrosorption processes [2]. By contrast, the operating principle of lithium-ion batteries is based on reversible faradaic reactions and associated Lithium intercalation/de-intercalation into the structure of the electrode materials [3]. State-of-the-art lithium-ion batteries utilize graphite anodes and are limited to carbonate electrolytes. These electrolytes are able to form a dense solid electrolyte interphase (SEI) at the graphite surface and therefore enable a stable cell operation [4]. Anode materials like lithium titanate ($\text{Li}_4\text{Ti}_5\text{O}_{12}$, LTO), which operate at high potentials

(>1 V vs. Li/Li^+), can circumvent the SEI formation, and access a wide variety of possible electrolyte alternatives. Additionally, LTO is characterized by its inherent safety [5], high Coulombic efficiency [6], negligible volume expansion during lithiation [6] and the cost effective raw materials for synthesis [7]. These unique material properties did lead to a substantial interest in the scientific community, resulting in a progressive improvement of LTO performance in recent years. Especially the challenging rate performance, caused by the low intrinsic electronic conductivity, can be considerably enhanced by the presence of an additional carbon phase. Besides a direct addition of a conductive carbon into the LTO electrode [8,9], it was proposed to synthesize LTO-carbon composite materials like carbon coated LTO [10,11], LTO confined in nanopores of activated carbon [12] or LTO grafted on carbon nanotubes [13–17], carbon nanofibers [7,18–20], or graphene [21–25].

One promising electrolyte alternative for LTO anodes is acetonitrile (ACN), due to its high lithium-ion conductivity (about five times higher as compared to conventional carbonate electrolytes) [2], low charge transfer resistance [26], and aluminum

* Corresponding author at: Department of Materials Science and Engineering, Saarland University, Campus D2 2, 66123 Saarbrücken, Germany.

E-mail address: volker.presser@leibniz-inm.de (V. Presser).

¹ ISE member.

current collector corrosion inhibition properties [27]. Moreover, it is well-known that the gas evolution in case of high surface area carbon electrodes is drastically reduced when switching from carbonate to ACN based electrolytes [28]. Therefore ACN electrolyte formulations could also be a conceivable solution to overcome the problematic gassing issues of LTO anodes [29–33]. Despite these advantages, ACN electrolytes for LTO-based lithium-ion batteries are not well investigated and an assessment method for defining the electrolyte electrochemical stability window (ESW) is in high demand.

Very recently, Lee et al. [34] reported a rate-dependent degradation of LTO based anodes. In this study, the capacity decrease and the increase in resistance during cycling were reported to be proportional to the current density. It was proposed that a high current density could lead to amplified gas generation (mainly H₂O and HF) due to electrolyte decomposition, but the underlying mechanisms are still under investigation [34].

These degradation mechanisms are important for high-rate electrode designs, like composite electrodes containing a mixture of AC and LTO. In the recent years, composite electrodes have attracted considerable interest in the scientific community and several material combinations were proposed [35–42]. The composite electrodes merge the advantages of capacitive (supercapacitor-materials, high power and cycle life) and Faradic (battery-materials, high capacity) charge storage mechanisms in one electrode. It has been suggested that a synergy between both materials can be obtained in the composite electrode, as the presence of AC increases the conductivity of the electrodes [36] and can act as a “shock absorber” for high currents [41]. Nevertheless, the interactions between battery-materials and nanoporous carbon (like AC) and the accompanied effects on the ESW remain poorly understood.

In the present study, we will address above-mentioned issues and uncover surprising interconnections between the electrochemical stability, electrode microstructure, electrical percolation, and rate-dependent cell degradation. In a first step, we will expand the electrolyte stability determination method of Xu et al. [43,44] to include the Faradaic charge storage contribution of LTO. For this purpose, the LTO content will be continuously increased, starting from a purely capacitive AC electrode. This is accompanied by drastic changes of the electrode microstructure, which in turn have stark implications on the ESW. Our findings shed new light on the traditional view of electrochemical stability, which is usually not considered in dependence of the electrode microstructure.

2. Experimental

2.1. Electrode materials and preparation

Steam-activated, coconut-derived activated carbon powder YP-50F was purchased from Kuraray Chemicals and will be referred to as AC. Carbon black type C-ENERGY C65, referred to as CB, was obtained from Imerys Graphite & Carbon. Commercial sub-

micrometer-sized lithium titanate (lithium titanate, spinel, nanopowder, <200 nm) was obtained from Sigma Aldrich.

In the following the different electrode compositions will be distinguished by a number, which reflects the LTO content in mass percent, followed by the addition “L” (Table 1). In some cases, 9 mass% of AC was replaced by 9 mass% CB and the respective electrodes were labeled with the supplement “C”. All counter electrodes are based on 0L compositions (i.e., no LTO, just AC). For some experiments, the LTO powder was manually grinded in a mortar prior to electrode processing to de-agglomerate LTO and the respective electrodes were labelled with the addition “-A”. The counter electrode and the working electrode were prepared by using a solvent based wet process [45]. In detail, AC and mixtures of AC with CB and LTO (Table 1) were mixed with isopropanol (for precise dosages see Table S1) in a DAC400 FVZ speedmixer at 2500 rpm. This treatment was followed by 7 min ultrasonic treatment and subsequent 4 min supplementary mixing at 2500 rpm. Afterwards, the slurry was transformed to a paste by adding 10 mass% (dry mass) of dissolved polytetrafluoroethylene (PTFE, 60 mass% solution in water from Sigma Aldrich) combined with speed-mixing at 800 rpm for 5 min. This paste was manually kneaded on a glass plate until the consistency of the paste was sufficiently viscous for further processing. An appropriate amount of electrode paste was placed between two untreated aluminum foils. This stack was then calendared down in a BLE682 battery lamination machine by applying a mass of 70 kg and a forward speed of 10 mm/s. The final electrode thickness was adjusted to $175 \pm 20 \mu\text{m}$ for the working electrode and $525 \pm 20 \mu\text{m}$ for the counter electrode. Two counter electrodes were pressed together to increase the overall CE capacity and reduce unwanted influences of side reactions occurring at the counter electrode.

A dry electrode preparation process inside an argon-filled glovebox (MBraun, O₂ and H₂O < 1 ppm) was used for quasi-reference electrodes (QRE) based on surface-functionalized AC (as outlined in more detail in Ref. [45]). Functionalization of AC was conducted in a nitric acid solution at 95 °C for 5 h according to our procedure described previously [45]. The functionalization of the AC introduces nitrogen and oxygen containing functional groups on the carbon surface, which drastically stabilize the QRE stability [45]. The functionalized AC and PTFE powder (PTFE 6 CN X, DuPont) were dried at 120 °C under vacuum (10^{-4} mbar) for 12 h before they were introduced into the glovebox. Afterwards, 0.45 g carbon powder was mixed with 0.05 g PTFE and grinded in a mortar until a dry paste forms. Small parts of the latter were then cut and used as QRE. For convenience and comparability to literature all QRE potentials stated in this work were calculated to the well-known Li potential (QRE-potential: 3.442 V vs. Li/Li⁺) [45].

2.2. Cell preparation and electrochemical measurements

Sheet resistance measurements were made with a custom-built spring-loaded four-point probe with blunt gold contacts (tip diameter: 1.5 mm, tip distance: 3 mm). For electrochemical testing,

Table 1
Overview of the employed electrode recipes and electrode labelling.

	LTO content (mass%)	AC content (mass%)	CB content (mass%)	PTFE content (mass%)
0L	0	90	0	10
0LC	0	81	9	10
40L	40	50	0	10
54L	54	36	0	10
72L	72	18	0	10
72L-A	72	18	0	10
72LC	72	9	9	10
72LC-A	72	9	9	10

we employed a custom-built polyether ether ketone (PEEK) cell with spring loaded titanium pistons as a three-electrode system, as described elsewhere [46]. Electrode discs with 12 mm diameter were punched out of the free-standing electrode film, separated by a glass-fiber separator (GF/D from Whatman) and placed on a carbon-coated aluminum foil current collector (Ranafoil, Toyo Aluminium K.K.). The assembled cells were dried at 120 °C for 12 h at 10^{-4} mbar and then transferred to an Ar-filled glovebox (MBraun, O₂ and H₂O < 1 ppm). After cooling, the QRE was placed on a compressed glass-fiber separator (GF/D, from Whatman) in a cavity close to the WE-CE electrode stack and contacted by a titanium wire. Afterwards the cells were vacuum-filled with 1 M LiClO₄ dissolved in acetonitrile (99.9%, water content <10 ppm, Acros Organics).

Electrochemical measurements were carried out using a potentiostat/galvanostat CTS LAB from BaSyTec. Cyclic voltammetric potential window opening experiments (CVPWOE) were recorded with a sweep rate of 1 mV/s by incrementally decreasing the vertex potential to 2.62, 2.37, 2.12, 1.87 V vs. Li/Li⁺ and then in 0.1 V steps until a Coulombic efficiency of 91 % was reached. Every polarization/de-polarization cycle was repeated three times and the Coulombic efficiency and *S*-value were calculated from the third cycle per the procedure described in Section 3.2.

We also calculated the equivalent series resistance (ESR) from the voltage drop after applying a 50 C pulse in polarization direction. For this purpose, the cells were polarized with 1 C to the respective potential to obtain ESR-voltage dependencies. Afterwards this potential was hold for 30 min, to ensure equilibrium conditions, followed by a 50 C pulse. The voltage drop was read out 100 ms after pulse initiation.

Galvanostatic charge/discharge cycling with potential limitation (GCPL) experiments were conducted between 1.17 V and 2.37 V vs. Li/Li⁺. The C-rate was calculated from the theoretical capacity of LTO (175 mAh/g, Ref. [6]) and the measured capacity of AC in the potential range from 1.17–2.37 V vs. Li/Li⁺ (36.74 mAh/g, determined from the CVPWOE) weighted with their respective content in the electrodes. In case of 1 C, the first 10 cycles were recorded in sequence followed by recording every 10th cycle for 500 cycles. A similarly approach was conducted for rates of 10 C (first 100 cycles in sequence, afterwards every 100th cycle until reaching 5,000 cycles). The cycle life was approximated by linear regression of the last 200 (1 C) respectively 2,000 (10 C) cycles for cells which did not reach the end of life (capacity drops below 80% of the initial capacity) after 500 respectively 5,000 cycles. The capacity values stated in this work are given with respect to the overall active mass (AC+LTO) and all results shown are average values of two cells. All electrochemical measurements were conducted at 23 ± 1 °C.

2.3. Structural characterization

For cross-section images the electrodes were cut with a scalpel and fixed with silver glue onto a Si-wafer. Afterwards, the deformed area of the electrode was removed by ion milling at 6 kV for 1.5 h with a IM4000Plus device from Hitachi. Scanning electron microscopy (SEM) analysis was carried out with a SUPRA VP system from Zeiss at an acceleration voltage of 5 kV. The samples were mounted on a carbon tab and sputter coated with a thin layer of platinum/palladium prior to the investigation.

3. Results and discussion

3.1. Electrode microstructure and electrical conductivity

In this work, we explore different electrode microstructures generated by mixing two distinct carbon powders (AC and CB) in

various ratios and combinations with sub-micrometer-sized LTO powder. AC consists of relatively large, micrometer-sized particles (d_{50} : 2.2 μm [47]) with an irregular shape and characteristic sharp edges (Fig. 1A). Contrary, CB is composed of spherical, loosely connected particles in the sub-micrometer range (d_{50} : 0.2 μm [47], Fig. 1B). AC is a primarily microporous material with a high specific surface area (SSA) of 1293 m²/g, while CB is predominantly non-porous with interparticle macropores having a SSA of 61 m²/g (both SSA were calculated via quenched-solid density functional theory) [45]. The SSA determination, porosity analysis, and a detailed characterization of the carbon powders can be found elsewhere [45]. The SEM micrographs of the LTO powder (Fig. 1C) reveal pronounced agglomeration of LTO primary particles (<200 nm, Fig. 1C) to form secondary particles in the micrometer range (~50 μm, Fig. S1A).

Fig. 2 shows cross sectional scanning electron micrographs of the electrodes. Carbon and LTO containing areas can easily be distinguished due to the large difference in atomic numbers between titanium (Z = 22) and carbon (Z = 6). The LTO phase shows

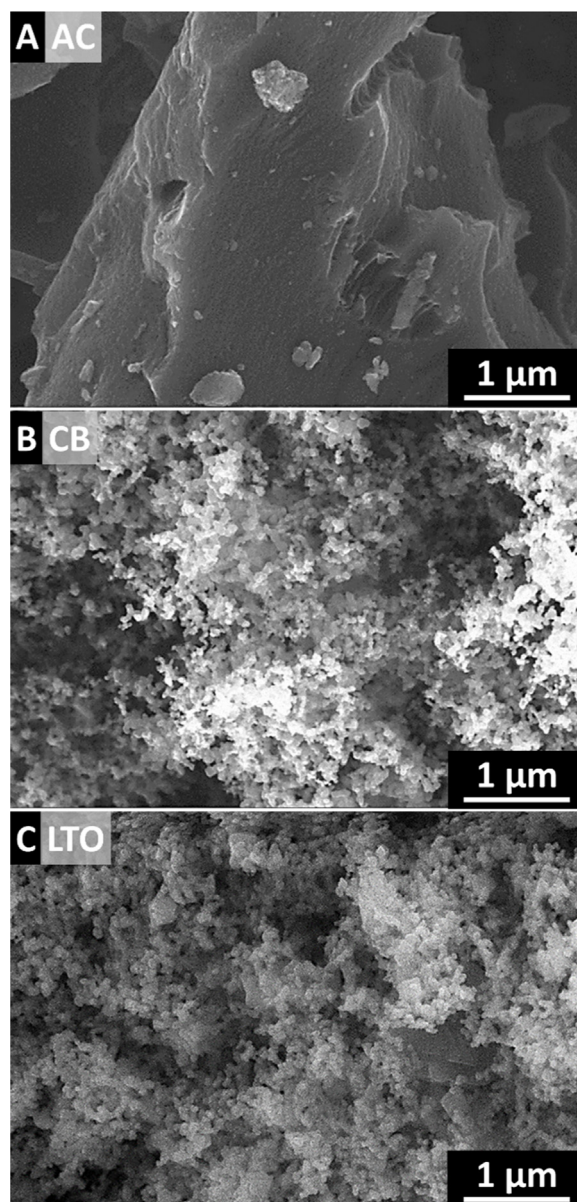


Fig. 1. SEM micrographs of (A) AC, (B) CB and (C) LTO powders.

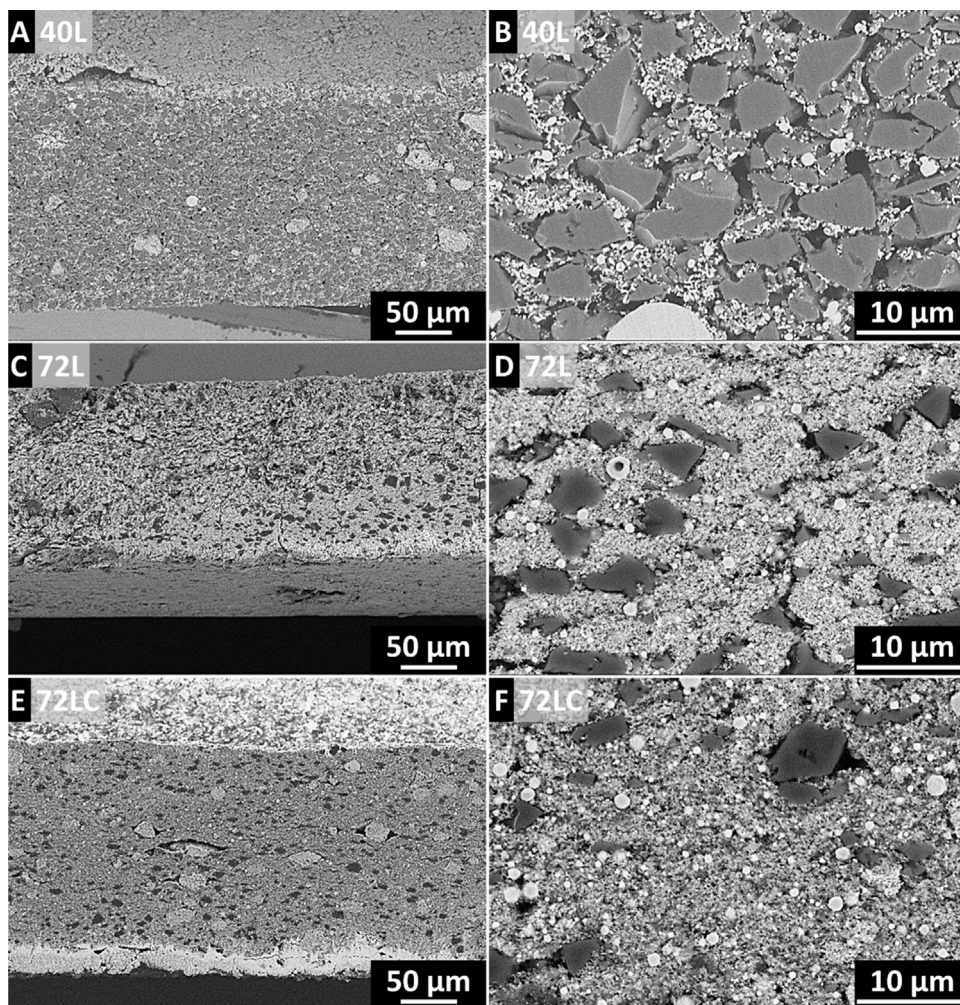


Fig. 2. SEM micrographs of the electrode cross section of 40L (A–B), 72L (C–D) and 72LC (E–F). Bright areas correspond to LTO particles, while dark areas can be ascribed to carbon particles (AC or CB).

pronounced SE backscattering as compared to the carbon phase and appears as bright sections in the SEM micrographs. Furthermore, AC can be identified due to its characteristic irregular shape and its sharp edges (Fig. 2B, D, F). In case of 40L-based electrodes, the sub-micrometer LTO particles mainly occupy the space in-between the larger AC particles. The AC particles are also in closer proximity, with some direct contacts amongst each other. This microstructure changes with rising LTO amount as the AC particles get separated and isolated in the LTO matrix (Fig. 2D). For 72LC, this isolation is further amplified due to the decreased overall amount of AC (Fig. 2F). In this case, a highly-interconnected network of CB particles in the LTO matrix is formed (Fig. 2F, Fig. S1B). The LTO phase tends to agglomerate to large secondary particles in the

micrometer range. These agglomerates can be seen in the electrodes optically (Fig. S2A, C). To disband the LTO agglomerates, the LTO powder was manually grinded in an agate mortar. As seen from light micrographs, this process drastically reduces the amount of large LTO agglomerates (Fig. S2B, D).

The resulting carbon distribution has a high impact on the electrical sheet resistance of the electrodes. The sheet resistance dramatically increases with increasing LTO content (Table 2). From 0L to 40L, the sheet resistance increases from $35 \Omega \text{ cm}$ to about $8000 \Omega \text{ cm}$ due to the electrical insulating nature of LTO [48]. For higher LTO contents, the electrical sheet resistance even exceeds the maximally measurable value. As discussed above, LTO fills the space in-between AC particles. Therefore, the electrical current can

Table 2

Polarization limits of negative electrodes calculated with the Coulombic efficiency = 91 % criterion and sheet resistance of the electrodes. For electrodes with intermediate passivation steps, polarization limits are determined for both cases when the Coulombic efficiency drops below 91 %.

	1st polarization limit (V vs. Li/Li ⁺)	2nd polarization limit (V vs. Li/Li ⁺)	Sheet resistance ($\Omega \text{ cm}$)
0L	$+0.785 \pm 0.032$	–	35 ± 5
0LC	$+0.779 \pm 0.003$	–	8 ± 1
40L	$+0.713 \pm 0.012$	–	8144 ± 4231
54L	$+0.686 \pm 0.016$	–	Out of range
72L	$+2.097 \pm 0.006$	$+0.621 \pm 0.008$	Out of range
72L-A	$+2.200 \pm 0.007$	$+0.641 \pm 0.006$	Out of range
72LC	$+0.554 \pm 0.026$	–	29 ± 3
72LC-A	$+0.542 \pm 0.004$	–	99 ± 11

only be passed at the few areas where AC particles are in direct contact to each other. Even low amounts of LTO already disrupt significantly the electrical pathways. The high statistical scatter of the sheet resistance for 40L electrodes can be ascribed to a strong local dependence of the few available electrical pathways. These pathways can be restored by adding small amounts of sub-micrometer-sized CB into the electrode (compare 72L and 72LC, Table 2). In this case, the electrical percolation of the electrode is provided by the well-distributed and interconnected cluster network of CB particles. Thus, the sheet resistance is reduced to a value comparable to 0L electrodes. The improvement of the electrical conductivity from 72L to 72LC is much more pronounced as compared to the one from 0L to 0LC. For electrodes only based on AC (0L), adding CB mainly improves the electrical conductivity by increasing particle-particle contacts [49]. In this case, the electrical current is also conducted through the AC particle network. For 72LC, the electrical current is conducted through the CB network without involvement of the insulating LTO matrix. The growth of electrical resistance from 72LC to 72LC-A is ascribed to the destruction of LTO agglomerates. This releases LTO sub-micrometer-sized particles into the electrode which were formerly bound in large agglomerates (Fig. S2). The rising content of sub-micrometer-sized LTO particles further disrupt the electrical percolation of the CB network and leads to the increase of sheet resistance in case of 72LC-A.

3.2. Generalization of the conventional S-value approach

The electrochemical stability window is defined as the potential range at which electrodes can be polarized in an electrolyte with negligible occurrence of irreversible Faradaic currents [50]. An operation of a device within these borders will consequently allow a stable cycling performance of the device. In case of electrical double-layer capacitors, ESW as high as possible are desired (due to the quadratic dependence of the energy on the potential). For Faradaic energy storage, the ESW should be sufficiently high to allow the reversible electrochemical processes taking place.

The ESW is highly dependent on the employed electrolyte solvent, electrolyte salt, electrode material and electrolyte or electrode contaminations [50]. It is impossible to accurately predict an ESW of a certain electrochemical system due to the variety of interactions between the different components [50]. An experimental determination of the ESW for a chosen electrode-electrolyte combination is indispensable. According to Xu et al. [43,44], the ESW of high surface electrodes can be determined with the help of cyclic voltammetric potential window opening experiments and a subsequent determination of a so called S-value [43,44]:

$$S = \frac{|Q_F|}{|Q_{nF}|} \quad (1)$$

where Q_F is the charge assigned to Faradaic electrolyte decomposition and Q_{nF} the non-Faradaic charge associated to reversible double layer formation. The cathodic charge Q_C (charge accumulated during polarization) and the anodic charge Q_A (charge extracted during de-polarization) can be expressed as [43,44]:

$$Q_C = Q_{nF} + Q_F \quad (2)$$

$$Q_A = Q_{nF} \quad (3)$$

Hence, (Eq. (2)) and (Eq. (3)) can be combined with (Eq. 1) and result in (Eq. 4) [43,44]:

$$S = \frac{|Q_C|}{|Q_A|} - 1 \quad (4)$$

Similar considerations for anodic territory lead to the definition of the S-value in anodic range [43,44]:

$$S = \frac{|Q_A|}{|Q_C|} - 1 \quad (5)$$

Usually the ESW is defined for the polarization potential at which S exceeds 0.1 (i.e., 10 % of the total charge inserted during polarization is consumed by parasitic electrolyte decomposition) [43,44]. The electrochemical implication of Eqs. (4) and (5) becomes clear when considering the definition of the Coulombic efficiency, that is, the ratio between charges extracted and inserted into an electrochemical device. In cathodic regime, the Coulombic efficiency is given by:

$$\text{Coulombic efficiency} = \frac{|Q_A|}{|Q_C|} \quad (6)$$

and in anodic regime, the Coulombic efficiency reads:

$$\text{Coulombic efficiency} = \frac{|Q_C|}{|Q_A|} \quad (7)$$

A generalized expression for the S-value, valid in both anodic and cathodic ranges, can be written as follows:

$$S = \frac{1}{\text{Coulombic efficiency}} - 1 \quad (8)$$

Therefore, the S-value is a function of the Coulombic efficiency and the conventional ESW criterion of $S = 0.1$ can be translated to a Coulombic efficiency of 91 %. The original definition of the S-value evaluation (Eq. (1)) implies its applicability to capacitive materials only, as the reversible charge Q_{nF} is ascribed to non-Faradaic processes. The charge storage mechanism in this case (i.e., double-layer charging) is known to be highly reversible and any decrease of the Coulombic efficiency necessarily must be associated to a charge loss caused by electrolyte degradation (if charge loss due to self-discharge, electrode degeneration or leakage currents is neglected). The presence of additional reversible Faradaic charge storage slightly complicates the S-value/Coulombic efficiency evaluation. This is due to the less reversible nature of Faradaic processes as compared to capacitive charge storage (e.g., due to material degradation caused by volume changes etc.). Consequently, any decrease of the Coulombic efficiency is a superposition of the charge loss due to the less reversible character of faradaic charge storage and the charge loss caused by parasitic electrolyte degradation. Hence, an S-value/Coulombic efficiency evaluation of the ESW must be performed with caution for Faradaic energy storage materials.

3.3. Electrolyte electrochemical stability and underpotential electrolyte decomposition

In this work, we extend the S-value/Coulombic efficiency evaluation to the ESW determination with additional faradaic charge storage contribution of LTO. The lithium intercalation of LTO is highly reversible, with only negligible volume expansion in the fully lithiated state ("zero strain material") [6]. Therefore, it is considered as one of the most stable lithium ion battery materials, proven to withstand thousands of charge-discharge cycles [51–53]. The irreversibility of the Faradaic charge storage process is negligible during one polarization-depolarization cycle as will be shown in this section. Accordingly, a decline of the Coulombic efficiency (increases of S-value) is mainly connected to currents induced by parasitic electrolyte degradation. We must emphasize that our results should not be regarded as a justification of an S-value/Coulombic efficiency evaluation for faradaic contributions per se. Such an evaluation mandatorily must be considered with

caution and separately investigated for every faradaic charge storage material.

Fig. 3A–D shows the cyclic voltammetric potential window opening experiments of electrodes containing different LTO contents. The cyclic voltammogram of the purely capacitive electrode (Fig. 3A) shows the typical rectangular shape characteristic for double layer charging [46,54]. The addition of LTO leads to sharp peaks at 1.2–1.8 V vs. Li/Li⁺ (Fig. 3B) caused by reversible Li intercalation/de-intercalation. These peaks increase in height and width with increasing LTO content (Fig. 3B–C), while the size of the rectangular shaped area diminishes. This can be explained by the different AC to LTO ratios, as the cyclic voltammogram of a composite electrode is a superposition of AC and LTO current contributions. Consequently a decreasing AC fraction (i.e., increasing LTO fraction) will lead to an attenuated AC contribution (decreasing size of rectangle) and an increasing LTO contribution (lithiation/de-lithiation peaks) in the cyclic voltammogram.

While the lithiation peak of 72 mass% LTO (72L) still follows this general trend (Fig. 3D), a different behavior is observed during de-lithiation: The peak of 72L based electrodes is being stretched in the low polarization region, resulting in a highly asymmetric peak shape. Peak widening and shifting are typical for overpotential development (caused by a deterioration of the redox process kinetics) [55]. Yet, such phenomena typically affect reduction and oxidation (i.e., lithiation, respective, de-lithiation) in roughly equal shares, without a drastic effect on peak symmetry [56].

This unique behavior of 72L must be based on LTO charge/discharge peculiarities. The lithiation of LTO is accompanied by a phase transformation of the Li-poor phase (Li₄Ti₅O₁₂) into the Li-rich phase (Li₇Ti₅O₁₂) starting from the outer shell of the LTO particle [8,57,58]. With continued lithiation, the Li-rich phase propagates further into the LTO particle, thereby transforming the entire particle into the Li-rich phase (Fig. 4A) [8,57,58]. During de-lithiation, the Li-rich phase is transformed into the Li-poor phase according to the same principles (Fig. 4A). Both phases are distinguished by inherently different electrical conductivities: Li₄Ti₅O₁₂ can be considered as an electrical insulator ($<10^{-13}$ S/cm

[48]), while Li₇Ti₅O₁₂ has a conductivity comparable to a semiconductor (about 10^{-2} S/cm [59]). This peculiarity combined with the microstructure of 72L (entire loss of electrical percolation, Section 3.1) leads to drastic differences during lithiation and de-lithiation: The electron transport through the LTO matrix is aggravated due to the missing percolation of carbon particles. At the beginning of charging, only an insignificant amount of current can be passed through the insulating LTO matrix. Only the LTO particles in direct contact to the current collector will get lithiated initially, thereby forming a conductive Li-rich layer on their outer shell. This introduces an electrical contact to neighboring LTO particles and the resulting cascade-like process, operative during the progression of lithiation, activates more and more conductive paths throughout the entire electrode. This process is different as compared with the mosaic particle-by-particle mechanism in LiFePO₄ electrodes [60,61], as both end-members (Li-rich and Li-poor phase) are electrical insulators in the latter case.

A similar mechanism occurs during de-lithiation. In this case, the electronic paths get deactivated rapidly after the initiation of de-lithiation due to the insulating nature of the de-lithiated phase formed at the outer shell of the LTO particles (Fig. 4A). Accordingly, an overpotential emerges, which is amplified during the advancement of de-lithiation as more electronic pathways become deactivated. This process results in the observed asymmetric peak shape. The electrical percolation can be re-established by exchanging a fraction of micrometer-sized AC of 72L-based electrodes with sub-micrometer-sized CB. This carbon is much more effective in providing a percolated conductive carbon network throughout the electrode compared to AC (Section 3.1). The cascade-like processes described above are circumvented in the case of 72LC, as electrons can be conducted without restrictions via the conductive and well-distributed cluster network of the CB particles. The symmetrical shape of the de-lithiation peak of 72LC is therefore restored (Fig. 3D).

We also have determined the ESR between the reference and the working electrode in dependence of the electrode polarization (Fig. 4B) to further underpin our conclusions drawn above. The ESR

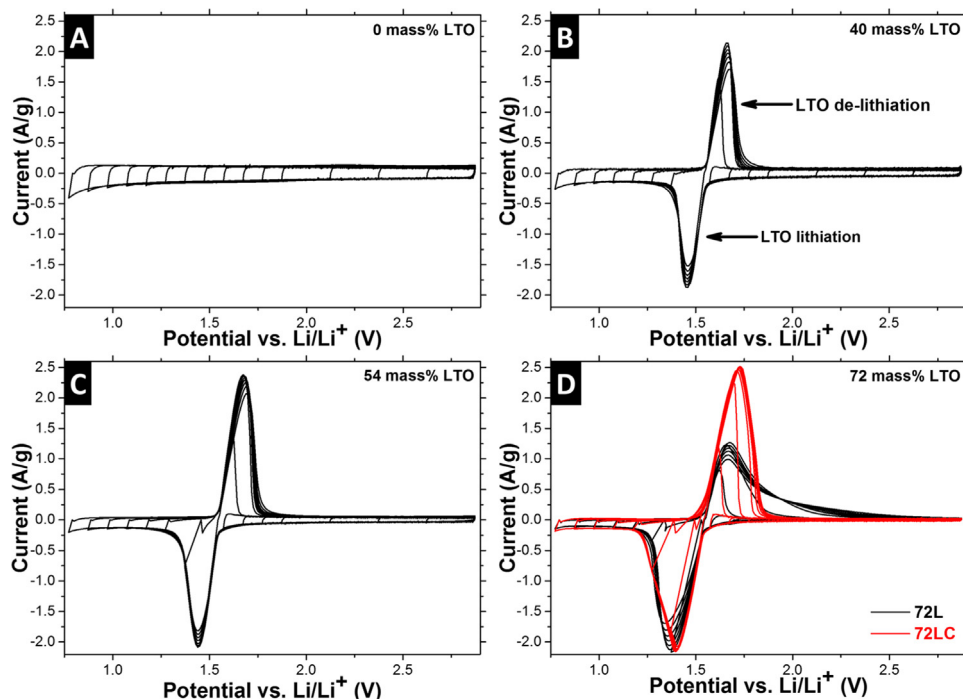


Fig. 3. Cyclic voltammetric potential window opening of (A) 0L, (B) 40L, (C) 54L, and (D) 72L respective 72LC up to a maximum polarization of 0.772 V vs. Li/Li⁺.

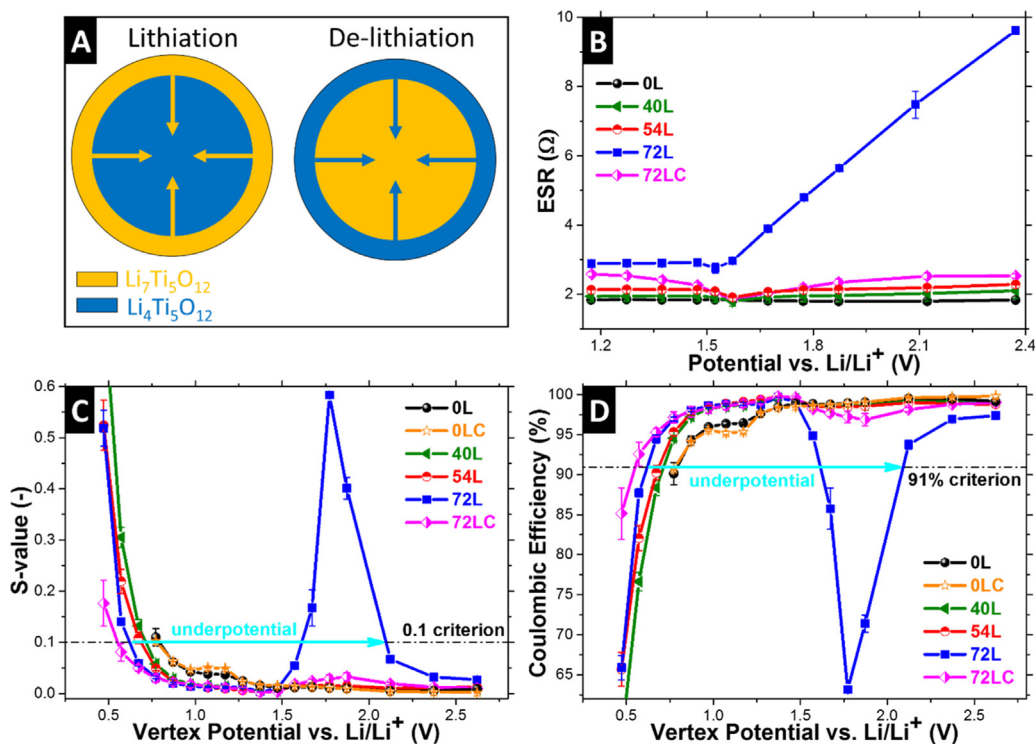


Fig. 4. (A) Simplified core-shell model of the spatial positioning of the present two phases in an LTO particle during lithiation and de-lithiation according to Takami et al. [8]. The propagation direction of the respective phase is indicated by the colored arrows. (B) Equivalent series resistance (ESR) between reference and working electrode in dependence of electrode polarization. (C–D). S-value and Coulombic efficiency plot calculated via cyclic voltammetric potential window opening (3rd cycle).

is a complex resistance composed of various electronic and ionic contributions of the electrode and the electrolyte [62]. In our case, most ionic contributions are constant from cell to cell. A careful quantitative analysis of the ESR will therefore allow a comparison of electronic conductivity differences. In case of 0L electrodes the ESR does not change during polarization (i.e., the electronic conductivity is not dependent on the state of charge). The addition of LTO slightly increases the ESR in case of 40L and 54L electrode compositions. In the low polarization regime (>1.8 V vs. Li/Li^+), this is mainly caused by an increase of the electrical resistance due to the substitution of conductive AC by less conductive LTO (Table 2 0L and 40L). With increasing polarization, the ESR slightly decreases and reaches a minimum at about 1.6 V vs. Li/Li^+ for 40L and 54L. We attribute this to a minor lithiation of a narrow surface layer of LTO outside of the potential regime for a bulk LTO phase transformation [5] and the associated decrease of the electrical resistance due to the superior conductivity of the Li-rich phase. At about 1.6 V vs. Li/Li^+ , bulk LTO is lithiated and an additional resistance term arises with further polarization (ESR increases). This term indicates an increase of the ionic diffusion resistance of the LTO lattice when lithiating beyond $\text{Li}_7\text{Ti}_5\text{O}_{12}$ composition [58,63,64]. For 72L based electrodes, a fivefold higher ESR is measured in the low polarization regime, reflecting the low degree of electrical percolation. With increasing polarization, we see a severe drop of the ESR for 72L, which supports the cascade-like effect described above. In case of 72LC, the percolation is re-established by a cluster network of sub-micrometer-sized CB particles and the ESR is decreased by a factor of about five. These trends are in-line with the sheet resistance measurements of the electrode films (cf. 72L with 72LC in Table 2) and the peak shape behavior during cyclic voltammetry.

These differences between 72L and 72LC are comparable to the peculiarities of single LTO particles and LTO-containing composite electrodes (LTO, carbon and binder): Single LTO particles are

characterized by a sharp lithiation and a broad de-lithiation peak, whereas the composite electrodes do not show differences between these peaks [8]. In that regard, 72L based electrodes do behave more comparable to single LTO particles due to the missing carbon percolation and the abundant LTO-LTO particle contacts.

The S-value and Coulombic efficiency is calculated from cyclic voltammetric potential window opening (Fig. 3A–D) via the procedure described in Section 3.2 and the results are shown in Fig. 4C–D. In the following, we refer to the Coulombic efficiency due to its more intuitive electrochemical definition and its comparability to the galvanostatic measurements in the last section. We note that the calculation of an S-value for GCPL is not common. For the purely capacitive electrode 0L and 0LC the Coulombic efficiency gradually decreases with increasing degree of polarization (Fig. 4D). The conventional criterion for the ESW of 91% Coulombic efficiency is reached for both material combinations at about 0.8 V vs. Li/Li^+ (Table 2). Thus, no significant influence of CB on the electrochemical stability can be verified. Nevertheless, the 91% Coulombic efficiency criterion should only be considered as an appraisalment of the rough stability boundaries and not as an absolute value. For example, passivation effects cannot be uncovered by a simple Coulombic efficiency evaluation. A high initial Coulombic efficiency might stabilize with advancing operation time as the surface gets passivized (Section 3.4). Nevertheless, the Coulombic efficiency criterion fits to the abrupt, exponential decrease of Coulombic efficiency (starting point of extensive electrolyte decomposition). This can be visualized by the appearance of a decomposition peak at high degrees of polarization when comparing Fig. 3B–C (Coulombic efficiency $>91\%$) with Fig. 3A–C (Coulombic efficiency $<91\%$).

The addition of LTO increases the stability as can be seen by the higher Coulombic efficiency of 40L electrodes, especially at potentials <1.5 V vs. Li/Li^+ . More LTO (40% to 54%) further improves the stability in this potential range. We conclude that the

irreversible nature of Faradaic charge storage only contributes to a negligible fraction to the Coulombic efficiency as the presence of LTO even improves the Coulombic efficiency. Changes of the Coulombic efficiency are mainly connected to currents induced by parasitic electrolyte degradation and a first estimation of the ESW via the Coulombic efficiency is justified. Sample 72L is found to be an outlier from the general trends. For 72L based electrodes, we see a spike in inefficiency in the low polarization region (>1.5 V vs. Li/Li^+). With increasing polarization, the Coulombic efficiency increases, followed by a second decline until reaching the polarization limit.

The inefficiency spike can be reduced when restoring the electrical percolation as can be seen for 72LC based electrodes in Fig. 4D. Moreover, the drastic decrease of the Coulombic efficiency emerges only when polarizing/de-polarizing in a potential regime not sufficiently high to lithiate bulk LTO, that is, when no electrical percolation of the Li-rich LTO phase can be provided (lithiation starts at about 1.6 V vs. Li/Li^+). This suggests a connection between the inefficiency spike and electrical percolation of the electrode. With increasing polarization beyond 1.6 V vs. Li/Li^+ the progressively growing electrical percolation provided by the Li-rich phase combined with electrode passivation effects (see Section 3.4) can stabilize the Coulombic efficiency until the final polarization limit at about 0.6 V vs. Li/Li^+ is reached (Table 2). The strong decrease of the Coulombic efficiency at relatively low polarization in the case of 72L implicates electrolyte degradation far within the stability of the individual materials, as the first polarization limit of 72L is shifted by about 1.3 V (Table 2) compared to the most instable electrode (i.e., 0L and 0LC). In the following, this phenomenon will be referred to as “underpotential electrolyte decomposition” (Fig. 4C–D), using the common definition of underpotential deposition phenomena, that is, the electrolytic deposition of metals at potentials below the equilibrium potential [65]. We will give a more detailed explanation of the observed underpotential electrolyte decomposition for 72L in the next section.

3.4. Interconnections of C-rate, electrode microstructure, and electrochemical cycling stability

The conventional ESW criterion according to Xu et al. [43,44] defines the electrolyte stability at the point where the Coulombic efficiency falls below 91% ($S=0.1$). A device which operates both of its electrodes to their maximum ESW (determined at the point where Coulombic efficiency $< 91\%$) will further mitigate the device Coulombic efficiency to about 83%, as both electrodes contribute to the efficiency loss. Referring an electrochemical energy storage device with such a low Coulombic efficiency to be stable might appear counterintuitive in the first place. Yet, this approach has proven its effectiveness throughout literature [43,44,66–68]. This contradiction can be explained by a passivation with increasing cycle number and/or time spend in a polarized state. Hence, a low initial Coulombic efficiency can stabilize with increasing operation time of the device. We see that, for example, for the Coulombic efficiency of 72L based electrodes during the CVPWOE, which is dependent on the cycle evaluated and increases with increasing cycle number (Fig. S4).

Although passivation effects are likely dependent on the electrochemical system under investigation, two general reasons might be conceivable: (i) Destruction/degradation of highly reactive areas due to the applied potential (e.g., areas in close contact to the electrolyte); (ii) coating of highly reactive areas and/or the active material surface area by electrolyte degradation products which prevent further electrolyte decomposition (similar to the solid electrolyte interphase formation on graphite anodes [69]). For example, it is well-known that polarization of AC, when using TEA- BF_4 in propylene carbonate (PC) or acetonitrile (ACN), leads to distinct surface deposits which are highly dependent on the solvent and polarization regime applied [47,70].

The ESW determination via Coulombic efficiency evolution during CVPWOE is highly dependent on the experimental conditions applied due to the presence of passivation effects

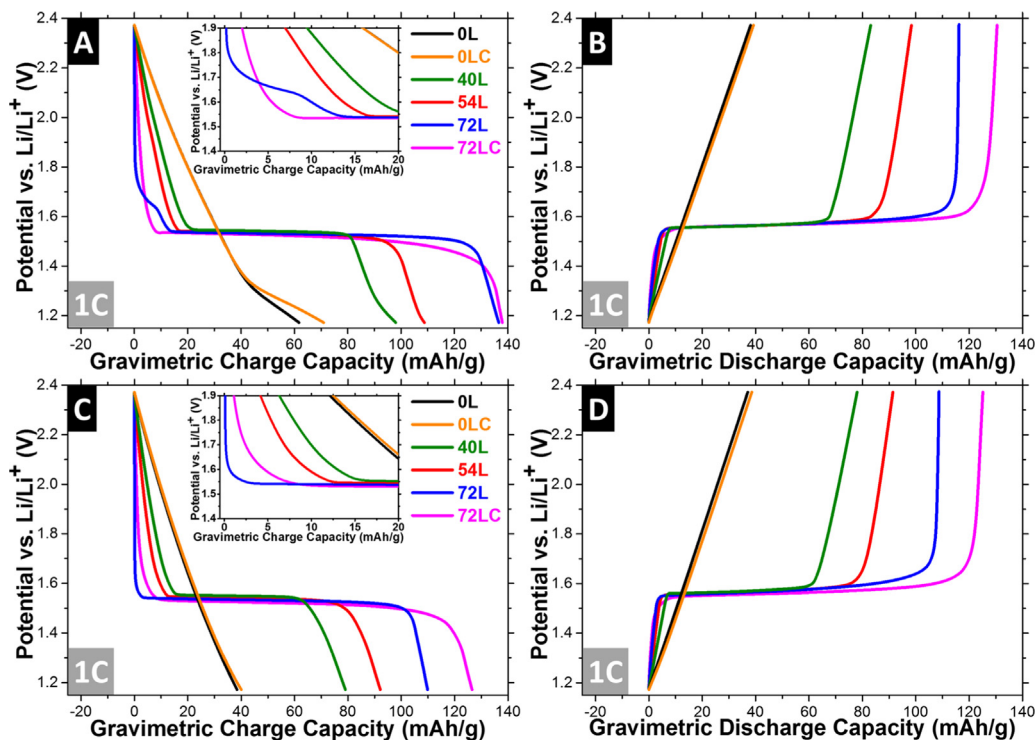


Fig. 5. Galvanostatic charge and discharge curves of the 1st (A–B) and 10th (C–D) cycle measured at 1C. The insets of (A) and (C) show a higher magnification of the charge curves in the area between 1.4 and 1.9 V vs. Li/Li^+ .

and their dependence of electrochemical prehistory (cycle used for evaluation, polarization step interval and cycle numbers applied per polarization step). Thus, it should serve as a first approximation of the rough ESW boundaries and a long-term measurement is needed for a robust assessment of the electrolyte stability. We applied GCPL in a potential range of 1.17–2.37 V vs. Li/Li⁺ (Figs. 5 and 6), which are well within the stability criterion of Coulombic efficiency > 91% for all sample materials (Fig. 4D). For the OL and OLC based electrodes the expected linear slope resulting from the purely capacitive double layer charge storage mechanism can be observed at 1 C (Fig. 5). During the first polarization (Fig. 5A), this constant linear slope is interrupted at a polarization of about 1.3–1.4 V vs. Li/Li⁺ and merges into a second area with mitigated sloping in the high polarization region. A deviation from the linear capacitive behavior indicates that charge is consumed by additional processes other than ion electrosorption. This charge is dissipated to parasitic electrolyte degradation as can be concluded from the complete lack of reversibility during depolarization (Fig. 5B). With increasing cycle number, the second area vanishes due to the passivation of the electrode, resulting in a purely capacitive behavior over the entire polarization regime (Fig. 5C). The second area is differently pronounced for OL and OLC and the formerly similar voltage profiles start to separate from each other (Fig. 5A).

The presence of a few percent of CB has a strong impact on the irreversible charge consumed during the first cycle of AC based electrodes. The impact on the long-term performance of admixed carbons was investigated before for 1 M TEA-BF₄ in ACN and composite electrodes were always found to be inferior to the respective single carbon based electrodes [47]. This was ascribed to water formation when admixing carbons with different basic and acidic surface groups [47]. In our case, a different mechanism must be responsible as the presence of CB generally improves (Fig. 7A) or does not alter (Fig. 7B) the long-term stability compared to electrodes just based on AC. Additionally, the starting potential of

electrolyte degradation roughly aligns for both OL and OLC based electrodes (Fig. 5A), which indicates similar degradation origins. The differences of irreversible charge consumed during the first cycle for OL and OLC might be connected to the improved conductivity of OLC (Table 2). This could accelerate the kinetics of Faradaic electrolyte degradation (i.e., reduce the overpotential) and increase the electrolyte decomposition during the first cycles. With increasing cycle number the electrode get passivated and the differences of irreversibility between OL and OLC become negligible (Figs. 5 A, C and 7 C). These trends for OL and OLC are visible in the Coulombic efficiency evolution of the CVPWOE (Fig. 4D) by the inflexion point of the Coulombic efficiency between 1.17–1.27 V vs Li/Li⁺ and the general lower Coulombic efficiency for OL for the subsequent two polarization scans (afterwards the surface gets passivated and the Coulombic efficiency evolution of OL and OLC coalesce again).

The addition of LTO introduces a potential plateau in the voltage profiles (Figs. 5 and 6) caused by the two-phase reaction of LTO [58]. As expected, this plateau increases with increasing LTO content. Simultaneously, the slope of the linear region shrinks due to the decreasing fraction of AC. Both effects are caused by the different AC to LTO ratios, as the voltage profile of the composite electrode is a superposition of AC and LTO contributions [37,39]. Consequently a decreasing AC fraction (i.e., increasing LTO fraction) will lead to an attenuated AC contribution and an increasing LTO contribution in the voltage profile.

The inflexion point of the linear slope in the high polarization region (after LTO lithiation, Fig. 5A) is still visible for 40L and 54L based electrodes; however, with progressively decreasing severity. It can be assumed that the LTO surface is less susceptible to electrolyte degradation, which is in-line to the CVPWOE observations described above. According to Fong et al. [71] the electrolyte decomposition rate scales with the surface area. Therefore, the inferior stability of AC could be connected to its considerably high surface area. Additionally, the inflexion point of the potential

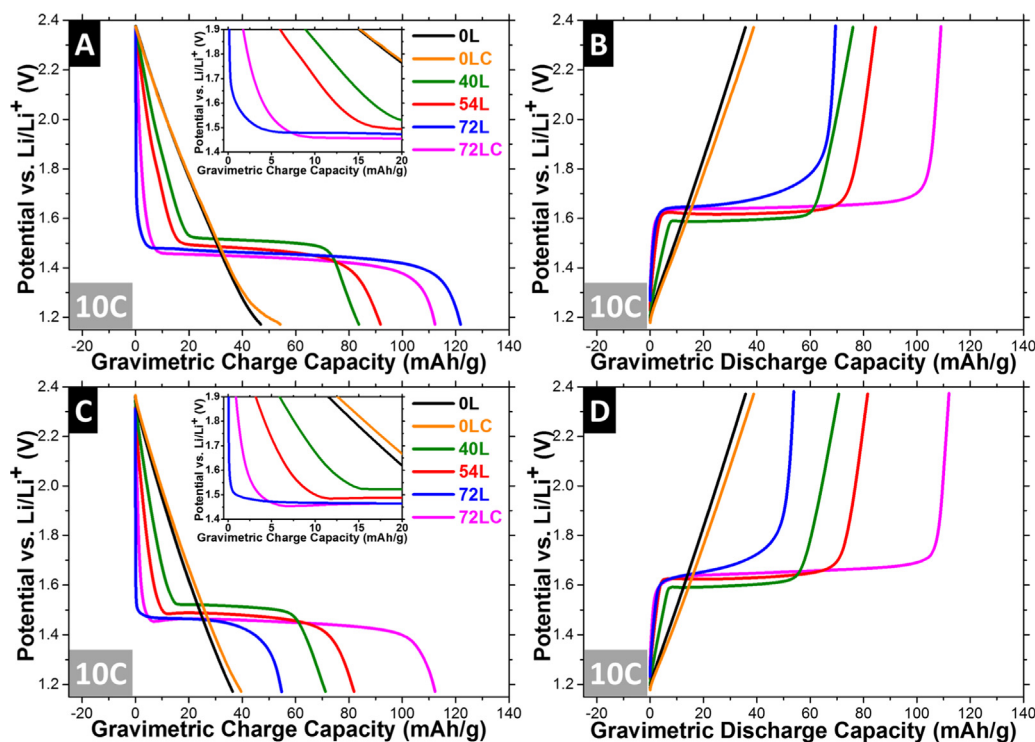


Fig. 6. Galvanostatic charge and discharge curves of the 1st (A–B) and 10th (C–D) cycle measured at 10 C. The insets of (A) and (C) show a higher magnification of the charge curves in the area between 1.4 and 1.9 V vs. Li/Li⁺.

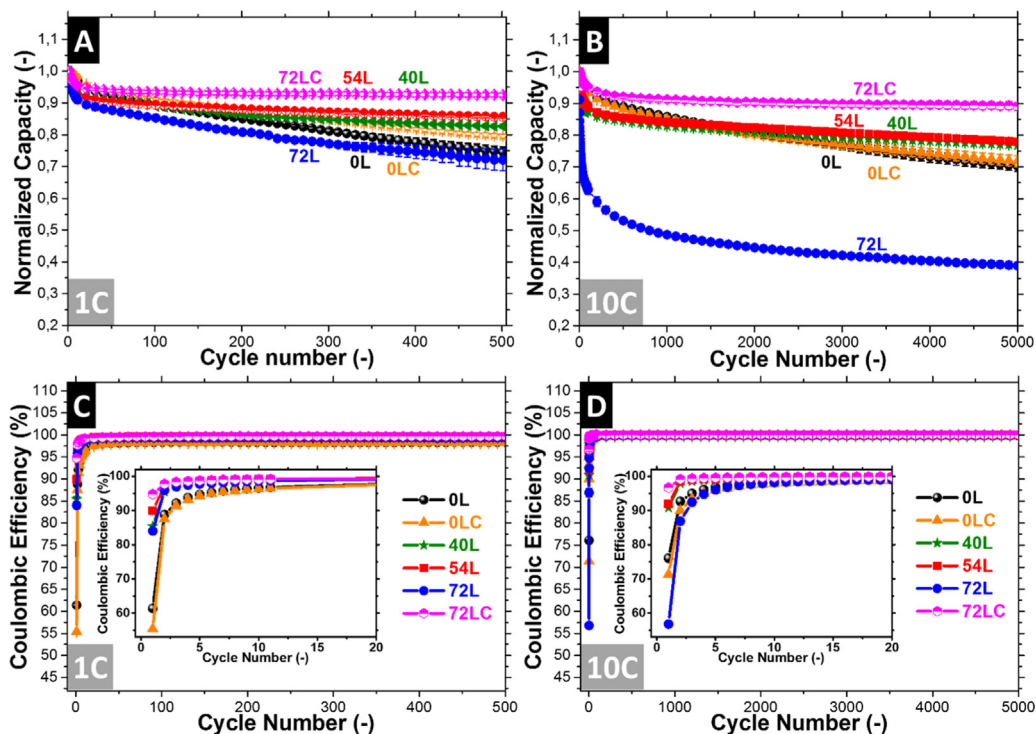


Fig. 7. Electrochemical cycling stability measured at charging/discharging rates of 1 C (A) and 10 C (B). Calculated Coulombic efficiency at 1 C (C) and 10 C (D).

profile in the high polarization area are shifted from about 1.4 V (0L, 0LC) to 1.3 V (40L) vs. Li/Li⁺, due to the overpotential caused by the increasing fraction of LTO particles and the exchange of relatively reactive AC with less reactive LTO. Like 0L and 0LC electrodes, the inflexion point vanishes with increasing cycle number (i.e., electrodes are passivated). For 72L-based electrodes, the underpotential electrolyte decomposition can be observed prior to LTO lithiation (see inset of Fig. 5A), in agreement with CVPWOE. With increasing cycle number, this underpotential electrolyte decomposition vanishes (Fig. 5C, inset) due to the passivation of the electrode surface. The re-establishing of the electrical percolation (72LC) leads to the circumvention of the underpotential electrolyte decomposition phenomena.

An elevation of the C-rate from 1 C (Fig. 5) to 10 C (Fig. 6) insignificantly alters the charging/discharging characteristics of the purely capacitive electrodes 0L and 0LC due to the fast charge

storage processes. Almost the same discharge capacity can be maintained at 10 C as compared to 1 C (Table 3 and 4). The rate-capability of 0LC is slightly superior to 0L electrodes due to the improved electrical conductivity. Compared to 1 C, the inflexion point of the linear area due to parasitic electrolyte degradation of 0L and 0LC is shifted to higher polarizations and vanishes entirely for 40L and 54L. Both effects could be caused by the increased overpotential of electrolyte reduction with increasing C-rate. At 10 C, the characteristic two phase plateaus of the LTO doped electrodes start to lose their alignment (Figs. 5 and 6). During the first polarization (Fig. 6A), a clear correlation of the AC content and the plateau position can be found: A decreasing AC amount generally shifts the LTO plateau to higher polarizations (40L < 54L < 72L < 72LC). Consequently, AC decreases the overpotential of the Faradaic LTO lithiation reaction. This cannot solely be explained by the increase of electrical resistance with increasing LTO content,

Table 3

Gravimetric discharge capacity and Coulombic efficiency of the first cycle and cycle life at 1 respective 10 C of the various electrode composition investigated. The cycle life is reached at the position of discharge capacities below 80% of the respective initial values. "*" denotes estimated cycle life values for cells withstanding 500 respectively 5,000 without dropping below 80% of the initial cell capacity cycles at 1 C respective 10 C.

	C-rate	Discharge capacity 1st cycle (mAh/g)	Coulombic efficiency 1st cycle (%)	Cycle life (cycles)
0L	1C	38.08 ± 0.03	61.40 ± 0.37	330
0L	10C	35.41 ± 0.29	76.07 ± 0.06	2,200
0LC	1C	39.28 ± 0.08	55.39 ± 0.16	480
0LC	10C	38.15 ± 0.63	71.33 ± 0.17	2,130
40L	1C	83.96 ± 0.86	85.42 ± 0.61	730*
40L	10C	76.41 ± 0.38	90.87 ± 0.02	2,550
54L	1C	98.85 ± 0.49	89.98 ± 0.44	1,240*
54L	10C	85.54 ± 1.07	91.97 ± 0.05	3,560
72L	1C	116.16 ± 1.72	84.09 ± 0.81	230
72L	10C	68.05 ± 1.43	56.80 ± 0.23	10
72L-A	1C	109.68 ± 0.83	81.89 ± 0.61	50
72L-A	10C	48.37 ± 1.08	57.55 ± 4.05	10
72LC	1C	131.07 ± 0.58	94.77 ± 0.22	7,180*
72LC	10C	104.84 ± 4.21	96.69 ± 0.48	36,380*
72LC-A	1C	134.46 ± 0.01	91.96 ± 1.10	900*
72LC-A	10C	112.26 ± 0.12	92.88 ± 0.45	3,210

Table 4

Ratios between 10 C and 1 C of the gravimetric capacity and cycle life for the different electrode compositions. “Q” stands for the gravimetric discharge capacity, “CL” for cycle life.

	Q_{10C}/Q_{1C}	CL_{10C}/CL_{1C}
0L	93	6.67
0LC	97	4.44
40L	91	3.49
54L	87	2.87
72L	59	0.04
72L-A	44	0.20
72LC	80	5.07
72LC-A	83	3.57

especially when comparing the plateau position of the low resistive 72LC with high resistive 72L. Therefore, a synergy effect between the charge storage mechanisms of AC (double layer charging) and LTO (faradaic Li-intercalation reactions) might indeed be operative, as proposed previously by Wang et al. [41]. During the de-polarization (Fig. 6B), the overpotential shifts the LTO de-lithiation reaction to higher potentials. Hence, the sequence of LTO plateaus positions is inverted. 72L is found to be an outlier from the general trends during the de-lithiation as the LTO plateau starts to get distorted into the low polarization region with increasing charge extracted (Fig. 6B). A greatly reduced rate capability results (Table 3). These kinetic effects do also reflect in the rate capability of the different electrode compositions (Table 4). We conclude that the deactivation of the electronic paths, provided by the Li-rich LTO phase, is more problematic during fast delithiation.

With increasing cycle number, the LTO lithiation plateau of 72L (Fig. 6B) progressively drifts to higher polarizations and even reaches comparable values as 72LC (Fig. 6A, C). This decrease of the electrochemical kinetics of 72L could be attributed to a more pronounced cell aging compared to 72LC, for example caused by the formation of surface films on the electrode materials.

From the GCPL measurements, we also calculate the discharge capacity and Coulombic efficiency in dependence of the cycle number (Fig. 7). The capacity is normalized with respect to the discharge capacity of the first cycle to eliminate the interfering capacity variations of the electrodes caused by the different LTO content (for the absolute capacity values see Table 3). During the first cycles, a strong decrease of the capacity becomes visible for all electrodes at all surveyed rates (Fig. 7A–B). Afterwards, the capacity stabilizes for the subsequent cycles, dependent on the electrode composition and C-rate. When comparing the Coulombic efficiency values (Fig. 7C–D), we see a progressive increase of Coulombic efficiency during cycling. In alignment with CVPWOE (Section 3.3), we can correlate any decrease of the Coulombic efficiency to charge dissipated for parasitic electrolyte decomposition. The strong decrease of the electrode capacity during the initial cycles is caused by excessive electrolyte decomposition on the highly reactive, “fresh” electrode surface. This process is attenuated with increasing electrode passivation and the performance stabilizes, as described above. During the first cycles, the Coulombic efficiency of 0L and 0LC strongly decreases compared to the CVPWOE measurements with a comparable polarization maximum (Fig. 4D). In the case of GCPL, 0L- and 0LC-based electrodes are characterized by low first cycle Coulombic efficiencies in the range of about 55–60% at 1 C. With proceeding cycle number, the Coulombic efficiency of 0L and 0LC constantly increases during GCPL. Thus, the differences between GCPL and CVPWOE for 0L and 0LC are caused by passivation effects due to the prehistory which can obscure the Coulombic efficiency evaluation during CVPWOE (electrolyte can already react with the surface during the first low polarization cycles of the CVPWOE). Even after

500 cycles at 1 C, the Coulombic efficiency does not exceed 98.4% for 0L and 0LC (99.7% for 72LC for comparison).

The constant, yet attenuated Coulombic efficiency (i.e., constant electrolyte reduction) is also reflected in the low cycle life of 0L and 0LC based electrodes (Table 3). With increasing LTO fraction, the overall Coulombic efficiency can be improved (Fig. 7C–D). At the same time, the cycle life at 1 C is raised by a factor between two (40L) to five (54L), which again reflects the superior stability of LTO to withstand electrolyte decomposition. For 72L, this trend is radically interrupted, very likely due to the observed presence of underpotential electrolyte decomposition in this case. The Coulombic efficiency stabilizes for 72L with increasing cycle number, most likely connected to the formation of a passivation layer on the surface. This passivation seems to be different as compared to the other electrode compositions. Stark differences in the layers formed can be assumed, very likely due to the different onset-potentials of electrolyte reduction. For example, it is well-known that the chemical composition of the solid electrolyte interphase (SEI) constructed on graphite anodes is highly dependent on the applied voltage [69]. A similar behavior could be assumed in our case. However, a detailed characterization of such surface films is beyond the scope of this study. Additionally, our results demonstrate that underpotential electrolyte decomposition should be avoided at any price, as can be seen by the 31-fold increase of the cycle life when restoring the electrical percolation by changing the electrode composition from 72L to 72LC (at 1 C, Table 3).

With increasing C-rate, the cycle life of 0L and 0LC drastically increases. We associate this to the reduced fraction of time spend within the high polarization regime at higher rates [72] and the associated mitigated charge loss to parasitic electrolyte reduction per cycle. When we compare the ratio CL_{10C}/CL_{1C} of the cycle life during GCPL at 10 C and 1 C (Table 4), we detect remarkable coherences. By increasing the LTO fraction the ratio decreases from 0L to 54L and drops below one for 72L. This ratio reflects the ability of an electrode to superiorly resist either fast ($CL_{10C}/CL_{1C} > 1$) or low ($CL_{10C}/CL_{1C} < 1$) charge/discharge conditions. High values indicate a cell fading primarily caused by electrolyte instabilities due to the reason explained above. Interestingly the increased LTO fraction renders the electrodes progressively more susceptible to high rate cycling. The immediate conclusion would be that LTO is intrinsically inferior to high rate cycling as compared to AC. However, a comparison to 72LC based electrodes reveals the real origin of the inferior stability at high rates: The decrease of electrical percolation. We associate this to inhomogeneous charge or voltage distributions inside the electrode due to insufficient conductive pathways in case of AC dependent percolation.

Fig. 8 shows a simplified two-dimensional model of the electrode microstructure and the charge-distribution during the onset of LTO lithiation to illustrate a possible origin of these inhomogeneities. If the electrical conduction paths are provided by relatively big carbon particles, like AC, only LTO particles in close contact to the carbon network are charged initially (Fig. 8A). With progressed charging, the Li-rich phase can provide the electrical percolation to lithiate neighboring LTO particles. In this case, the lower conductivity of $Li_7Ti_5O_{12}$ compared to carbon could lead to inhomogeneous charge or voltage distributions inside the electrode. A strong local dependence of the degradation rate results, whereby well-connected areas can act as local spots with accelerated degradation rate. This effect is most pronounced prior to the onset of lithiation and will mitigate during continuous charging due to the increasing fraction of the conductive Li-rich phase. For a well-distributed cluster network of carbon particles in the sub-micrometer range a drastically enhanced fraction of LTO-carbon contacts are established. The electrode is charged more

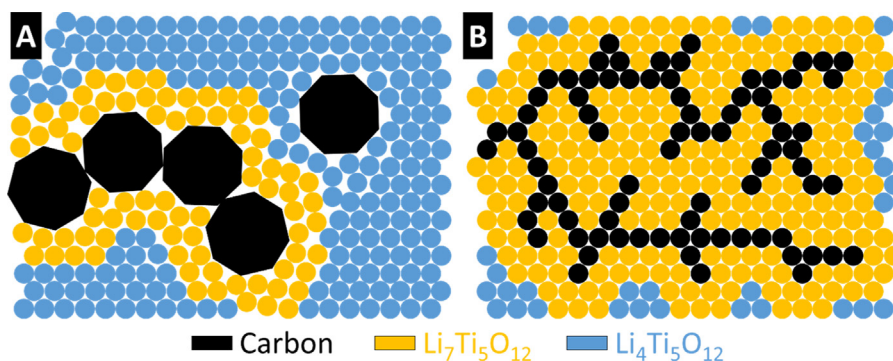


Fig. 8. Simplified two-dimensional model of electrode cross-sections in case of (A) conduction paths provided by relatively big carbon particles (e.g., AC) and (B) electrical conduction via a well distributed cluster network of carbon particles in the sub-micrometer range (e.g., CB). The area ratio of carbon-to-LTO ($\text{Li}_4\text{Ti}_5\text{O}_{12} + \text{Li}_7\text{Ti}_5\text{O}_{12}$) is identically for both cases. Only LTO particles in close contact to the carbon network are assumed to get charged initially.

homogeneously in this case, as a much greater fraction of LTO gets lithiated initially (Fig. 8B) and the local degradation spots are circumvented. These processes will be amplified during high rate cycling due to the higher currents applied and the smaller timescale for every charge-discharge cycle (the distribution/homogenization of charge and potential differences over the electrode area are counteracted).

Ultimately, this process results in the underpotential electrolyte decomposition for the extreme case of the entire loss of electrical percolation, already at relatively low rates. The decrease of the $\text{CL}_{10\text{C}}/\text{CL}_{1\text{C}}$ ratio with rising LTO content indicates a progressive transformation from cell fading primarily caused by electrolyte decomposition (0L) to cell fading due to the loss of electrical percolation (72L). By restoring the electrical percolation, the cell fading returns to primarily electrolyte decomposition for 72LC. In this case, the cycle life at 10 C is raised by a staggering factor of 3,600 from 72L to 72LC. This demonstrates the tremendous impact of the carbon distribution on the electrochemical stability of LTO-based electrodes.

We also have investigated the effect of the LTO agglomerates contained in the composite electrodes (Fig. S2A, C). Initially one would expect a more stable cell operation from the de-agglomerated electrodes due to their higher degree of homogenization (Fig. S2B, D). When comparing the GCP measurements (Fig. S5) we can see exactly opposing trends: De-agglomeration decreases the electrochemical cycling stability for all electrodes at all rates (Fig. S5 and Table 3). Simultaneously the $\text{CL}_{10\text{C}}/\text{CL}_{1\text{C}}$ ratio of 72LC-A decreases as compared to 72LC. We can now associate this with the inferior electrical percolation after the de-agglomeration due to the rising content of sub-micrometer sized LTO, which can disrupt electric conduction paths (Section 3.1). A less homogeneous electrode charging results, which in turn decreases the electrochemical stability according to the processes described above. Nevertheless, the decreased electrical percolation cannot explain these results alone, as the cycle life of 72LC-A is in the same order as 54L (which has a drastically higher resistance, Table 2). Additional cell fading mechanisms, connected to the de-agglomeration of LTO, are therefore very likely. While a detailed investigation of such effects exceeds the scope of this study, we believe that a partial destruction of LTO particles and the therefore increased and/or more reactive surface area are conceivable. Follow up work should focus on such effects to further illuminate the underlying degradation mechanisms in this case.

4. Conclusions

In the present study, we have revealed the impact of the electrode microstructure and electrical percolation on the

electrochemical stability of LTO based energy storage devices. For this purpose, we have continuously increased the LTO content of activated carbon-based electrodes. Initially the sub-micrometer-sized LTO occupies the spaces between the micrometer-sized activated carbon particles. At very high LTO concentrations (72 mass%) this microstructure is significantly altered as the activated carbon particles start to get separated in an insulating LTO matrix.

The microstructure transformation does affect the electrochemical stability of the electrodes. Initially an increasing LTO content was found to enhance the electrochemical stability as compared to neat activated carbon. We attribute this attenuated reactivity of LTO to the generally lower surface area as compared to activated carbon. At high LTO concentrations (72 mass%) an abrupt disruption of this trend can be observed and the electrolyte starts to decompose deep within the stability boundaries of neat activated carbon and all other activated carbon LTO composite electrodes. We attribute this underpotential electrolyte decomposition to a loss of electrical percolation and local degradation spots caused by inhomogeneous charge or voltage distributions throughout the electrode. By exchanging a small fraction of micrometer-sized activated carbon with sub-micrometer sized carbon black the electrical percolation can be re-established due to the formation of a well-distributed carbon cluster network. This leads to a more homogenous voltage or charge distribution and consequently circumvents the local degradation spots. The cycle life is increased from 10 (poor percolation) to 36,000 (good percolation) cycles, at equal carbon and LTO content of the electrodes.

By comparing the ratio of the cycle life at high rates to the cycle life at low rates, we can differentiate between cell degradation mainly caused by electrolyte decomposition (high values) from cell fading mainly caused by poor electrical percolation (low values). This reveals that the composite electrodes get more susceptible to high rate cycling with increasing LTO content due to the decreasing degree of electrical percolation. Contrary, if providing a perfect percolation, LTO based energy storage devices are only limited by electrolyte degradation, without any problems to withstand high rates. These results are of particular importance for the industrial manufacturing of LTO based electrodes, as this perfect percolation needs to be reliably ensured over huge electrode areas at relative low conductive carbon contents (inactive mass is usually kept as low as possible). Moreover, we are convinced that our results could also be of relevance for other electrochemical systems, which require electrodes containing high amounts of weakly conductive materials (e.g., LiFePO_4 cathodes or solid-state LIBs).

Acknowledgements

The authors thank A. Gonser and I. Wüthrl for the support and helpful discussions. We acknowledge funding from the German Federal Ministry for Economic Affairs and Energy (BMWi) in support of the HyBaCap project (award number 03ET6113C) and thank Prof. Eduard Arzt (INM) for his continuing support.

Appendix A. Supplementary data

Supplementary data associated with this article can be found, in the online version, at <http://dx.doi.org/10.1016/j.electacta.2017.07.073>.

References

- [1] Z. Yang, J. Zhang, M.C.W. Kintner-Meyer, X. Lu, D. Choi, J.P. Lemmon, J. Liu, *Chemical reviews* 111 (2011) 3577–3613.
- [2] F. Béguin, E. Frackowiak, *Supercapacitors: Materials, systems, and applications*, Wiley-VCH, Weinheim, 2013.
- [3] B. Scrosati, J. Garche, *Journal of Power Sources* 195 (2010) 2419–2430.
- [4] K. Xu, *Chemical reviews* 114 (2014) 11503–11618.
- [5] W.J.H. Borghols, M. Wagemaker, U. Lafont, E.M. Kelder, F.M. Mulder, *Journal of the American Chemical Society* 131 (2009) 17786–17792.
- [6] T. Ohzuku, *J. Electrochem. Soc.* 142 (1995) 1431.
- [7] K. Naoi, S. Ishimoto, Y. Isobe, S. Aoyagi, *Journal of Power Sources* 195 (2010) 6250–6254.
- [8] N. Takami, H. Inagaki, T. Kishi, Y. Harada, Y. Fujita, K. Hoshina, *J. Electrochem. Soc.* 156 (2009) A128.
- [9] C.-M. Chang, Y.-C. Chen, W.-L. Ma, P.-H. Wang, C.-F. Lee, H.-S. Chen, Y.W. Chen-Yang, *RSC Adv.* 5 (2015) 74381–74390.
- [10] L. Wen, Z. Wu, H. Luo, R. Song, F. Li, *Journal of the Electrochemical Society* 162 (2014) A3038–A3044.
- [11] A. Nugroho, D. Yoon, K.Y. Chung, J. Kim, *The Journal of Supercritical Fluids* 101 (2015) 72–80.
- [12] E. Zhao, C. Qin, H.-R. Jung, G. Berdichevsky, A. Nese, S. Marder, G. Yushin, *ACS nano* 10 (2016) 3977–3984.
- [13] X. Jia, Y. Kan, X. Zhu, G. Ning, Y. Lu, F. Wei, *Nano Energy* 10 (2014) 344–352.
- [14] X. Meng, J. Liu, X. Li, M.N. Banis, J. Yang, R. Li, X. Sun, *RSC Adv.* 3 (2013) 7285.
- [15] J. Shu, L. Hou, R. Ma, M. Shui, L. Shao, D. Wang, Y. Ren, W. Zheng, *RSC Adv.* 2 (2012) 10306.
- [16] J.-H. Choi, W.-H. Ryu, K. Park, J.-D. Jo, S.-M. Jo, D.-S. Lim, I.-D. Kim, *Scientific reports* 4 (2014) 7334.
- [17] H. Ni, L.-Z. Fan, *Journal of Power Sources* 214 (2012) 195–199.
- [18] K. Naoi, *Fuel Cells* 10 (2010) 825–833.
- [19] K. Naoi, S. Ishimoto, J.-i. Miyamoto, W. Naoi, *Energy Environ. Sci.* 5 (2012) 9363.
- [20] K. Naoi, W. Naoi, S. Aoyagi, J.-i. Miyamoto, T. Kamino, *Accounts of Chemical Research* 46 (2013) 1075–1083.
- [21] Y. Tang, Y. Zhang, X. Rui, D. Qi, Y. Luo, W.R. Leow, S. Chen, J. Guo, J. Wei, W. Li, J. Deng, Y. Lai, B. Ma, X. Chen, *Advanced materials (Deerfield Beach, Fla.)* 28 (2016) 1567–1576.
- [22] H.-p. Liu, G.-w. Wen, S.-f. Bi, C.-y. Wang, J.-m. Hao, P. Gao, *Electrochimica Acta* 192 (2016) 38–44.
- [23] H.-Y. Dong, Y.-B. He, B. Li, C. Zhang, M. Liu, F. Su, W. Lv, F. Kang, Q.-H. Yang, *Electrochimica Acta* 142 (2014) 247–253.
- [24] J. Zhu, R. Duan, Y. Zhang, J. Zhu, *Ceramics International* 42 (2016) 334–340.
- [25] N. Xu, X. Sun, X. Zhang, K. Wang, Y. Ma, *RSC Adv.* 5 (2015) 94361–94368.
- [26] Q. Wang, S.M. Zakeeruddin, I. Exnar, M. Grätzel, *J. Electrochem. Soc.* 151 (2004) A1598.
- [27] D. Di Censo, I. Exnar, M. Graetzel, *Electrochemistry Communications* 7 (2005) 1000–1006.
- [28] R. Kötz, M. Hahn, P. Ruch, R. Gallay, *Electrochemistry Communications* 10 (2008) 359–362.
- [29] T. Yuan, Z. Tan, C. Ma, J. Yang, Z.-F. Ma, S. Zheng, *Adv. Energy Mater.* 9–10 (2017) 1601625.
- [30] I. Belharouak, G.M. Koenig, T. Tan, H. Yumoto, N. Ota, K. Amine, *Journal of the Electrochemical Society* 159 (2012) A1165–A1170.
- [31] Y.-B. He, B. Li, M. Liu, C. Zhang, W. Lv, C. Yang, J. Li, H. Du, B. Zhang, Q.-H. Yang, J.-K. Kim, F. Kang, *Scientific reports* 2 (2012) 913.
- [32] M. He, E. Castel, A. Laumann, G. Nusp, P. Novak, E.J. Berg, *Journal of the Electrochemical Society* 162 (2015) A870–A876.
- [33] K. Wu, J. Yang, Y. Liu, Y. Zhang, C. Wang, J. Xu, F. Ning, D. Wang, *Journal of Power Sources* 237 (2013) 285–290.
- [34] B.-G. Lee, S.-H. Lee, *Journal of Power Sources* 343 (2017) 545–549.
- [35] N. Böckenfeld, R.-S. Kühnel, S. Passerini, M. Winter, A. Balducci, *Journal of Power Sources* 196 (2011) 4136–4142.
- [36] N. Böckenfeld, T. Placke, M. Winter, S. Passerini, A. Balducci, *Electrochimica Acta* 76 (2012) 130–136.
- [37] D. Cericola, P. Novák, A. Wokaun, R. Kötz, *Electrochimica Acta* 56 (2011) 8403–8411.
- [38] D. Cericola, P.W. Ruch, R. Kötz, P. Novák, A. Wokaun, *Electrochemistry Communications* 12 (2010) 812–815.
- [39] D. Cericola, P. Novák, A. Wokaun, R. Kötz, *Electrochimica Acta* 56 (2011) 1288–1293.
- [40] D. Cericola, P. Novák, A. Wokaun, R. Kötz, *Journal of Power Sources* 196 (2011) 10305–10313.
- [41] B. Wang, Q. Wang, B. Xu, T. Liu, D. Wang, G. Zhao, *RSC Adv.* 3 (2013) 20024.
- [42] M. Secchiaroli, R. Marassi, M. Wohlfahrt-Mehrens, S. Dsoke, *Electrochimica Acta* 219 (2016) 425–434.
- [43] K. Xu, *J. Electrochem. Soc.* 146 (1999) 4172.
- [44] K. Xu, M.S. Ding, T. Richard Jow, *Electrochimica Acta* 46 (2001) 1823–1827.
- [45] M. Widmaier, B. Krüner, N. Jäckel, M. Aslan, S. Fleischmann, C. Engel, V. Presser, *J. Electrochem. Soc.* 163 (2016) A2956–A2964.
- [46] D. Weingarth, M. Zeiger, N. Jäckel, M. Aslan, G. Feng, V. Presser, *Adv. Energy Mater.* 4 (2014) 1400316.
- [47] N. Jäckel, D. Weingarth, A. Schreiber, B. Krüner, M. Zeiger, A. Tolosa, M. Aslan, V. Presser, *Electrochimica Acta* 191 (2016) 284–298.
- [48] C.H. Chen, J.T. Vaughey, A.N. Jansen, D.W. Dees, A.J. Kahaian, T. Goacher, M.M. Thackeray, *J. Electrochem. Soc.* 148 (2001) A102.
- [49] N. Jäckel, D. Weingarth, M. Zeiger, M. Aslan, I. Grobelsek, V. Presser, *Journal of Power Sources* 272 (2014) 1122–1133.
- [50] D. Orbakh, *Nonaqueous electrochemistry*, Dekker, New York, 1999.
- [51] G.G. Amatucci, F. Badway, A. Du Pasquier, T. Zheng, *J. Electrochem. Soc.* 148 (2001) A930.
- [52] S. Stewart, P. Albertus, V. Srinivasan, I. Plitz, N. Pereira, G. Amatucci, J. Newman, *J. Electrochem. Soc.* 155 (2008) A253.
- [53] K. Zaghib, M. Dontigny, A. Guerfi, P. Charest, I. Rodrigues, A. Mauger, C.M. Julien, *Journal of Power Sources* 196 (2011) 3949–3954.
- [54] E. Frackowiak, F. Béguin, *Carbon* 39 (2001) 937–950.
- [55] M.W. Verbrugge, *J. Electrochem. Soc.* 146 (1999) 833.
- [56] P.R. Bandaru, H. Yamada, R. Narayanan, M. Hoefler, *Materials Science and Engineering: R: Reports* 96 (2015) 1–69.
- [57] J. Ma, C. Wang, S. Wroblewski, *Journal of Power Sources* 164 (2007) 849–856.
- [58] X. Lu, L. Zhao, X. He, R. Xiao, L. Gu, Y.-S. Hu, H. Li, Z. Wang, X. Duan, L. Chen, J. Maier, Y. Ikuhara, *Advanced materials (Deerfield Beach, Fla.)* 24 (2012) 3233–3238.
- [59] S. Scharner, *J. Electrochem. Soc.* 146 (1999) 857.
- [60] C. Delmas, M. Maccario, L. Croguennec, F. Le Cras, F. Weill, *Nature materials* 7 (2008) 665–671.
- [61] Y. Li, F. El Gabaly, T.R. Ferguson, R.B. Smith, N.C. Bartelt, J.D. Sugar, K.R. Fenton, D.A. Cogswell, A.L.D. Kilcoyne, T. Tyliczszak, M.Z. Bazant, W.C. Chueh, *Nature materials* 13 (2014) 1149–1156.
- [62] L.L. Zhang, X.S. Zhao, *Chemical Society reviews* 38 (2009) 2520–2531.
- [63] F. Wang, L. Wu, C. Ma, D. Su, Y. Zhu, J. Graetz, *Nanotechnology* 24 (2013) 424006.
- [64] H. Ge, N. Li, D. Li, C. Dai, D. Wang, *Electrochemistry Communications* 10 (2008) 719–722.
- [65] A.J. Bard, L.R. Faulkner, *Electrochemical methods: Fundamentals and applications*, in: Allen J. Bard, Larry R. Faulkner (Eds.), 2nd ed., John Wiley, New York, Chichester, 2001.
- [66] D. Weingarth, H. Noh, A. Foelske-Schmitz, A. Wokaun, R. Kötz, *Electrochimica Acta* 103 (2013) 119–124.
- [67] M. Aslan, D. Weingarth, N. Jäckel, J.S. Atchison, I. Grobelsek, V. Presser, *Journal of Power Sources* 266 (2014) 374–383.
- [68] S. Dsoke, B. Fuchs, E. Gucciard, M. Wohlfahrt-Mehrens, *Journal of Power Sources* 282 (2015) 385–393.
- [69] S.J. An, J. Li, C. Daniel, D. Mohanty, S. Nagpure, D.L. Wood, *Carbon* 105 (2016) 52–76.
- [70] P.W. Ruch, D. Cericola, A. Foelske, R. Kötz, A. Wokaun, *Electrochimica Acta* 55 (2010) 2352–2357.
- [71] R. Fong, *J. Electrochem. Soc.* 137 (1990) 2009.
- [72] D. Weingarth, A. Foelske-Schmitz, R. Kötz, *Journal of Power Sources* 225 (2013) 84–88.

Influence of carbon distribution on the electrochemical performance and stability of lithium titanate based energy storage devices

Mathias Widmaier^{1,2}, Nicolas Jäckel^{2,3}, Marco Zeiger^{2,3}, Murad Abuzarli⁴, Christine Engel¹,
Lars Bommer¹, and Volker Presser^{2,3,*}

¹ Robert Bosch GmbH, Postfach 10 60 50, 70049 Stuttgart, Germany

² Department of Materials Science and Engineering, Saarland University, Campus D2 2, 66123 Saarbrücken, Germany

³ INM – Leibniz Institute for New Materials, Campus D2 2, 66123 Saarbrücken, Germany

⁴ ESPCI Paris, PSL Research University, 10 rue Vauquelin, 75231 Paris Cedex 05, France

* corresponding author's email: volker.presser@leibniz-inm.de

Supporting Information

Figures

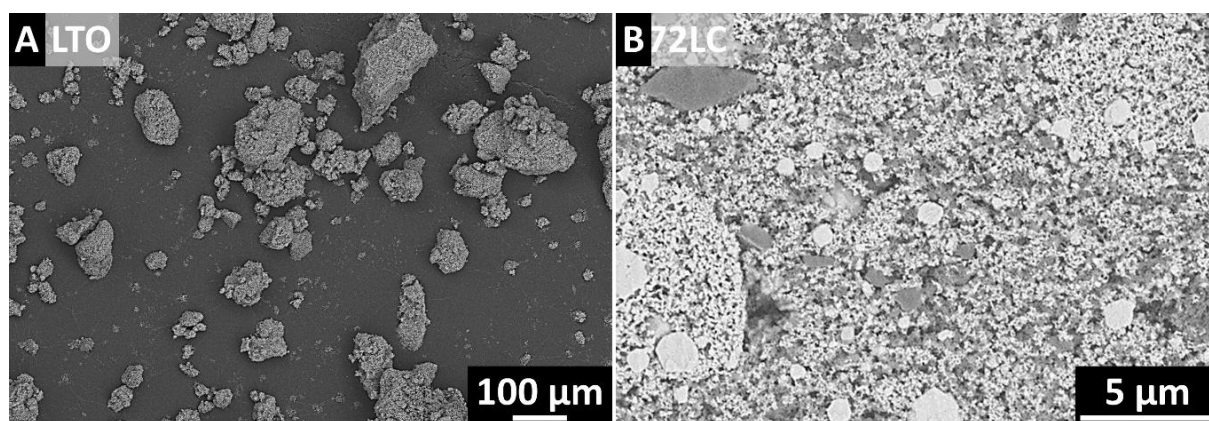


Fig. S1: SEM micrographs of LTO (A) and a higher magnification of 72LC based electrodes.

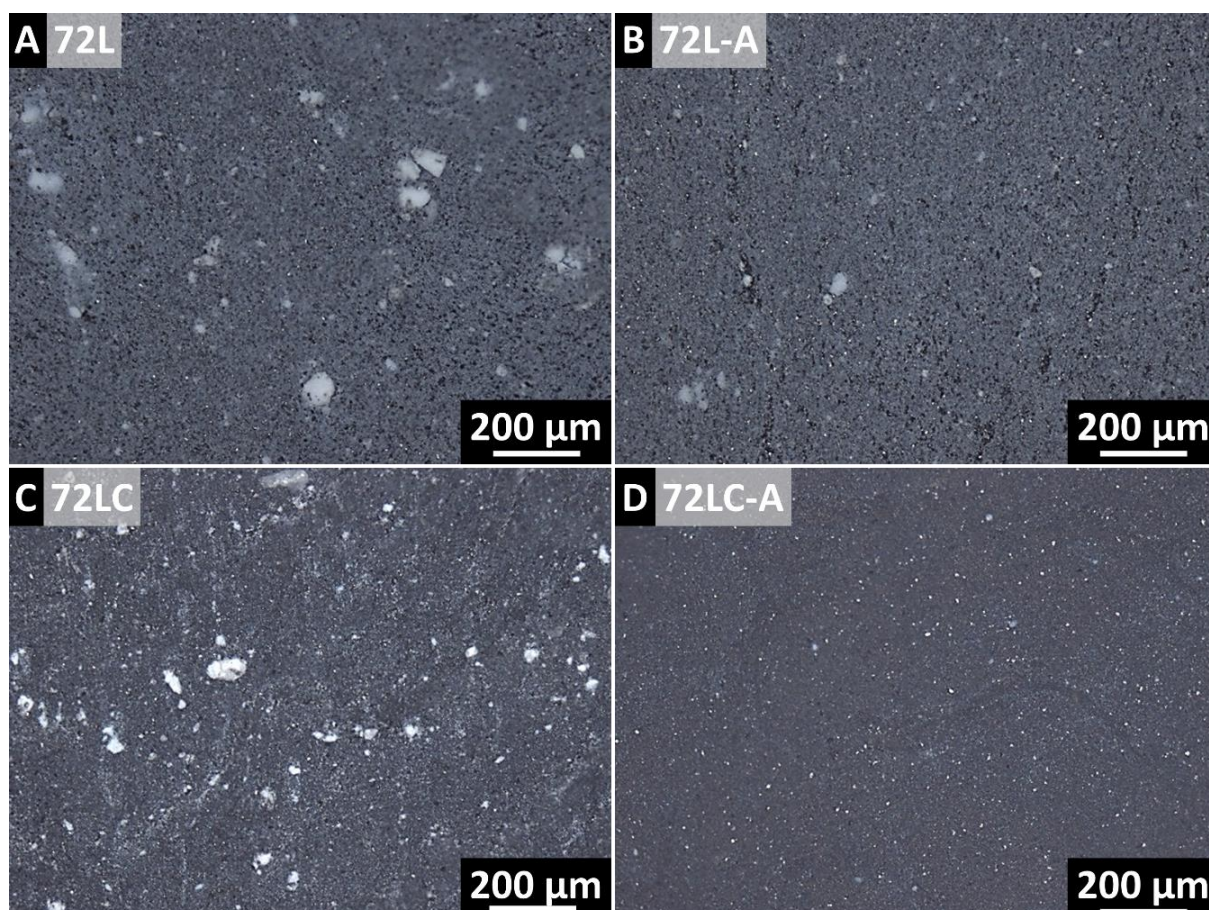


Fig. S2: Light micrograph of (A) 72L, (B) 72L-A, (C) 72LC, and (D) 72LC-A. The white phase relates to LTO agglomerates.

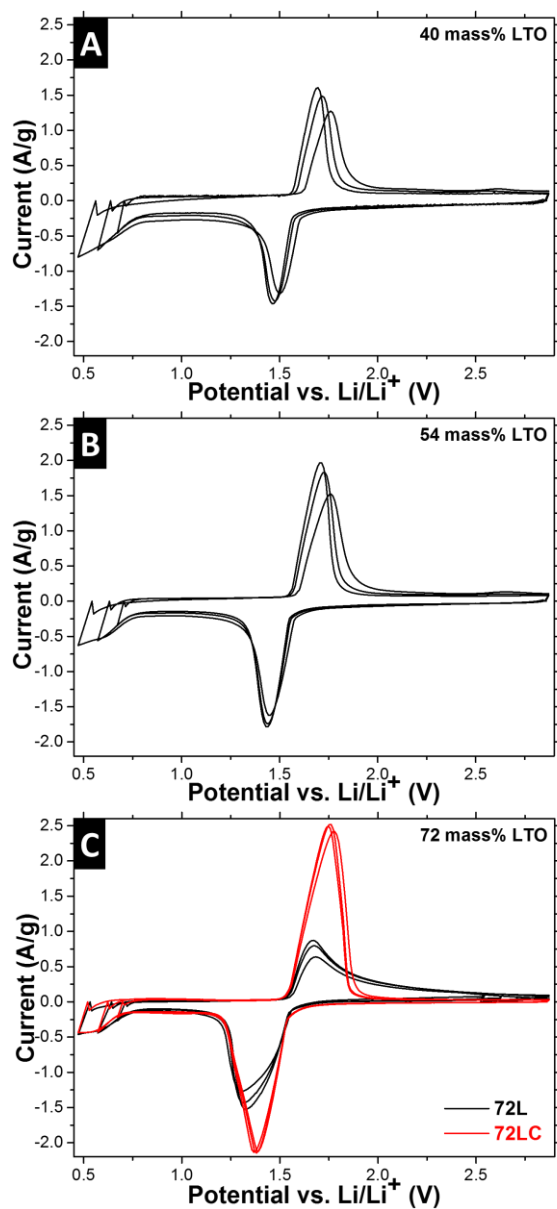


Fig. S3: Cyclic voltammetric potential window opening of (A) 0L, (B) 54L, (C) 72L and 72LC up to a maximum polarization of 0.472 V vs. Li/Li⁺.

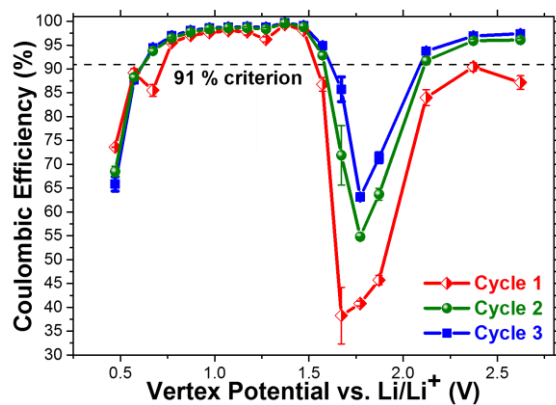


Fig. S4: CE course plot of 72L determined from cyclic voltammetric potential window opening experiments in dependence of evaluated cycle.

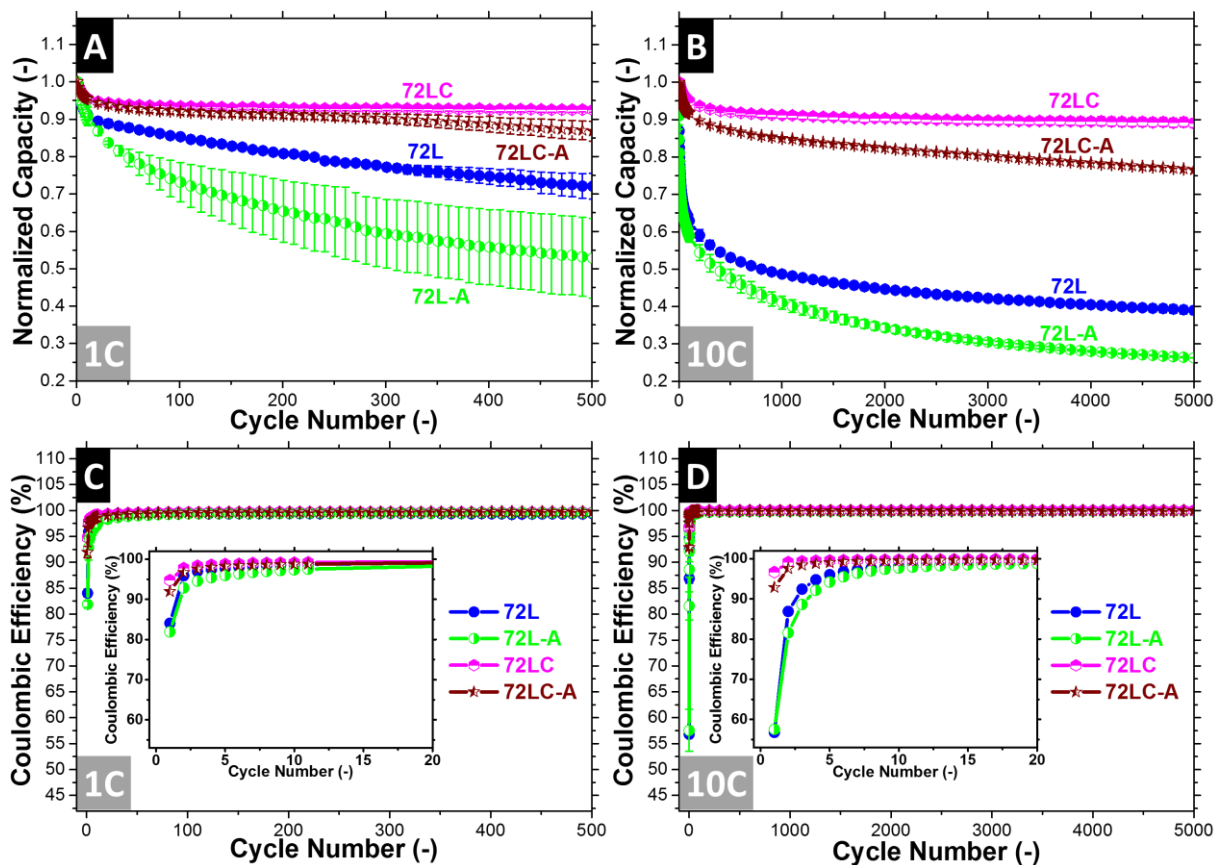


Fig. S5: Electrochemical cycling stability measured at charging/discharging rates of 1 C (A) and 10 C (B) of electrodes containing LTO agglomerates (72L, 72LC) and electrodes with a decreased amount of LTO agglomerates (72L-A, 72LC-A). Calculated coulombic efficiency at 1 C (C) and 10 C (D).

Tables

Table S1: Overview of the dosages used for electrode manufacturing. The PTFE values stated are given with respect to a 60 % water suspension.

	LTO (g)	AC (g)	CB (g)	PTFE (g)	Isopropanol (g)
0L	-	1.876	-	0.347	3.5
0LC	-	1.688	0.188	0.347	3.9
40L	1.0	1.273	-	0.421	2.2
54L	1.0	0.667	-	0.309	2.4
72L	1.5	0.375	-	0.347	2.6
72L-A	1.5	0.375	-	0.347	2.7
72LC	1.5	0.188	0.188	0.347	3.9
72LC-A	1.5	0.188	0.188	0.347	2.7

3.3 Valence-Tuned Lithium Titanate Nanopowder for High-Rate Electrochemical Energy Storage

M. Widmaier^{1,2}, K. Pfeifer^{1,3}, L. Bommer¹, and V. Presser^{2,4}

¹ Robert Bosch GmbH, Robert-Bosch-Campus 1, 71272 Renningen, Germany

² Saarland University, Campus D2 2, 66123 Saarbrücken, Germany

³ Chemisches Institut, Eberhard Karls Universität Tübingen, Auf der Morgenstelle 18, 72076 Tübingen, Germany

⁴ INM – Leibniz Institute for New Materials, Campus D2 2, 66123 Saarbrücken, Germany

Citation:

Batteries & Supercaps, 2018, DOI:10.1002/batt.201700007

Own Contribution:

Planning, writing, electrochemical measurements

Abstract:

In recent years, numerous studies have explored ways to overcome the low intrinsic electrical conductivity of lithium titanate ($\text{Li}_4\text{Ti}_5\text{O}_{12}$, LTO) for energy storage with lithium-ion batteries. These approaches almost exclusively considered element doping and elaborate LTO-carbon nanocomposites, whereas simple adjustment of the defect concentration remains largely unexplored. In our study, we will tune the $\text{Ti}^{3+}/\text{Ti}^{4+}$ concentration of a commercial LTO nanopowder through oxygen vacancy formation during thermal annealing in a hydrogen atmosphere. We investigated the impact of the treatment on material properties like energy band structure, electrical conductivity, crystallinity, phase distribution, surface chemistry, and particle morphology and correlated these parameters to the electrochemical performance. At optimum treatment conditions, the intrinsic electrical conductivity can be greatly improved, while circumventing LTO phase transformations or amorphization. This enables the reduction of the carbon concentration to 5 mass% while yielding a high electrode capacity of about 70 mAh/g (82 mAh/g based on active mass) at ultra-high C-rates of 100 C. When combined with an activated carbon / lithium manganese oxide composite cathode, an excellent energy and power performance of 70 Wh/kg and 47 kW/kg were obtained (82 Wh/kg and 55 kW/kg based on active mass), while maintaining 83 % of its energy ratings after 5,000 cycles at 10 C (78 % after 15,000 cycles at 100 C).

Valence-Tuned Lithium Titanate Nanopowder for High-Rate Electrochemical Energy Storage

Mathias Widmaier,^[a, b] Kristina Pfeifer,^[a, c] Lars Bommer,^[a] and Volker Presser^{*[b, d]}

In recent years, numerous studies have explored ways to overcome the low intrinsic electrical conductivity of lithium titanate ($\text{Li}_4\text{Ti}_5\text{O}_{12}$, LTO) for energy storage with lithium-ion batteries. These approaches almost exclusively considered element doping and elaborate LTO-carbon nanocomposites, whereas simple adjustment of the defect concentration remains largely unexplored. In our study, we tune the $\text{Ti}^{3+}/\text{Ti}^{4+}$ concentration of a commercial LTO nanopowder through oxygen vacancy formation during thermal annealing in hydrogen atmosphere. We investigate the impact of the treatment on material properties like energy band structure, electrical conductivity, crystallinity, phase distribution, surface chemistry, and particle morphology, and correlate these parameters to the

electrochemical performance. At optimum treatment conditions, the intrinsic electrical conductivity can be greatly improved, while circumventing LTO phase transformations or amorphization. This enables the reduction of the carbon concentration to 5 mass%, while yielding a high electrode capacity of about 70 mAh/g (82 mAh/g based on active mass) at ultrahigh C-rates of 100C. When combined with an activated carbon/lithium manganese oxide composite cathode, an excellent energy and power performance of 70 Wh/kg and 47 kW/kg were obtained (82 Wh/kg and 55 kW/kg based on active mass), while maintaining 83% of its energy ratings after 5000 cycles at 10C (78% after 15000 cycles at 100C).

1. Introduction

Lithium-ion batteries and supercapacitors have become indispensable energy storage devices for the steadily growing electrification.^[1] Lithium-ion batteries store energy via reversible Faradaic reactions and related lithium intercalation/de-intercalation into host materials.^[2] On the contrary, the operating principle of a conventional supercapacitor is based on ion electrosorption at the interface of an electrolyte and high surface area electrodes, such as activated carbon (AC).^[3] These energy storage principles are reflected by the inherently different properties of both devices: A lithium-ion battery is a high energy device with moderate power and longevity, while a supercapacitor possesses a superior power density and cycle life with an inferior energy density.^[4] To overcome the intrinsic limitations of each of these two technologies, device hybridization has been explored in recent years.^[5–14]

Hybrid supercapacitors, combining the advantages of both devices, were first introduced in a pioneering study of Amatucci et al.^[5] In this work, an asymmetric hybrid supercapacitor combined an AC cathode with a lithium titanate anode.

Hybridization can also be realized by combining lithium-ion battery materials with AC in the same electrode. These composite electrodes have attracted considerable interest in the scientific community and several material combinations have been proposed.^[6–14] Additionally beneficial synergistic effects between both material classes have been observed, as AC simultaneously decreases the electrode resistivity and can act as a “shock absorber” for high currents.^[7,12]

LTO is a promising lithium-ion battery electrode material for high rate applications due to its inherent safety, high Coulombic efficiency, negligible volume expansion during lithiation, cost effective raw materials for synthesis, and effective avoidance of the solid electrolyte interphase (SEI) formation.^[15–17] The electrochemical behavior of LTO-based electrodes may severely deteriorate because of LTO's poor intrinsic electronic conductivity of about 10^{-13} S/cm.^[14,18] However, there is an abrupt rise of electrical conductivity for lithiated LTO ($\text{Li}_7\text{Ti}_5\text{O}_{12}$) to about 10^{-2} S/cm.^[19] At present, state-of-the-art literature appears to have split into two camps:

- The electrical conductivity of the lithiated phase ($\text{Li}_7\text{Ti}_5\text{O}_{12}$) is sufficiently high to operate LTO without any or very low amounts of conductive additives (< 5 mass%).^[20–25] Kinetic limitations of LTO are mainly caused by sluggish lithium diffusion and an improvement of electrical conductivity is not required.^[25,26]
- The low electrical conductivity of $\text{Li}_4\text{Ti}_5\text{O}_{12}$ deteriorates the electrochemical performance and large amounts of carbon are required for high rate operation. In this context, a variety of LTO-carbon nanocomposites have been proposed; for example, LTO confined in nanopores of AC,^[27] and LTO grafted on carbon nanotubes,^[28–32] carbon nanofibers,^[17,33–35] or graphene.^[36–40] The carbon content of the electrode is often neglected when calculating the capacity (i.e., capacity

[a] M. Widmaier, K. Pfeifer, Dr. L. Bommer
Robert Bosch GmbH, Robert-Bosch-Campus 1, 71272 Renningen, Germany

[b] M. Widmaier, Prof. V. Presser
Department of Materials Science and Engineering, Saarland University,
Campus D2 2, 66123 Saarbrücken, Germany
E-mail: volker.presser@leibniz-inm.de

[c] K. Pfeifer
Chemisches Institut, Eberhard Karls Universität Tübingen, Auf der Morgen-
stelle 18, 72076 Tübingen, Germany

[d] Prof. V. Presser
INM – Leibniz Institute for New Materials, Campus D2 2, 66123 Saarbrücken,
Germany

Supporting information for this article is available on the WWW under
<https://doi.org/10.1002/batt.201700007>

is only normalized to the LTO mass of the electrode). Yet, such a normalization is questionable as the electrode may contain up to 20–50 mass% carbon and only the performance of the entire electrode is of importance for an actual device (not how well a small quantity of LTO performs in a massive matrix of electrochemically inactive carbon).

The electrical conductivity of carbon and its distribution can also severely influence the electrochemical stability of a composite electrode as we have demonstrated recently.^[14] LTO doping (e.g., with Cu^{2+} ,^[41] Mg^{2+} ,^[42] Zn^{2+} ,^[43] Fe^{3+} ,^[44] Cr^{3+} ,^[45] Al^{3+} ,^[46] Sn^{4+} ,^[47] Zr^{4+} ,^[48] Ta^{5+} ,^[49] V^{5+} ,^[50] Nb^{5+} ,^[51] W^{6+} ,^[52]) is another effective way to improve the intrinsic electronic conductivity of LTO. Such doping elements have been reported to reduce a fraction of Ti^{4+} into Ti^{3+} and hence increase the overall electron concentration.^[53] Nevertheless, element doping might entail additional problems related to the toxicity of certain doping elements and possible detrimental side reactions.^[54]

In 2006, Wolfenstine et al.^[55] discovered that Ti^{3+} valence states may form during prolonged annealing (36 h) of LTO at 800 °C in hydrogen containing atmosphere, although the root cause of this effect remained unknown. This simple strategy is free of waste products and does not require the addition of any other additional chemicals or catalysts,^[56] but has only attracted little attention in literature so far (especially in contrast to the large number of studies addressing carbon-LTO nanocomposites or LTO doping). Shen et al.^[57] proposed annealing of LTO nanowire arrays under hydrogen atmosphere to create Ti^{3+} valence states. A minor shift of the Ti 2p X-ray photoelectron spectra to lower binding energies after hydrogen treatment confirmed the formation of Ti^{3+} valences. This change was attributed to the formation of OH surface defects after hydrogen treatment. Hydrogen treatment was conducted in 5 vol% H_2 in Ar at 500–700 °C for 1.5 h, while the pressure or the impact of the treatment temperature was not specified. Later work of Qiu et al.^[56] was conducted with industrial grade LTO in high purity H_2 gas sourced from a metal-hydride at a high pressure of 40 bar for 1 h. It was suggested that the elevated temperature “facilitates the opening of the LTO lattice” while the high pressure “helps the deep penetration of hydrogen into the LTO bulk”.^[56] In this work, it was also proposed that, besides OH groups, additionally oxygen vacancies are responsible for the Ti^{3+} valence states and the improvement of the rate performance. The enhanced electrochemical kinetics were attributed to increased electronic conductivity caused by Ti^{3+} valence states and a simultaneously improved Li-ion diffusivity due to larger diffusion pathways in the oxygen-deficient LTO. Sen et al. conducted hydrogen annealing of LTO nanosheets at 500 °C for 2 h with a heating rate 3 °Cmin⁻¹ (pressure not stated) and concluded that “the introduction of Ti^{3+} species and/or oxygen vacancies greatly improves the electronic conductivity”.^[58] Accordingly, current literature on this topic seems to be inconsistent even on basic aspects like necessity of pressure, temperature range of the reaction, and the underpinning processes causing Ti^{3+} valence states.

In the current study, we address these issues and provide comprehensive data to identify crucial temperature ranges of the reaction. The associated implications on material and

chemical properties (e.g., crystallinity, surface area, particle size, phase contents, titanium valence state) will be investigated and connected to the electrochemical behavior of LTO half cells and LTO-based hybrid supercapacitors. For this purpose, a commercially available lithium titanate nanopowder was heated to defined temperatures in hydrogen atmosphere, followed by an immediate cooling to preserve prevailing material properties. This allows us to adjust the concentration of Ti^{3+} valences and to identify the rate limiting factor of a nanoparticulate LTO electrode.

Experimental Section

Electrode Materials and Electrode Preparation

Steam-activated, coconut-derived activated carbon (AC) powders YP-50F and YP-80F were purchased from Kuraray Chemicals. Carbon black (CB) type C-ENERGY C65, referred to as CB, was obtained from Imerys Graphite & Carbon. Commercial lithium manganese oxide (LMO, type: HPM-7051) and nanometer-sized lithium titanate (LTO, type: lithium titanate, spinel, nanopowder) was obtained from Toda Kogyo and Sigma Aldrich, respectively.

LTO was modified in a high temperature furnace (FSW 230/400-1500-MO/BL/PS, FCT Anlagenbau GmbH) by heating under hydrogen at atmospheric pressure with 10 °Cmin⁻¹ from room temperature to 500 °C, 600 °C, 800 °C, 900 °C, or 1000 °C and a hydrogen flow rate of 2 Lmin⁻¹. The samples were labelled L (pristine powder), L/500, L/800, L/900, and L/1000, respectively. Afterwards, the gas flow was switched to Ar with a flow rate of 2 L/min and the samples were cooled to room temperature at a rate of 20 °C/min without any temperature holding steps to preserve the prevailing material properties. After heat-treatment, the samples were immediately transferred into an Ar-filled glovebox (MBraun, O_2 and $\text{H}_2\text{O} < 1$ ppm) until further use to avoid a re-oxidation of the material.

For negative electrodes, LTO powder was mixed with different ratios of CB (Table 1) and 10 mass% polyvinylidene fluoride (PVdF) dissolved in dimethyl sulfoxide in a DAC400 FVZ speed-mixer. Subsequently, the electrode slurries were doctor bladed on a carbon-coated aluminum foil current collector (Ranafoil from Toyo Aluminium). The electrode sheets were dried for two days at ambient conditions in a fume hood, followed by drying in vacuum at 120 °C for 12 h. Finally, the dried electrodes were transferred and stored in an Ar-filled glovebox (MBraun, O_2 and $\text{H}_2\text{O} < 1$ ppm). Dried negative electrodes typically possessed a thickness of 25 ± 5 μm with a material loading of 3 ± 1 mg/cm². The different negative electrode compositions are distinguished by a number, which reflects the CB content in mass percent, followed by the

Table 1. Overview of the employed anode recipes and labeling.

Sample	LTO material	LTO content [mass%]	CB content [mass%]	PVdF content [mass%]
0-L	Pristine	90	0	10
5-L	Pristine	85	5	10
20-L	Pristine	70	20	10
5-L/500	500 °C in H_2	85	5	10
5-L/600	600 °C in H_2	85	5	10
5-L/800	800 °C in H_2	85	5	10
5-L/900	900 °C in H_2	85	5	10
5-L/1000	1000 °C in H_2	85	5	10

addition “-L” (pristine powder) or “-L/X” where “X” is the treatment temperature in °C of the respective modified LTO powder (Table 1).

Positive electrodes were produced by mixing 4.4 g activated carbon (YP-80F) with 2.4 g lithium manganese oxide, 0.4 g CB, and 0.8 g PVdF in dimethyl sulfoxide utilizing the same electrode preparation process as for negative electrodes. The dry electrode thickness was adjusted to $128 \pm 10 \mu\text{m}$ at a material loading of $7 \pm 1 \text{ mg/cm}^2$.

The counter electrode was prepared by mixing YP-50F with isopropanol in a DAC400 FVZ speed mixer at 2500 rpm.^[59] This treatment was followed by 7 min sonication and subsequent 4 min mixing at 2500 rpm. Afterwards, the slurry was transformed to a paste by adding 10 mass% (dry mass) of dissolved polytetrafluoroethylene (PTFE, 60 mass% solution in water from Sigma Aldrich) combined with speed-mixing at 800 rpm for 5 min. This paste was manually kneaded on a glass plate until the consistency of the paste was sufficiently viscous for further processing. An appropriate amount of electrode paste was placed between two untreated aluminum foils. This stack was then calendared in a BLE682 battery lamination machine by applying a mass of 70 kg and a forward speed of 10 mm/s.

We used a dry electrode preparation process inside an argon-filled glovebox (MBraun, O_2 and $\text{H}_2\text{O} < 1 \text{ ppm}$) to manufacture quasi-reference electrodes (QRE) based on surface-functionalized AC, as outlined in more detail in Ref. [59]. Functionalization of AC was conducted in a nitric acid solution at 95 °C for 5 h according to our procedure described in Ref. [59]. The functionalization of AC introduces nitrogen and oxygen containing functional groups on the carbon surface, which drastically stabilize the QRE stability.^[59] The functionalized AC and PTFE powders (PTFE 6 CN X, DuPont) were dried at 120 °C under vacuum for 12 h before being introduced to the glovebox. Afterwards, 0.45 g carbon powder was mixed with 0.05 g PTFE and grinded in a mortar until a dry paste had formed. Small parts of the latter were then cut and used as QRE. For convenience and comparability to literature, all QRE potentials stated in this work were calculated to the Li potential.^[59]

Cell Preparation and Electrochemical Measurements

For electrochemical testing, we employed a custom-built polyether ether ketone (PEEK) cell with spring-loaded titanium pistons as a three-electrode system, as described in Ref. [60]. Electrode discs with 12 mm diameter were punched out of the electrode films and separated by a glass-fiber (Whatman GF/D) or cellulose separator (Nippon Kodoshi) for half-cell cycle life, or half-cell rate capability measurements and full-cells, respectively. The mass ratio of anode/cathode of full-cells was adjusted to 0.37. For half-cell cycle life measurements, two counter electrodes ($525 \pm 20 \mu\text{m}$ each) were pressed together and placed on a carbon-coated aluminum foil current collector (Ranafoil, Toyo Aluminium). In case of half-cell rate capability measurements, one counter electrode was used instead. The assembled cells were dried at 120 °C for 12 h at 0.1 Pa and then transferred to an Ar-filled glovebox (MBraun, O_2 and $\text{H}_2\text{O} < 1 \text{ ppm}$). After cooling, the QRE was placed on a compressed glass-fiber separator (GF/D, from Whatman) in a cavity close to the working electrode/counter electrode stack and contacted by a titanium wire. Afterwards the cells were vacuum-filled with 1 M LiClO_4 dissolved in acetonitrile (99.9%, water content $< 10 \text{ ppm}$, Acros Organics). In addition, individual electrodes were arranged between titanium positions without the addition of electrolyte, and a current of 0.001 mA was applied to probe the electrical percolation.

Electrochemical measurements were carried out using a potentiostat/galvanostat CTS LAB from BaSyTec. Cyclic voltammetry was

recorded with a sweep rate of 0.1 mV/s from 1.17–2.37 V. Galvanostatic charge/discharge cycling with potential limitation (GCPL) experiments were conducted at 1.17–2.37 V vs. Li/Li^+ for half-cells and at 0.8–2.8 V for full-cells. The C-rate was calculated from the theoretical capacity of LTO (175 mAh/g, Ref.[16]). Half-cell rate capability measurements were conducted at C-rates between 0.1C and 200C (same rates for charge and discharge). Full-cells were cycled at 10C for 100 charge-discharge cycles and then charged at 1C prior to discharging at C-rates between 1C and 1000C. All electrochemical stability measurements were conducted at 10C charge/discharge rates. The first 100 cycles were recorded in sequence, followed by recording every 100th cycle until reaching 5000 cycles. All capacity, energy density, and power density values stated in this work are given with respect to the entire electrode mass if not otherwise mentioned and all electrochemical measurements were conducted at $23 \pm 1 \text{ }^\circ\text{C}$.

Material Characterization

Thermogravimetric measurements combined with a mass spectrometer (TGA-MS) were performed using a STA 409CD – QMS422 from Netzsch under Ar. For measurements using 60% H_2 and 40% He, a STA 429CD from Netzsch coupled with an analytical mass spectrometer QMG 422 from Balzers was used instead. The samples were heated to 1000 °C at a rate of 10 °C/min in the respective atmospheres.

Scanning electron microscopy (SEM) analysis was carried out with a SUPRA VP system from Zeiss at an acceleration voltage of 5 kV. The samples were mounted on a carbon tab and sputter coated with a thin layer of platinum/palladium prior to the investigation.

Transmission electron microscopy (TEM) was performed with a JEOL 2100F system operating at 120 kV. Samples were prepared by dispersing and sonicating of the powder samples in isopropanol and deposition on a copper grid with a lacey carbon film (Gatan).

Nitrogen gas sorption measurements of the carbon powders were carried out with an Autosorb iQ system (Quantachrome), at the temperature of liquid nitrogen ($-196 \text{ }^\circ\text{C}$) after outgassing (at 300 °C for 24 h) at about 10^2 Pa . The relative pressure range was varied from $5 \cdot 10^{-7}$ to 1.0 in 68 steps. The specific surface area (SSA) was calculated with the ASiQwin-software using the Brunauer-Emmett-Teller (BET) equation^[61] in the linear pressure range from 0.01–0.2. Values for the total pore volume correspond to $p/p_0 = 0.95$.^[62]

UV-Vis-NIR diffuse reflectance measurements were recorded at 250–2500 nm employing a Cary 5000 UV-Vis-NIR spectrometer (Agilent) with an integrating sphere (Labsphere). Powder samples with a thickness of about 500 μm were sandwiched between quartz glass. The reflectance of the quartz glass was subtracted from all measured spectra.

X-ray diffraction (XRD) experiments were conducted using a D8Advance DaVinci-Cu diffractometer (Bruker AXS) with a $\text{CuK}\alpha$ X-ray source, a Bragg-Brentano geometry, a 0.5° aperture stop, and a LynxEye detector. Rietveld refinement was carried out using TOPAS software (Bruker AXS).

X-ray photoelectron spectroscopy (XPS) was carried out with a PHI Quantera SXM utilizing monochromatic $\text{AlK}\alpha$ emission with an energy of 1486.6 eV for excitation (50 W, 200 μm spot diameter) and an angle between sample and analyzer of 45° . Survey spectra were recorded with a step size of 0.8 eV and a pass energy of 224 eV. For high resolution C 1 s and O 1 s spectra, a step size of 0.05 eV and a pass energy of 55 eV were used instead. The C 1 s maximum which was shifted to 285 eV to calibrate the binding energies of all recorded spectra. Before the measurements, the

powder samples were pressed with a steel roller onto indium foils. Immediately afterwards, the samples were introduced into an ultrahigh vacuum.

2. Results and Discussion

2.1. Thermal Annealing of LTO in Hydrogen Atmosphere

A reduction of the LTO titanium oxidation state in hydrogen atmosphere can be explained by the reaction of hydrogen with lattice oxygen to form oxygen vacancies and water (Eq. 1) or by the creation of proton defects (Eq. 2). These two reactions can be expressed by use of the Kröger-Vink notation as follows:



Both reactions will lead to mass changes of LTO during annealing under hydrogen: Eq. 1 causes a mass decrease and Eq. 2 a slight mass increase. We measured TG-MS in hydrogen and argon atmosphere (Figure 1) to gain more insights into mechanisms and relevant temperature ranges of the reaction. Below 450 °C, we observed three distinct regions of mass loss when thermally annealing in argon and in hydrogen atmosphere. These mass changes must be connected to intrinsic reactions of LTO during thermal annealing, rather than arising from specific reactions of LTO with hydrogen. In the first and second region, water desorbs from the sample (Figure 1B) with maximum rates of mass change centered at 86 °C and 223 °C, respectively. The low temperature desorption is correlated to the release of physisorbed water from the surface, while water desorption at 223 °C is likely connected to the recombination of OH groups. This temperature aligns with values reported for recombination in TiO₂ for OH by Henderson (217 °C; Ref. [63]) and Hugenschmidt et al. (227 °C; Ref. [64]). At about 400 °C, a third reaction takes place which releases CO₂. Additionally, small amounts of CO₂ desorb in the temperature range of 150–

350 °C. The CO₂ desorption could be related to decomposition of carboxylic groups at the LTO surface and/or of impurities.

At temperatures exceeding 450 °C, the behavior of LTO annealed in either argon or hydrogen starts to deviate. In argon atmosphere, no further decomposition reaction is detected, as the mass remains constant (Figure 1A) and no gaseous species were observed. By contrast, after annealing in hydrogen, we see a continued mass loss and a simultaneous water desorption at 450–1000 °C. Hence, we can correlate this temperature range to the reaction according to Eq. 1. A shoulder of the differential thermogravimetry (DTG) curve at 813 °C and an additional small peak at 940 °C indicate a possible transition of the type of reaction mechanism in the range of 800–900 °C. Oxygen may initially be removed from low energy lattice sites until reaching the maximum reaction rate at about 813 °C. With increasing the reaction temperature, these oxygen positions continuously deplete and are replaced by oxygen vacancies. Thereby, the reaction rate is being reduced and a shoulder of the DTG curve is observed. For temperatures above 800 °C, the thermal energy is sufficient to also activate the removal of oxygen located at high-energy positions and the reaction rate re-accelerates until reaching its maximum at 940 °C.

Based on these observations, we annealed LTO at 500 °C (reaction start), 600 °C (early stage of reaction), 800 °C (DTG shoulder), 900 °C (transition area to second high-temperature DTG peak), and 1000 °C (post second high-temperature DTG peak) in a furnace under hydrogen atmosphere to produce appropriate quantities of modified LTO for further experiments. For all annealing experiments, we chose conditions alike applied during the TG measurements for a meaningful comparability (i.e., same heating rate, no temperature holding steps, gas flow switched to Ar during cooling to preserve the prevailing material properties). The samples treated in the furnace show a mass loss as would be expected from the TG measurement (Figure 1A). A slightly higher mass than what we measured with the thermogram for high-temperature treated samples (L/800, L/900, and L/1000) could be indicative to absorption of gaseous species and a minor re-oxidation during follow-up sample transfer (in air).

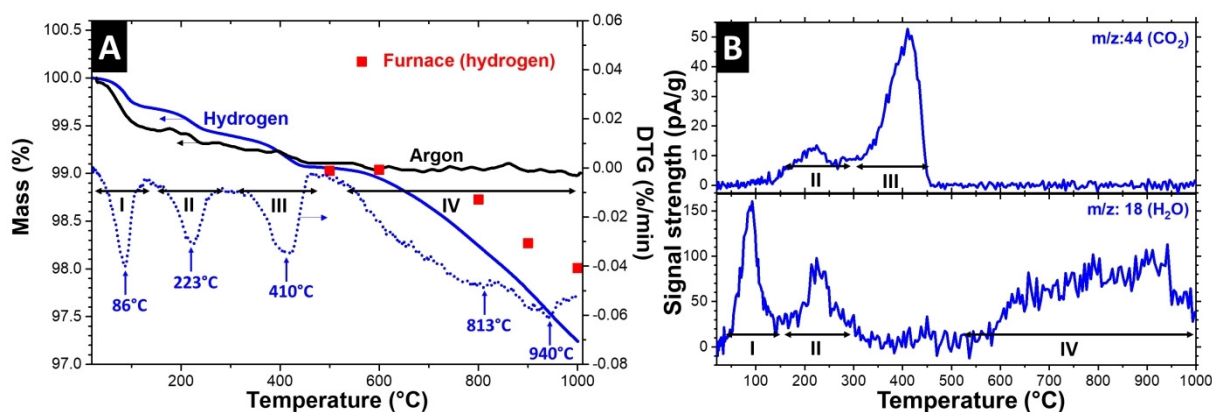


Figure 1. (A) Thermogravimetric and derivative thermogravimetric (DTG) curve of LTO powder during thermal annealing under argon and hydrogen atmosphere. The red markers correspond to mass loss measured after treatment of LTO in a high temperature furnace under hydrogen atmosphere. (B) Mass spectra signals of the gasses evolving during annealing under hydrogen atmosphere.

Our results confirm a mechanism according to Eq. 1. Nevertheless, proton defects cannot be entirely excluded according to the TG-MS results, as hydrogen absorption according to Eq. 2 could be masked by the observed oxygen removal, especially when considering the large mass difference between hydrogen and oxygen. The presence of large amounts of OH groups is relatively unlikely due to the tendency of OH groups to condensate into water and oxygen vacancies during thermal annealing.^[63] Shin et al.^[54] concluded that oxygen vacancies account for the majority of crystal structure defects for hydrogen treated TiO₂, as proton defects would equilibrate quickly due to the much higher mobility as compared to oxygen vacancies.^[54] Hence, proton defects likely play a minor role for hydrogen treated LTO. The strong hydrogen signal reported by Qiu et al.^[56] using nuclear magnetic resonance (NMR) spectroscopy could be caused by chemisorbed water due to the high tendency for water absorption of the oxygen-deficient samples caused by the reasons described above, rather than originating from OH-groups formed during hydrogen treatment. Moreover, oxygen-deficient LTO (Ref. [65]) and TiO₂ (Ref. [66]) surfaces have been reported to immediately form OH groups after exposure to atmospheric water due to the high hydrophilicity of Ti³⁺,^[67] this trend is also supported by our XPS characterization below.

We have calculated the chemical composition and oxidation state of Ti according to the mass loss of the thermogram recorded at 450–1000 °C for LTO annealed in hydrogen (Table 2) by assuming Eq. 1 and LTO phase preservation. A mass loss of 1% at a moderate temperature of 800 °C appears relatively small. Yet, this value translates to about 0.25 oxygen ions removed per LTO structural unit, as phase preservation can be assumed at this temperature (see XRD characterization). Therefore, every eighth titanium ion was reduced from Ti⁴⁺ to Ti³⁺ at 800 °C. Accordingly, significant modifications of electronic properties of the electrode material are anticipated. Furthermore, enough Ti⁴⁺ remains for the electrochemical reaction: three out of five Ti⁴⁺ ions have to be reduced to Ti³⁺ during lithiation to attain the full theoretical capacity of 175 mAh/g.^[16]

2.2. Material Characterization of Reduced LTO Powders

The LTO investigated in this study predominantly consists of branched chains of fused LTO nanoparticles with about 50 nm

diameter, as can be seen from electron micrographs depicted in Figure 2A. This microstructure benefits rapid electrolyte penetration through the open pore network and simultaneously increases the overall electrolyte-electrode interface area. Accordingly, the Li-diffusion distance in the solid state is decreased and fast charge and discharge rates are enabled. A small number of larger particles with a diameter $\leq 1 \mu\text{m}$ in the network of LTO nanoparticles can be seen from the scanning electron micrographs. The particle morphology is largely maintained for modification temperatures of up to 800 °C, as no changes were observed by SEM and TEM characterization (Figure 2A–D). However, a stark impact on the optical material properties can be seen, as the powder changed its color from white to light blue and then to blue. At temperatures above 800 °C, distinct changes of the powder microstructure occur, since the powder density starts to rise markedly (Figure 2E–F). Simultaneously, the color of the samples transforms into dark blue (900 °C) and finally to black (1000 °C). The LTO nanoparticles start to coalesce to larger primary particles with a diameter of about 100 nm at 900 °C (Figure 2E, inset). When adjusting the temperature to 1000 °C, all LTO nanoparticles were transformed into micrometer-large particles with some internal porosity (Figure 2F).

Figure 3A shows the optical absorption spectra of the different LTO samples. The pristine powder exhibits absorption below 420 nm (3 eV), with its main absorption edge in the ultraviolet region at about 320 nm (3.9 eV). Accordingly, the pristine powder appears white, as light in the visible range is almost entirely reflected. This absorption energy range is typical for wide-band-gap semiconductors and corresponds to electron excitation from the filled valence band into the empty conduction band.^[68] The theoretical band gap of LTO was calculated to be 2.0–2.3 eV,^[69,70] but experimentally obtained results in the range of 3–7 eV align with our findings.^[68,71–73] After heat treatment at 500 °C in hydrogen atmosphere, a wide absorption band arises centered at around 1200 nm (1 eV). When further increasing the treatment temperature to 600 °C, this absorption band becomes more pronounced and broader. For temperatures exceeding 800 °C, the expansion leads to near 100% absorption in the low energy range up to 2500 nm (0.5 eV) and a small area at 320–800 nm with only minor absorption. This behavior strongly suggests additional absorption in the wavelength region beyond our experimental limitation of 2500 nm. For highly modified powders (i.e., L/900 and L/1000), absorption at 320–800 nm is further increased and near 100% absorption over all investigated wavelengths can be observed for L/1000. We attribute the absorption band to electron transitions from intra-band-gap energy levels (in-gap states) to the conduction band.^[74] Such in-gap-states have been reported for oxygen-deficient LTO (Ref. [56]) and TiO₂ (Ref. [74–76]) and are related to oxygen vacancy formation and associated Ti³⁺ valence states. Our results suggest that the in-gap states initially occur at about 1 eV below the conduction band (absorption maxima). With increasing treatment temperature, the rising Ti³⁺ content causes the in-gap states to form energy bands which expand in direction of the conduction and valence band simultaneously (i.e., absorption band widens). For

Table 2. Temperature dependent mass change of LTO at different temperatures with respect to a temperature of 450 °C and calculated oxygen loss, theoretical LTO formula unit with average Ti oxidation state (OS), number (#) of Ti³⁺ respectively Ti⁴⁺ ions per LTO formula unit, and Ti³⁺/Ti⁴⁺ ratio assuming LTO phase preservation.

Temperature [°C]	Mass [%]	O loss [%]	Formula unit	Avg. Ti OS	#Ti ⁴⁺	#Ti ³⁺	#Ti ³⁺ / #Ti ⁴⁺
500	99.99	0.02	Li ₄ Ti ₅ O ₁₂	4.00	4.99	0.01	< 0.01
600	99.88	0.29	Li ₄ Ti ₅ O _{11.97}	3.99	4.93	0.07	0.01
800	99.17	1.98	Li ₄ Ti ₅ O _{11.76}	3.90	4.52	0.48	0.11
900	98.71	3.08	Li ₄ Ti ₅ O _{11.63}	3.85	4.26	0.74	0.17
1000	98.17	4.38	Li ₄ Ti ₅ O _{11.47}	3.79	3.95	1.05	0.27

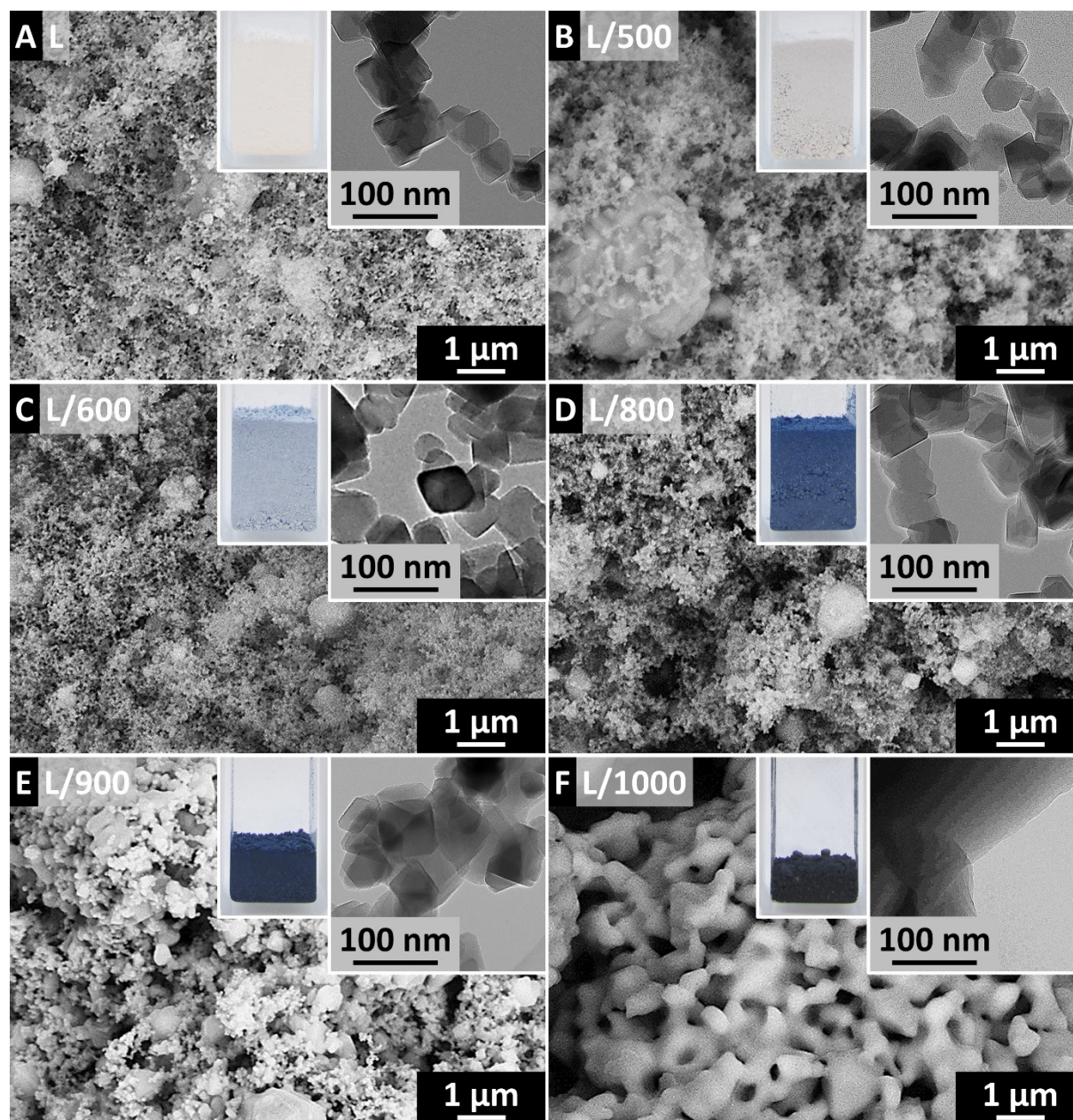


Figure 2. SEM and TEM (inset) micrographs of pristine LTO powder (A) and LTO powder heated to 500 °C (B), 600 °C (C), 800 °C (D), 900 °C (E), and 1000 °C (F) under hydrogen atmosphere. The insets show digital photographs of the respective powders with identical mass (0.3 g each).

highly modified powders, this causes a continuous in-gap band spreading from the band gap into the conduction band or, at the very least, up to 0.5 eV below the conduction band according to the maximum wavelength measurable with our device. Hence, we confirm electron band structures comparable to metals in the strongly modified powders, as electrons can now freely drift due to the coalescence of the occupied “mid-gap bands” and the empty conduction band. This implies a strong modification of the electrical conductivity for oxygen-deficient samples.

Nitrogen sorption isotherms of the LTO powders show a type II shape, which is typically observed for materials in absence of micro- or mesopores (Figure 3B).^[62] The pristine

powder is characterized by a BET specific surface area (SSA) of 25 m²/g and a pore volume of 0.04 cm³/g due to the nano-meter-sized primary particles. Only minor changes of the isotherms and corresponding BET specific surface area (SSA; Table 3) are observed for temperatures ≤ 800 °C, which aligns with the morphologies observed with electron microscopy (i.e., microstructure is conserved/absence of sintering). When further increasing the temperature, we see a strong decrease of BET SSA and total pore volume below 4 m²/g and 0.01 cm³/g, respectively. This reflects the observed sintering of LTO primary particles and the drastic powder morphology changes of these samples.

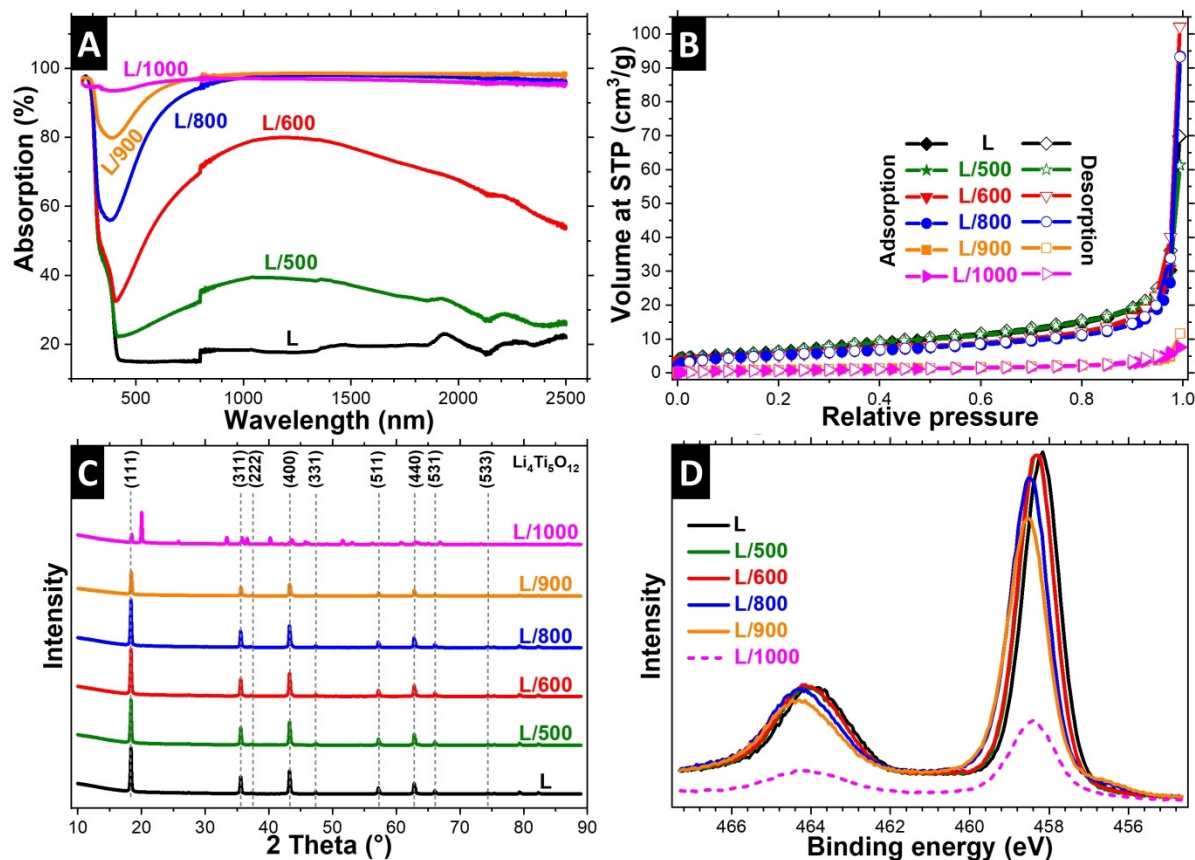


Figure 3. Material characterization of pristine LTO and LTO powder heated to different temperatures under hydrogen atmosphere. UV-VIS-NIR absorption spectra (A), gas sorption isotherms (B), X-ray diffraction pattern with indexed position of spinel $\text{Li}_4\text{Ti}_5\text{O}_{12}$ lattice planes (C), Ti 2p high-resolution XPS-spectra and UV/VIS adsorption spectra (D).

X-ray diffraction patterns were recorded (Figure 3C) to examine the crystal structure and crystalline phase content of the LTO powders. Broad signals, coming from spinel LTO (JCPDS 49–0207), and a minor contribution of rutile TiO_2 (JCPDS 21–1276) were detected in the pristine material. The phase distribution of the sample was calculated to 99:1 by mass (LTO/ TiO_2) according to Rietveld refinement of the XRD patterns (Table 4). After hydrogen annealing, an additional monoclinic Li_2TiO_3 (JCPDS 4–009–2812) phase forms and the fraction of spinel LTO and rutile TiO_2 decreases with increasing temperature. The Li_2TiO_3 phase tends to increase with rising temperature, but does not exceed 8 mass% up to 900 °C. The LTO crystallinity is largely maintained up to a temperature of 800 °C, as deduced from the almost constant XRD signal amongst these samples. For L/900, partial amorphization accompanied

by a contraction of the (111) lattice planes takes place as seen from a decrease of the XRD signal intensity decreases and a shift of the (111) reflection to higher diffraction angles, Figure 3C and Figure S1. This supports our hypothesis of a transition of the reaction mechanism during annealing in hydrogen between 800–900 °C, since the removal of high energy oxygen sites could likely induce the collapse/amorphization of the LTO structure via a distorted crystalline transition state.

It is probable that the amorphization causes the abrupt microstructure change for the samples treated at ≥ 900 °C due to a higher material diffusivity in the disordered state or even by liquefaction of the amorphous phase at high temperature.

Table 3. Specific surface area and pore volume of the pristine and modified LTO powders.

Sample	BET SSA [m ² /g]	Pore volume [cm ³ /g]
L	25	0.04
L/500	24	0.04
L/600	19	0.03
L/800	19	0.03
L/900	4	0.01
L/1000	3	0.01

Table 4. Crystalline phase contents according to Rietveld fitting of the measured X-ray diffraction patterns.

Sample	$\text{Li}_4\text{Ti}_5\text{O}_{12}$ spinel [mass%]	TiO_2 rutile [mass%]	Li_2TiO_3 monoclinic [mass%]	$\text{Li}_{0.57}\text{Ti}_{0.86}\text{O}_2$ ramsdellite [mass%]
L	99	1	n.d. ^[a]	n.d.
L/500	94	1	5	n.d.
L/600	94	1	5	n.d.
L/800	92	< 1	8	n.d.
L/900	92	n.d.	8	n.d.
L/1000	6	n.d.	21	73

[a] n.d.: not detectable.

When the temperature reaches 1000 °C, a phase transformation of LTO mainly to ramsdellite $\text{Li}_{0.57}\text{Ti}_{0.86}\text{O}_2$ (JCPDS 1–070-2365) and some monoclinic Li_2TiO_3 takes place (Figure 3C, Table 4). According to the phase diagrams, LTO starts to decompose at temperatures above 1015 ± 5 °C into ramsdellite $\text{Li}_{0.57}\text{Ti}_{0.86}\text{O}_2$ and monoclinic Li_2TiO_3 .^[77] Hence, the high-temperature phase transformation observed in our case is likely promoted by growing structural instabilities due to the removal of high energy oxygen atoms from the LTO lattice at temperatures above 800 °C (Section 2.1.). Initially, this leads to the contraction of the (111) lattice planes with a subsequent amorphization and phase transformation.

XPS survey scans were recorded to calculate the near-surface chemical composition (Table 5). All powders show XPS signals for Li, C, O, and Ti. For the pristine material, the ratio of Li/Ti/O elements is about 1:2:6, which should theoretically be at around 1:1:3 for LTO. The excess amount of Ti and O and its ratio of 1:2 indicates the presence of an additional TiO_2 side phase. According to the XPS elemental chemical composition, the ratio of LTO to TiO_2 is roughly 1:1. This differs from the 99:1 ratio determined by XRD characterization and suggests that the TiO_2 phase is either mainly located in near-surface regions and/or that amorphous TiO_2 is present in the sample, since XPS only probes near-surface regions and XRD solely detects crystalline phases. About 10 atom% of carbon was detected in the surface of the pristine powder. Such values can be caused by surface absorption of impurities from the environment and are commonly observed for samples which were not strictly prepared and stored in ultrahigh vacuum conditions. The near-surface chemical composition is largely maintained for the modified LTO powders treated at temperatures of up to 900 °C. For L/1000 an abrupt increase of Li and C is observed, while the Ti amount simultaneously decreases.

All powders show an O 1s peak centered at about 529.6–529.9 eV (Figure S2A), and a Li 1s peak at about 54.2–54.7 eV (Figure S2C), which are characteristic binding energies of electrons originating from O respectively Li in metal oxides like LTO.^[65,78] For L/1000, an additional peak arises at 531.7 eV (O 1s) and at 55.2 eV (Li 1s), which can be attributed to oxygen and lithium ions in Li_2CO_3 .^[78] This is further supported by the C 1s peak of L/1000 at 289.9 eV (Figure S2B), which can be assigned to carboxylic groups.^[79–81] Therefore, the observed change of chemical composition is caused by the formation of a Li_2CO_3 containing phase at the surface of L/1000. While the exact origin of this phase remains unclear, surface precipitation of

Li_2CO_3 during the phase transformation or a chemical reaction with ambient CO_2 during sample transfer is conceivable (i.e., caused by the oxophilicity of the highly oxygen-deficient material). A drift of the XPS peaks to higher binding energies with increasing treatment temperature can be seen in all high-resolution XPS spectra, except for the C1s spectra, which was shifted to 285 eV for calibration. It is unlikely that the observed drift is caused by surface charging effects, as it is pronounced to different degrees for the various elements. Several interacting factors could be responsible for the drifting of the XPS peaks: i) elevation of the Fermi-level caused by the high oxygen vacancy concentration, ii) change of chemical environment due to surface phase transformation, and iii) varying degree of near-surface band bending due to contact formation to distinct surface phases (e.g., Li_2TiO_3) and/or surface adsorbates (e.g., O_2 , H_2O or CO_2). Especially latter have been linked to energy band bending phenomena and binding energy drifts in TiO_2 .^[82–84] An adsorption of oxygen-containing species is likely due to the general high oxophilicity of titanium (especially in its reduced state; Ref. [84]) and the high oxygen deficiency of the materials treated at elevated temperatures. This is also supported by the slightly higher mass of high temperature modified powders (L/800, L/900, and L/1000) when compared to the thermogram (Figure 1A). Moreover, the shoulder at 531–533 eV in the O 1s spectra for the heat-treated powders suggests a rising tendency for oxygen and water absorption (especially recognizable for L/800 and L/900). This shoulder has been connected to hydroxyl groups formed by chemisorption of water and to chemisorbed oxygen on LTO and TiO_2 surfaces.^[65,66]

The Ti 2p high-resolution XPS spectra (Figure 3D) of the LTO powders show the high-intensity Ti 2p3/2 peak centered at 458.2–458.6 eV and a low-intensity Ti 2p1/2 peak at 463.9–464.4 eV. These binding energies are typically observed for tetravalent titanium.^[65,85] The Ti 2p peak intensity of L/1000 is severely decreased due to the arising Li_2CO_3 side phase at this treatment temperature. An additional small shoulder of the Ti 2p3/2 peak emerges for the treated powders at about 455.6–457.1 eV, which can be attributed to trivalent titanium.^[65,85] Both components have been fitted by two separate peaks and the resulting $\text{Ti}^{3+}/\text{Ti}^{4+}$ ratio is provided in Table 5. For peak-fitting, we assumed the Ti^{3+} component for all samples to obtain consistent data. Accordingly, small amounts of Ti^{3+} are also obtained for the pristine sample. We did not identify a significant difference of the $\text{Ti}^{3+}/\text{Ti}^{4+}$ ratio between the pristine material and L/500 respectively L/600, while powders treated at higher temperatures show a minor increase of the Ti^{3+} species. The calculated ratio of the XPS measurements for high-temperature treated samples is lower by a factor of 2–5 compared to the ratio obtained from the TG-MS results (Table 2). Hence, the chemisorption of gaseous species (O_2 , H_2O , or CO_2) during sample transfer results in a near-surface re-oxidation of titanium. However, the bulk vacancy concentration is largely maintained, since reduced LTO is typically stable in air for weeks/months.^[56] Accordingly, XPS results must be carefully interpreted for valence-tuned LTO and a shift of 2p X-ray photoelectron spectra, like proposed by Shen et al.,^[57] cannot be seen as evidence for the formation of Ti^{3+} valence states.

Table 5. XPS elemental analysis and calculated ratio of $\text{Ti}^{3+}/\text{Ti}^{4+}$ species of pristine and of the modified LTO powders. The average value and the standard deviation refer to measurements at three different positions.

Material	Li content [atom%]	C content [atom%]	O content [atom%]	Ti content [atom%]	$\text{Ti}^{3+}/\text{Ti}^{4+}$
L	10.9 ± 0.4	12.5 ± 0.3	56.3 ± 0.3	20.2 ± 0.2	0.026
L/500	10.6 ± 0.4	12.4 ± 0.2	56.5 ± 0.3	20.6 ± 0.1	0.024
L/600	10.0 ± 0.8	12.5 ± 0.1	56.8 ± 0.6	20.2 ± 0.2	0.025
L/800	10.2 ± 0.5	13.0 ± 0.3	56.3 ± 0.2	20.1 ± 0.2	0.046
L/900	10.5 ± 1.1	14.2 ± 0.5	56.1 ± 0.5	19.2 ± 0.1	0.062
L/1000	18.3 ± 1.6	18.9 ± 0.9	55.0 ± 0.8	7.1 ± 1.5	0.053

Summarizing these data, we see that the bespoke reduction of titanium oxidation state was successfully achieved by a simple and rapid process. It consists of fast heating under hydrogen and subsequent immediate cooling, without the need for time-consuming/cost-ineffective high-temperature holding steps or elaborate high-pressure techniques. This procedure maintains the LTO nanostructure and largely prevents the sintering of particles due to the short timespan in the high temperature regime. When operating in an appropriate temperature range (i.e., $\leq 800^\circ\text{C}$), the titanium oxidation state can be adjusted, while circumventing LTO phase transformations or amorphization.

2.3. Understanding the Rate Limitations of Nanoparticulate Lithium Titanate Electrodes

To enable high power operation of electrochemical energy storage devices, like hybrid supercapacitors, the solid Li-ion transport paths through the active materials need to be minimized, while the electrode/electrolyte interface should be maximized.^[86] This is due to the much higher Li-ion conductivity of the liquid electrolyte as compared to solid-state Li-ion diffusion inside the electrode materials.^[86] From this point of view, nanosizing of the active material is a common and effective approach to resolve this issue. In case of insulating active materials, like $\text{Li}_4\text{Ti}_5\text{O}_{12}$, this can entail additional challenges with the electrochemical stability, as we have shown recently.^[14] A decreasing particle size of the insulating $\text{Li}_4\text{Ti}_5\text{O}_{12}$ will reduce the insulating to conductive particle size ratio (conductive carbon size is constant). According to Monte Carlo simulations of He et al.,^[87] a reduction of this ratio will raise the threshold of conductive additive material required for electrical percolation. Hence, nanometer-sized $\text{Li}_4\text{Ti}_5\text{O}_{12}$ is very effectively disrupting the electrical percolation paths^[14] and the electrical conductivity of a nanopowder may be much more limiting as compared to a powder with a larger particle size. In the case of LTO, this only holds if the low electrical conductivity of the Li-poor phase ($\text{Li}_4\text{Ti}_5\text{O}_{12}$) is the rate limiting factor and the emerging conductive Li-rich phase ($\text{Li}_7\text{Ti}_5\text{O}_{12}$) is not sufficient to provide the required electrical percolation during cell operation. In a first step, we will clarify this issue via rate capability assessment of electrodes containing no CB (0-L) and electrodes with 5 mass% respectively 20 mass% CB (5-L respectively 20-L) as state-of-the-art literature on this topic is contradictory (Section 1).

To probe the electrical percolation, electrodes were sandwiched between two titanium pistons, while applying a current and measuring the potential between both pistons. For 0-L and 5-L, a pronounced initial voltage increase, followed by a lower subsequent polarization can be observed (Figure S4A). This polarization indicates that electrical charge is accumulated between both pistons due to the insulating nature of these electrodes (working principle of a parallel plate capacitor). Accordingly, the carbon concentration for 5-L is not sufficient to reach the percolation threshold. By contrast, for 20-L no

polarization was detectable due to the high amount of conductive carbon (i.e., percolation threshold is reached).

The electrochemical rate capability of 0-L, 5-L, and 20-L was normalized to the total LTO mass of the electrode and the corresponding data are shown in Figure 4a. At low rates of 0.1C, the LTO capacity is about 160 mAh/g for 5-L, which is slightly lower as compared to the theoretical value of 175 mAh/g.^[16] Such values are common for commercial materials and can, for example, be caused by small impurities.^[11,56] This implies that almost all active material particles do possess a sufficient electrical contact to the current collector. The slightly smaller values of 0-L are likely connected to a minor amount of electrically insulated particles, while 20-L is about in the statistical scatter range of 5-L results. For 20-L, the electrical percolation is established by the CB matrix. Since 0-L and 5-L are electrical insulating and do not have a CB percolation network, the electrical percolation necessarily must be formed during charging. Electrical percolation is established during lithiation when electrically conductive, Li-rich LTO is being formed.^[14] With increasing the C-rate, the behavior changes and we see significant differences between 0-L, 5-L, and 20-L. In case of carbon-free electrodes, a sharp decline of the LTO capacity is observed and the capacity drops from about 150 mAh/g to 30 mAh/g when raising the charging/discharging rate from 0.1C to 20C. We attribute this to a cascade-like effect which de-activates more and more conductive paths during delithiation when conductive Li-rich phase is being replaced by the insulating Li-poor phase.^[14] At high rates, this process seems to be amplified due to the smaller timescale of one discharge cycle and the associated more inhomogeneous distribution of charge and potential differences throughout the electrode.^[14] Hence, well-connected areas of Li-rich LTO particles will be delithiated at first and the most effective conductive paths are lost shortly after initiation of the discharge.

The rate performance of 5-L is superior to 0-L, although the carbon content of 5-L is not sufficient to provide effective electrical percolation. In this case, the conductive paths are likely co-provided by CB and Li-rich LTO. Therefore, the conductive paths are only partially de-activated during fast de-lithiation as some conductivity can still be maintained by carbon and the conductivity of the Li-rich phase mostly serves to connect certain electrode areas. Cells based on 20-L show superior rate performance as compared to 0-L and 5-L, since electrical percolation is solely established by the conductive carbon network. Hence, the high rate behavior of 20-L is not dictated by the arising Li-poor LTO phase and is limited by intra-particle Li-ion and/or electron conduction kinetics. The differences between 20-L and 5-L are likely connected to the small size of the LTO nanoparticles, since the electrical percolation of conventional micrometer-sized particles is usually already achieved at carbon contents below 5 mass%.^[88-90] From these results, we see that the rate limitation of nanoparticulate LTO based cells is caused by the low conductivity of the Li-poor phase. Only when we remove this rate limitation by increasing the carbon content, this behavior changes and the rate capability gets determined by intra-particle conductivity limitations. It is insufficient to only consider the high conductivity of the Li-rich phase to identify the rate limitations of LTO based

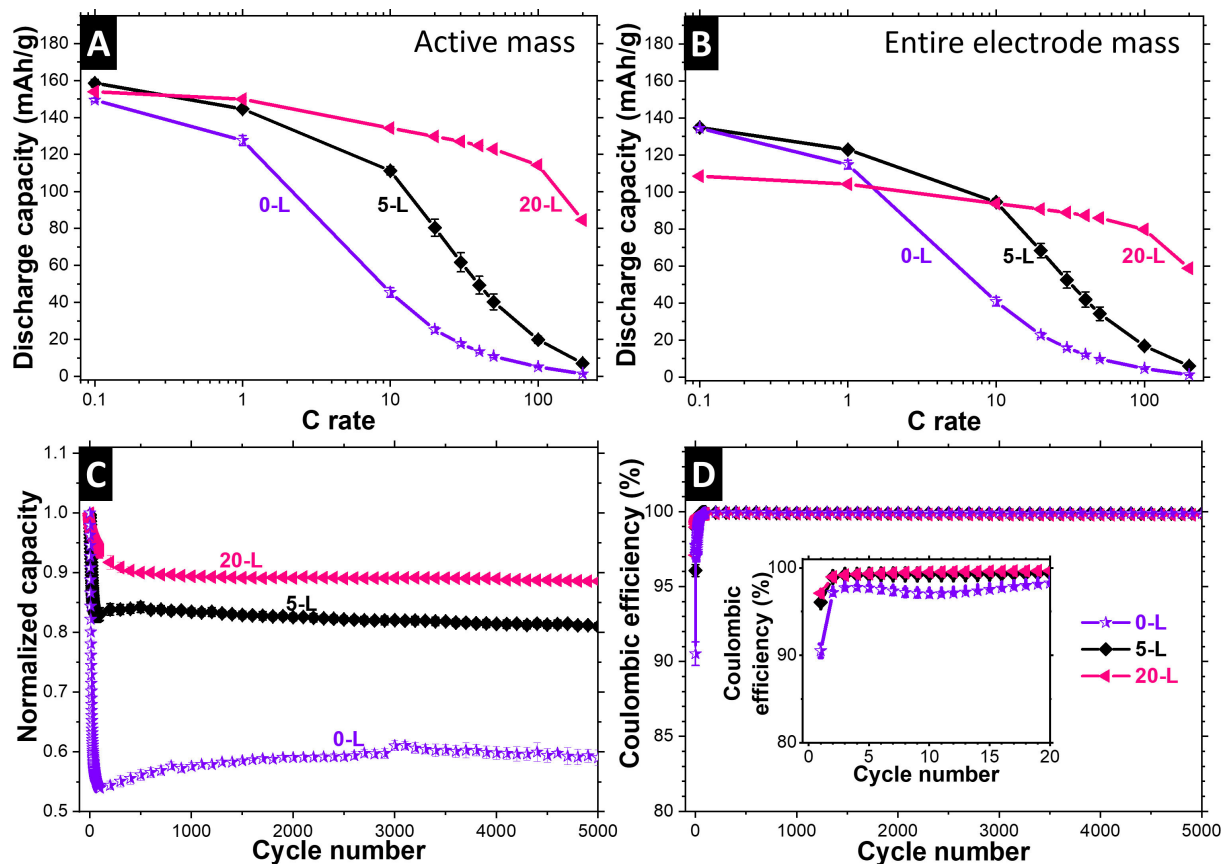


Figure 4. Rate performance based on active or electrode mass (A,B). Electrochemical cycling stability (C) and Coulombic efficiency at charging/discharging rates (D) of 10C of electrodes containing LTO with different carbon concentrations.

electrodes,^[25] since the emerging de-lithiated phase can heavily disrupt conduction paths during fast de-lithiation.

Our findings are contradictory to the results to Wang et al. who concluded that “slow ionic transport (not low electronic conductivity) limits the rate performance of $\text{Li}_4\text{Ti}_5\text{O}_{12}$ anodes”.^[26] In this study, the influence of carbon coatings was investigated. Non-coated LTO was found to be superior to coated LTO, although the carbon additive content (10 mass%) of the electrodes was not considered (i.e., carbon concentration might already be sufficient to provide electrical percolation and carbon-coating is redundant). Moreover, from determination of Li-ion diffusion coefficients, the authors concluded that the “carbon layer hinders lithium ion diffusion into the $\text{Li}_4\text{Ti}_5\text{O}_{12}$ lattice” and explains the impaired rate performance.^[26] While this demonstrates that a carbon layer can act as an additional barrier for lithium ion diffusion under certain circumstances, it should not be considered as a general evidence for Li-ion diffusion limitation in LTO based electrodes. Such a conclusion can only be drawn when specifically modifying the intra-particle electrical conductivity without impacting Li-diffusion kinetics. Therefore, our results show that the electrode conductivity can be rate limiting for LTO-based cells, but we cannot specify if the intra-particle kinetics are either dictated by Li-ion diffusion or by electrical conductivity.

The electrochemical cycling stability at 10C scales with the carbon content (Figure 4C). Lower Coulombic efficiencies are

observed during the first cycles of 0-L and 5-L cells. Carbon-free electrodes drop below 60% of the initial capacity already after 30 cycles, while about 90% of the capacity is maintained for 20-L even after 5000 charge/discharge cycles. These findings are consistent with our recent work and likely attributed to local degradation spots caused by inhomogeneous current/voltage distribution throughout the electrode for compositions without carbon or with low carbon content.^[14] We conclude that carbon-free/low carbon content based LTO cells may be suitable for certain low rate applications, but this deteriorates the rate capability and electrochemical stability. The usage of LTO for such applications is questionable considering that these are critical unique selling points of LTO based cells over other anode materials with higher capacity (e.g., Sn, Si, or SiOC; Ref. [91]).

Undoubtedly, a high carbon content greatly improves the electrochemical performance, but it comes at the expense of a decreased overall electrode capacity since carbon is electrochemically inactive in the operating potential of LTO (Figure 4B). This performance is of significantly greater importance for practical application in an electrochemical energy storage device. For such applications, it is not of interest how well a small quantity of LTO performs in a massive matrix of carbon; the main challenge is to achieve a superior performance with the lowest possible amount of conductive carbon. Therefore,

increasing the intrinsic electronic conductivity of LTO is the best solution, as we will show throughout the next section.

2.4. Electrochemical Properties of Modified LTO Powders

The carbon content for all follow-up experiments was kept at 5 mass% since this composition was found to be superior to carbon-free electrodes and yet possess a high capacity with respect to the entire electrode mass. At this carbon concentration, the rate capability remains limited by the low conductive Li-poor phase and an improvement of the intrinsic electrical conductivity of LTO is required for high rate operation.

In case of 5-L/500 and 5-L/600, the low amount of Ti^{3+} valence states did not lead to significant enhancement of the electrical conductivity and the electrode still is electrically insulating (Figure S4B). By contrast, treatment at higher temperatures did lead to massive enhancement of the electrical conductivity, since no polarization was detectable for these electrodes (Figure S4B).

At low charge/discharge rates, the capacity of pristine LTO is maintained for the modified powders L/500, L/600, and L/800 (Figure 5A). This confirms that enough Ti^{4+} is present to attain the full LTO capacity. These species are vital for the LTO redox

reaction, as Ti^{4+} is reduced to Ti^{3+} during lithiation to ensure charge neutrality during Li-insertion. The characteristic two-phase lithiation/de-lithiation mechanisms of LTO is preserved for all LTO powders as can be deduced from the flat voltage plateau below 1.6 V vs. Li/Li^+ (Figure 6A) and the two redox peaks between 1.4–1.7 V vs. Li/Li^+ of the cyclic voltammograms (Figure 6C).^[92] With increasing treatment temperature, the voltage plateau position seems to be continuously lowered towards small potentials vs. Li/Li^+ (Figure 6A, inset). A shift of the voltage plateau may be linked to overpotential development due to a deterioration of the redox process kinetics. However, a rising overpotential would simultaneously force the lithiation plateau to lower potentials and the de-lithiation plateau to higher potentials vs. Li/Li^+ .^[14] Since both plateaus are coincidentally shifted to lower polarizations (e.g., about 30 mV for 5-L/900), the half-wave potential (HWP) of the LTO lithiation/de-lithiation reaction seems to be modified for the oxygen-deficient LTO samples. The HWP is correlated to the energy, which is required to insert or remove Li-ions into the active materials.^[93] Since the HWP is shifted to higher polarizations for the modified LTO powders, this energy seems to be increased in case of the modified powders. Possibly, this is linked to lattice distortion of the oxygen-deficient samples.^[93] A shifting of the LTO HWP to lower voltages vs. Li/Li^+ is beneficial for an

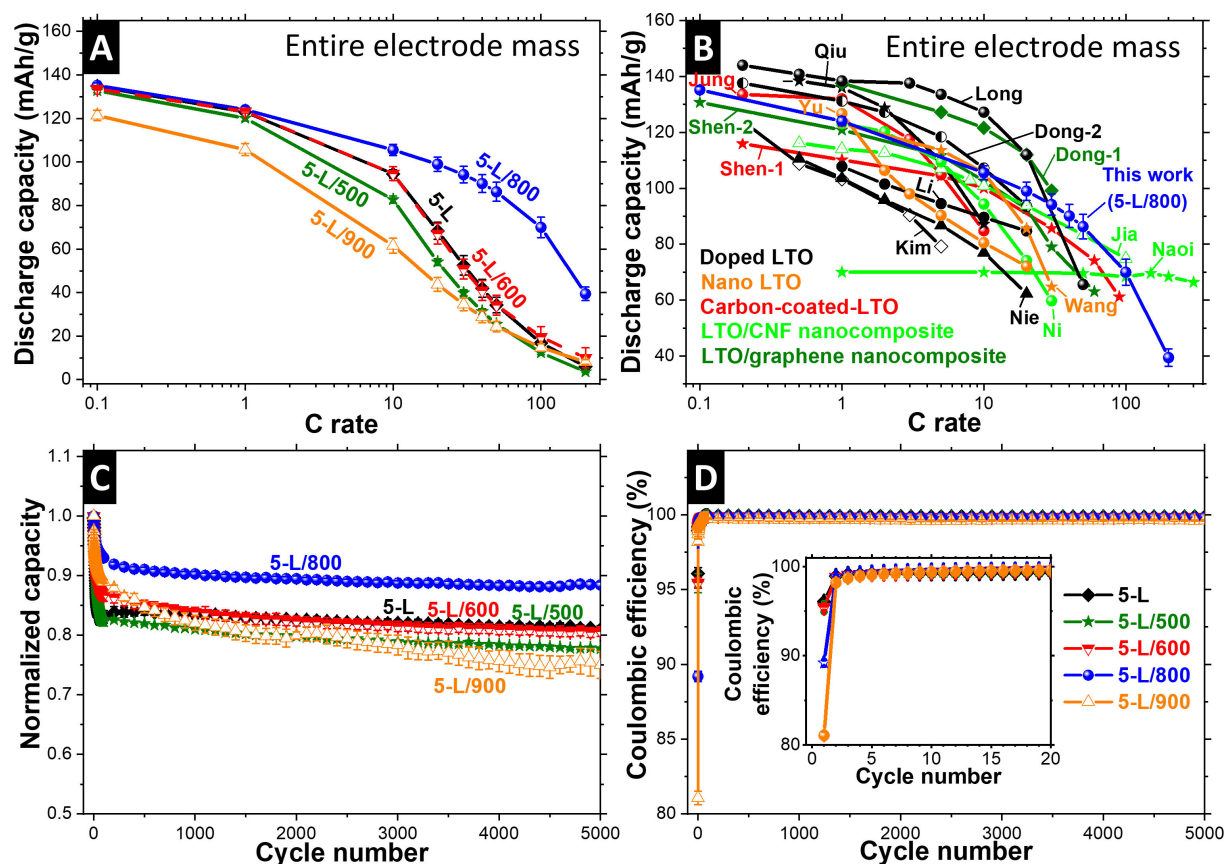


Figure 5. Rate performance (based on electrode mass) (A) including a comparison to literature (B), electrochemical cycling stability (C) and Coulombic efficiency at charging/discharging rates (D) of 10C of electrodes containing modified LTO. The literature values were converted to electrode mass with active mass capacities and electrode composition stated in the respective references (Dong-1,^[38] Dong-2,^[99] Jia,^[28] Jung,^[107] Kim,^[108] Li,^[109] Long,^[110] Naoi,^[17] Ni,^[32] Nie,^[58] Qiu,^[56] Shen-1,^[111] Shen-2,^[112] Wang,^[103] Yu^[113]).

LTO-based electrochemical energy storage device due to the proportionality of the energy density to the potential. Below 1.3 V vs. Li/Li^+ , a small decrease of the voltage profile slope can be observed (Figure 6A), which may be connected to a minor lithiation beyond $\text{Li}_7\text{Ti}_5\text{O}_{12}$ composition.^[15,94–96] The reaction seems to be strongly influenced by electrochemical kinetics, since it was only observed for low rates of 0.1C (Figure 6A–C). This could be associated to the rising ionic diffusion resistance, which is observed when the Li-rich phase ($\text{Li}_7\text{Ti}_5\text{O}_{12}$) is further lithiated.^[14]

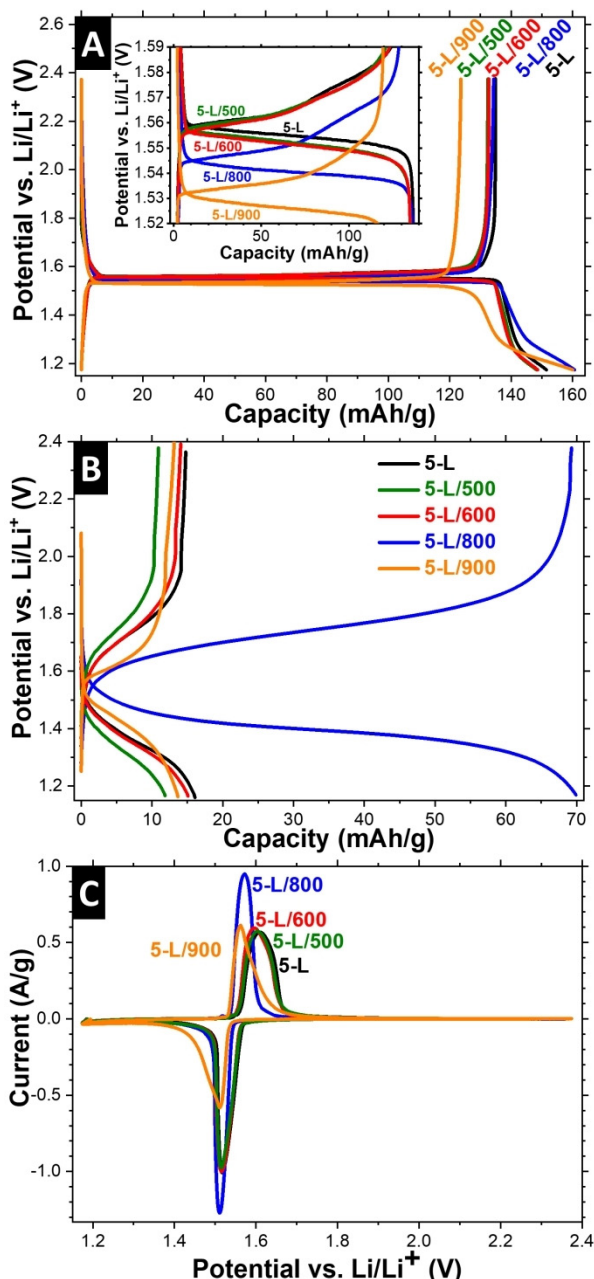


Figure 6. Galvanostatic charge and discharge curves normalized to electrode mass of the 3rd cycle measured at 0.1C (A) and at 100C (B). Cyclic voltammograms recorded with 0.1 mV/s (C). The inset of (A) shows a higher magnification of the lithiation/de-lithiation plateau of LTO at 0.1C.

Our data show no additional capacity in the working potential window of LTO for monoclinic Li_2TiO_3 . This is consistent with literature, as monoclinic Li_2TiO_3 has a poor Li-ion storage capacity of about 20 mAh/g.^[97] The latter value would mathematically translate to an additional contribution to the overall electrode capacity of about 1 mAh/g in our case. Since the full capacity of LTO is maintained and the capacity contribution of the Li_2TiO_3 side phase is negligible, we can confirm LTO phase preservation up to treatment temperature of 800 °C. We conclude that emerging crystalline Li_2TiO_3 at low temperatures (800 °C and below) cannot arise from a decomposition of LTO during heat treatment as this should entail a simultaneous capacity decrease. It is likely that the observed rutile TiO_2 phase could react with residual Li_2CO_3 (LTO is usually synthesized by thermal annealing of TiO_2 and Li_2CO_3 ; Ref. [55, 98, 99]) to form Li_2TiO_3 . This would agree with the observed CO_2 release that we measured during thermogravimetric analysis. However, rutile TiO_2 only makes up about 1 mass% of the entire mass of the pristine LTO and no crystalline Li_2CO_3 was detected during XRD characterization. Since the amount of the Li_2TiO_3 side phase is much larger (about 8 mass% for L/800), it must arise from an amorphous phase or phases, which cannot be detected by XRD. Such amorphous phases could decompose or crystallize into monoclinic Li_2TiO_3 after thermal annealing under hydrogen atmosphere at temperatures of 800 °C and below. This hypothesis is supported by the measured capacity of LTO, which is about 92 % of its theoretical capacity (i.e., 8 mass% of electrochemically inactive impurity phase might be contained in the pristine LTO). It is reasonable to assume that the amorphous phases are nearly entirely converted into monoclinic Li_2TiO_3 at 800 °C. Hence, the LTO content only seemingly decreases, simply due to the rise of an additional crystalline phase and its impact on the phase distribution. Based on the entire mass (amorphous and crystalline), the LTO content remains constant. The capacity for electrodes based on 5-L/900 is decreased by about 12 mAh/g, likely caused by the partial LTO amorphization, the contraction of the (111) lattice planes, and/or related to the drastic changes of the particle morphology.

The reversible capacity of 5-L/1000 is further decreased to about 90 mAh/g at low rates (Figure S3), which is related to the high-temperature phase transformation of LTO into Li_2TiO_3 and $\text{Li}_{0.57}\text{Ti}_{0.86}\text{O}_2$. In this case, the capacity is mainly accomplished by the $\text{Li}_{0.57}\text{Ti}_{0.86}\text{O}_2$ phase as the LTO content in the electrode and the charge storage capabilities of Li_2TiO_3 are negligible. According to literature (e.g., Ref.^[100]), $\text{Li}_{0.57}\text{Ti}_{0.86}\text{O}_2$ can reversibly store about 150 mAh/g, which translates to 130 mAh/g normalized to the electrode mass in our case. The capacity difference may originate from an incomplete phase transformation with electrochemically inactive amorphous phases and/or large particles. According to Tsuyumoto et al.,^[101] the black color and the two differently sloped areas during galvanostatic charging (Figure S3B) are characteristic for the oxidized ramsdellite-type lithium titanate ($\text{Li}_{0.5}\text{TiO}_2$). However, 5-L/1000 electrodes show an inferior rate capability due to the high amount of Li_2TiO_3 and the large active material particle size of this sample. Hence this

material is not suitable for high power applications and was not further investigated.

At high rates, the capacity initially decreases for the weakly modified sample 5-L/500, is restored for 5-L/600, reaches an optimum for 5-L/800, and is diminished for 5-L/900 (Figure 5A). This behavior suggests that an impaired Li-diffusion must arise with increasing treatment temperature, as the electrical conductivity is tendentially increased due the rising Ti^{3+} concentration. Since the surface area and powder morphology is barely altered at temperatures $\leq 800^\circ C$, this decreasing Li-diffusion kinetic must be related to the emerging Li_2TiO_3 phase and the associated decreasing fraction of rutile and/or amorphous TiO_2 . In fact, small amounts of anatase or rutile TiO_2 impurity phases are known to beneficially impact the rate performance of LTO.^[102,103] Moreover, monoclinic Li_2TiO_3 is a poor Li-ion conductor^[104,105] and its presence likely also deteriorates the cell performance. For 5-L/500, the aggravation of Li-ion diffusion outweighs the minor increase of electrical conductivity and the overall rate performance declines. When increasing the treatment temperature, the Li_2TiO_3 content does only marginally change, whereas the Ti^{3+}/Ti^{4+} ratio and the associated electrical conductivity gradually rises. Hence, the gain in electrical conductivity first compensates (5-L/600) and then outweighs (5-L/800) the diminishing Li-ion diffusion kinetics after heat treatment. In case of 5-L/900, the abrupt change of particle microstructure further decreases the Li-diffusion kinetics. An increased particle size and the simultaneous decreased electrode/electrolyte interface area lead to increased solid Li-ion diffusion lengths and the positive effect of electrical conductivity is outweighed. At ultra-high C-rates of 100C, a capacity of about 70 mAh/g is maintained for 5-L/800, whereas all other samples with equal carbon contents only deliver capacities of around 15 mAh/g (Figure 6B). These superior electrochemical kinetics of 5-L/800 can also be deduced from the sharp redox peaks observed during cyclic voltammetry measurements (Figure 6C).

While powders treated at $500^\circ C$, $600^\circ C$, and $900^\circ C$ are comparable to the pristine sample, a strong improvement of the cycling stability is achieved for 5-L/800 (Figure 5C). For this electrode, about 90% of the initial capacity is remained after 5000 charge/discharge cycles at 10C, which is like electrodes containing excessive amounts of carbon (20-L). The capacity decay pattern is almost identical for 5-L/800 and 20-L as both electrodes show a pronounced declining capacity during the first cycles and an almost constant capacity for the subsequent cycles. This is related to the increased fraction of Ti^{3+}/Ti^{4+} and the associated increase of electrical conductivity of the delithiated phase. Furthermore, the increased amount of oxygen vacancies and titanium with Ti^{3+} valence state does not alter the electrochemical stability of the cells. Since these arguments are also valid for 5-L/900, the presence of the amorphous phase or structural instabilities during cycling caused by the contracted (111) lattice planes explain the inferior stability of this sample. For the slightly modified powders L/500 and L/600, the fraction of Ti^{3+}/Ti^{4+} is too small to strongly increase the electrical conductivity and these samples show a similar cycling behavior as the pristine powder. The Coulombic

efficiency decreases when using a higher annealing temperature, for the first cycle and then stabilizes for the subsequent cycles (Figure 5D). This behavior cannot be caused by inhomogeneous current or voltage distribution, as the conductivity of the modified powders is generally higher than of the pristine material, and the latter exhibits a low Coulombic efficiency during all 20 initial cycles (0-L in Figure 4D and Ref. [14]). We therefore ascribe the low first cycle efficiencies to the reduction surface adsorbates on the modified powders. Physisorbed water or OH-species found on the modified LTO powders (Section 2.2) could be reduced to hydrogen.^[3] The declining Coulombic efficiency, when elevating the treatment temperature, is connected to an increasing amount of surface adsorbates. This reduction only occurs during the first cycle, without any impact on the subsequent cycles and the beneficial influence of the improved electrical conductivity outweighs this effect by far. Thereby, a superior cycling stability of 5-L/800 results.

Electrodes based on 5-L/800 compositions possess a similar high-power capability and electrochemical cycling stability as compared to electrodes prepared with excessive amounts of conductive carbon. Simultaneously, the overall electrode capacity can be increased by 24% due the reduced amount of conductive carbon. The superior performance relates to the increased ratio of Ti^{3+}/Ti^{4+} and the associated high electrical conductivity of the de-lithiated phase. Hydrogen treated LTO challenges state-of-the-art LTO-carbon nanocomposites, especially at high C-rates above 50C (Figure 5B). This is mainly attributed to the increased electrical conductivity and the enabling of high rate capabilities at simultaneously low carbon concentration.

2.5. Performance of Hybrid Supercapacitors with Oxygen-Deficient LTO

The superior electrochemical performance of 5-L/800 electrodes was further demonstrated in a hybrid supercapacitor full-cell setup. We employed an AC-LMO composite cathode to adapt to the ultra-high rate capability and high electrode capacity of the anode. The active mass was set to 65 mass% AC and 35 mass% LMO to obtain equal shares of charge stored via fast ion electrosorption at the AC surface and via high capacitive Faradaic reactions of LMO. To operate both electrodes within the stability window of the electrolyte, the anode/cathode mass ratio was adjusted to 0.37. Accordingly, charging the cell to 2.8 V corresponds to a potential of 4.2 V respectively 1.4 V vs. Li/Li^+ for the cathode and anode, respectively (Figure 7A). The potential profile of the anode shows a voltage plateau at about 1.6 V vs. Li/Li^+ caused by the two-phase reaction of LTO,^[92] while the cathode is characterized by two linear regions with distinct slope. The voltage profile of a composite electrode is a superposition of AC and LMO contributions: For voltages below 3.9 V vs. Li/Li^+ the charge is solely stored via ion electrosorption at the interface of an electrolyte and AC, whereas at 3.9–4.2 V vs. Li/Li^+ , we also must consider Faradaic charge storage of LMO and associated Li-ion extraction/insertion.

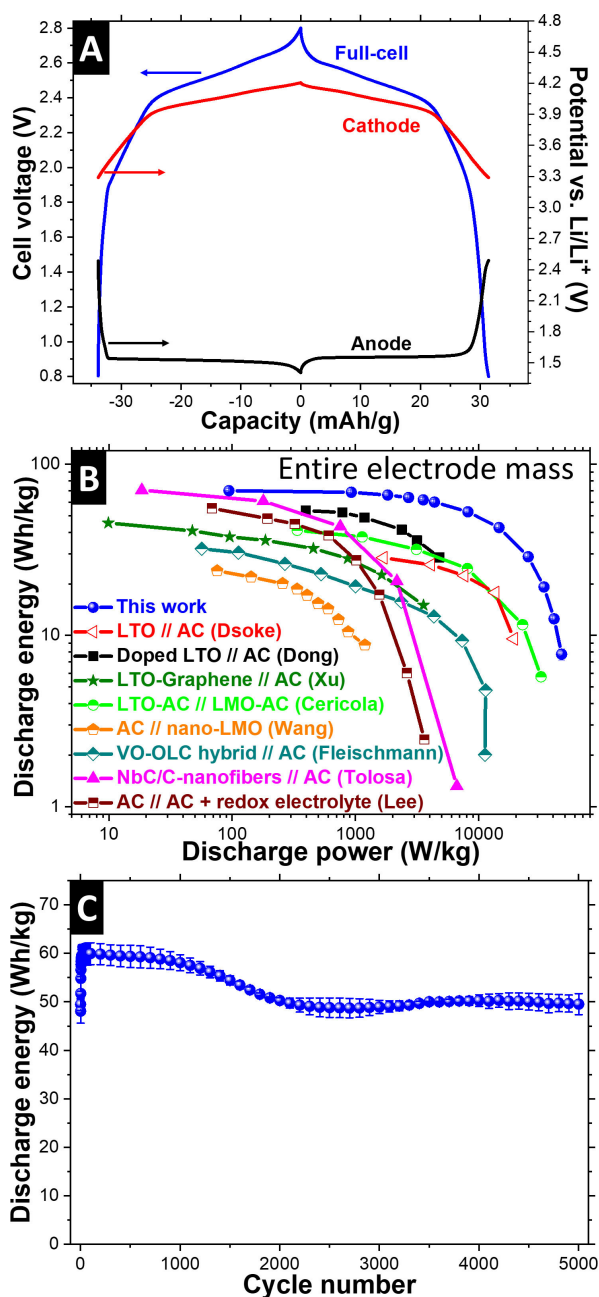


Figure 7. Galvanostatic charge and discharge curves at 1 C, including the voltage profiles of anode and cathode measured against a spectator QRE (A). Ragone-plot with comparison to literature (B). Electrochemical cycling stability at charging/discharging rates of 10C of full-cells employing 5-L/800 anodes and activated carbon/LMO composite cathodes normalized to the entire electrode mass (C). The literature values were converted to electrode mass with active mass energy/power density and electrode composition stated in the respective references (Cericola,^[10] Dong,^[99] Dsoke,^[114] Fleischmann,^[115] Lee,^[116] Tolosa,^[117] Wang,^[118] Xu^[40]).

We also calculated the gravimetric energy and power density of the hybrid supercapacitor from GCPL discharge curves at various rates (g^{-1}). The device is characterized by a high energy density of 70 Wh/kg and an ultra-high maximum power density of 47 kW/kg. These values correspond to 82 Wh/kg and 55 kW/kg based on active mass of both electrodes. About half of the energy can still be maintained, even when

operating the cell with a high power of 20 kW/kg. To the best of our knowledge, such a remarkable combination of high power and energy density have not been reported for 3 V devices so far. Especially in the high-power region above 10 kW/kg this cell concept is superior to other hybrid devices described in literature (Figure 7B).

During GCPL, the initial discharge energy increases during the first 60 cycles (Figure 7C). This behavior must be connected to processes taking place at the cathode, since it did not occur for LTO half-cells. Zhang et al. recently reported that the capacity of AC can increase during cycling in an Li-containing electrolyte.^[106] Since we also observed similar effects for AC, it is likely that the initial energy increase is attributed to the AC contained in our cathodes. About 83% of the maximum energy density is maintained after 5000 continuous charge-discharge cycles at charging/discharging rates of 10C and 100% depth of discharge. When increasing the rate to 100C, the device maintains 78% of the maximum energy after 15000 cycles (Figure S5). Such a behavior is typically observed for high rates, since the time spent in the high polarization regime is lower (per cycle) when increasing the charge/discharge rate.^[14] These outstanding device performances underpin the superior electrochemical performance of 5-L/800 electrodes and are a result of: i) Optimized LTO hydrogen treatment conditions, ii) high active mass content of the electrodes, iii) lowering of the LTO plateau positions, and iv) an AC-LMO composite cathode which is well-adjusted to the ultra-high rate capability of the anode.

3. Conclusions

We have increased the Ti^{3+}/Ti^{4+} ratio of a commercial lithium titanate (LTO) nanopowder through thermal annealing in hydrogen atmosphere. At atmospheric pressure and temperatures above 450 °C, the mass loss and simultaneous water desorption was correlated to the formation of oxygen vacancies and an associated reduction of titanium valence states from Ti^{4+} into Ti^{3+} . This process leads to massive modifications of the optical properties as the powder changes its color from white first to blue and finally to black. The color change is a result of in-gap energy levels caused by oxygen vacancy formation and associated Ti^{3+} valence states. These energy levels initially occur at about 1 eV below the conduction band and transform to in-gap bands, which spread into the conduction band for highly modified powders. Hence electrons can freely drift due to the coalescence of the occupied “mid-gap bands” with the empty conduction band and the intrinsic electronic conductivity of LTO is considerably increased.

The particle morphology, surface area, crystallinity, and the LTO phase content is largely maintained for annealing up to 800 °C as confirmed by SEM, TEM, gas sorption, and XRD characterization. When further increasing the temperature, the powder density decreases as the LTO nanoparticles initially start to coalesce to larger primary particles at 900 °C and finally transform into micrometer-large particles at 1000 °C. These processes are accompanied by partial sample amorphization via a distorted crystalline transition state and LTO phase trans-

formation. We have demonstrated that fast heating of nanoparticulate LTO under hydrogen (10 °C/min) to 800 °C and subsequent immediate cooling is sufficient to obtain appropriate Ti^{3+}/Ti^{4+} ratios. This procedure maintains the LTO structure, prevents the sintering of LTO nanoparticles due to the short timespan in the high temperature regime and does not require any additional high-temperature holding steps or elaborate high-pressure techniques. The associated increase of the intrinsic electrical conductivity of LTO allows us to operate LTO electrodes at C-rates above 50C with a minimal carbon concentration of 5 mass%. Such electrodes are highly competitive to elaborate state-of-the-art LTO-carbon nanocomposites and can deliver a high electrode capacity of about 70 mAh/g (82 mAh/g based on active mass) at ultra-high rates of 100C. Pristine LTO electrodes, on the other hand, are impaired by the low electronic conductivity of the Li-poor LTO phase and therefore require large amounts of electrochemically inactive conductive carbon (20 mass%).

The superior performance of hydrogen treated LTO was further demonstrated in a hybrid supercapacitor full-cell set up against an activated carbon/lithium manganese oxide composite electrode. This device is characterized by an outstanding energy and power density of 70 Wh/kg respectively 47 kW/kg (82 Wh/kg respectively 55 kW/kg based on active mass) and a high electrochemical cycling stability over 5000 charge-discharge cycles (78% after 15000 cycles at 100C).

Acknowledgements

The authors thank C. Engel, A. Fuchs, M. Tuchen, I. Wühl, C. Müller, M. Wessling, and A. Böhme for the support and helpful discussions. We acknowledge funding from the German Federal Ministry for Economic Affairs and Energy (BMWi) in support of the HyBaCap project (award number 03ET6113C) and thank Prof. E. Arzt (INM) for his continuing support. We thank M. Zeiger for his help with transmission electron microscopy and B. Krüner for his support with gas sorption analysis (both at INM).

Conflict of Interest

The authors declare no conflict of interest.

Keywords: lithium titanate · lithium ion battery · electrochemical energy storage · hybrid supercapacitor

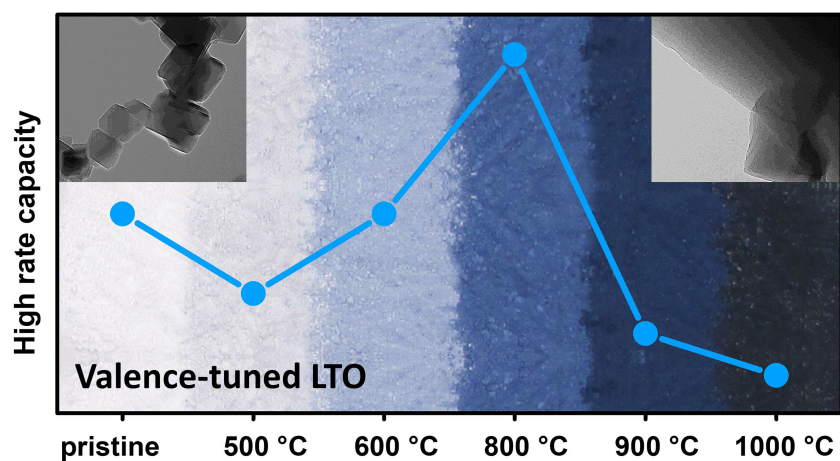
- [1] Z. Yang, J. Zhang, M. C. W. Kintner-Meyer, X. Lu, D. Choi, J. P. Lemmon, J. Liu, *Chem. Rev.* **2011**, *111*, 3577–3613.
- [2] B. Scrosati, J. Garche, *J. Power Sources* **2010**, *195*, 2419–2430.
- [3] F. Beguin, V. Presser, A. Balducci, E. Frackowiak, *Adv. Mater.* **2014**, *26*, 2219–2251.
- [4] M. Salanne, B. Rotenberg, K. Naoi, K. Kaneko, P. L. Taberna, C. P. Grey, B. Dunn, P. Simon, *Nat. Energy* **2016**, *1*, 16070.
- [5] G. G. Amatucci, F. Badway, A. Du Pasquier, T. Zheng, *J. Electrochem. Soc.* **2001**, *148*, A930–A939.
- [6] N. Böckenfeld, R. S. Kühnel, S. Passerini, M. Winter, A. Balducci, *J. Power Sources* **2011**, *196*, 4136–4142.

- [7] N. Böckenfeld, T. Placke, M. Winter, S. Passerini, A. Balducci, *Electrochim. Acta* **2012**, *76*, 130–136.
- [8] D. Cericola, P. W. Ruch, R. Kötz, P. Novák, A. Wokaun, *Electrochem. Commun.* **2010**, *12*, 812–815.
- [9] D. Cericola, P. Novák, A. Wokaun, R. Kötz, *Electrochim. Acta* **2011**, *56*, 1288–1293.
- [10] D. Cericola, P. Novák, A. Wokaun, R. Kötz, *J. Power Sources* **2011**, *196*, 10305–10313.
- [11] D. Cericola, P. Novák, A. Wokaun, R. Kötz, *Electrochim. Acta* **2011**, *56*, 8403–8411.
- [12] B. Wang, Q. Wang, B. Xu, T. Liu, D. Wang, G. Zhao, *RSC Adv.* **2013**, *3*, 20024–20033.
- [13] M. Secchiaroli, R. Marassi, M. Wohlfahrt-Mehrens, S. Dsoke, *Electrochim. Acta* **2016**, *219*, 425–434.
- [14] M. Widmaier, N. Jäckel, M. Zeiger, M. Abuzarli, C. Engel, L. Bommer, V. Presser, *Electrochim. Acta* **2017**, *247*, 1006–1018.
- [15] W. J. H. Borghols, M. Wagemaker, U. Lafont, E. M. Kelder, F. M. Mulder, *J. Am. Chem. Soc.* **2009**, *131*, 17786–17792.
- [16] T. Ohzuku, A. Ueda, N. Yamamoto, *J. Electrochem. Soc.* **1995**, *142*, 1431–1435.
- [17] K. Naoi, S. Ishimoto, Y. Isobe, S. Aoyagi, *J. Power Sources* **2010**, *195*, 6250–6254.
- [18] C. H. Chen, J. T. Vaughey, A. N. Jansen, D. W. Dees, A. J. Kahaian, T. Goacher, M. M. Thackeray, *J. Electrochem. Soc.* **2001**, *148*, A102–A104.
- [19] S. Scharner, W. Weppner, P. Schmid-Beurmann, *J. Electrochem. Soc.* **1999**, *146*, 857–861.
- [20] M. S. Song, A. Benayad, Y. M. Choi, K. S. Park, *Chem. Commun.* **2012**, *48*, 516–518.
- [21] C. Kim, Y.-S. Yu, B. Moyon, C. Sirisopanaporn, T. J. Richardson, J. Cabana, *J. Phys. Chem. C* **2016**, *120*, 29030–29038.
- [22] E. Pohjalainen, J. Kallioinen, T. Kallio, *J. Power Sources* **2015**, *279*, 481–486.
- [23] C. Kim, N. S. Norberg, C. T. Alexander, R. Kostecki, J. Cabana, *Adv. Funct. Mater.* **2013**, *23*, 1214–1222.
- [24] C. T. Alexander, C. Kim, R. Yaylian, J. Cabana, *Energy Technol.* **2014**, *2*, 383–390.
- [25] D. Young, A. Ransil, R. Amin, Z. Li, Y.-M. Chiang, *Adv. Energy Mater.* **2013**, *3*, 1125–1129.
- [26] J. Wang, H. Zhao, Z. Li, Y. Wen, Q. Xia, Y. Zhang, G. Yushin, *Adv. Mater. Interfaces* **2016**, *3*, 1600003.
- [27] E. Zhao, C. Qin, H.-R. Jung, G. Berdichevsky, A. Nese, S. Marder, G. Yushin, *ACS Nano* **2016**, *10*, 3977–3984.
- [28] X. Jia, Y. Kan, X. Zhu, G. Ning, Y. Lu, F. Wei, *Nano Energy* **2014**, *10*, 344–352.
- [29] X. Meng, J. Liu, X. Li, M. N. Banis, J. Yang, R. Li, X. Sun, *RSC Adv.* **2013**, *3*, 7285–7288.
- [30] J. Shu, L. Hou, R. Ma, M. Shui, L. Shao, D. Wang, Y. Ren, W. Zheng, *RSC Adv.* **2012**, *2*, 10306–10309.
- [31] J.-H. Choi, W.-H. Ryu, K. Park, J.-D. Jo, S.-M. Jo, D.-S. Lim, I.-D. Kim, *Sci. Rep.* **2014**, *4*, 7334.
- [32] H. Ni, L.-Z. Fan, *J. Power Sources* **2012**, *214*, 195–199.
- [33] K. Naoi, *Fuel Cells* **2010**, *10*, 825–833.
- [34] K. Naoi, S. Ishimoto, J.-i. Miyamoto, W. Naoi, *Energy Environ. Sci.* **2012**, *5*, 9363–9373.
- [35] K. Naoi, W. Naoi, S. Aoyagi, J.-i. Miyamoto, T. Kamino, *Accounts Chem Res* **2013**, *46*, 1075–1083.
- [36] Y. Tang, Y. Zhang, X. Rui, D. Qi, Y. Luo, W. R. Leow, S. Chen, J. Guo, J. Wei, W. Li, J. Deng, Y. Lai, B. Ma, X. Chen, *Adv. Mater.* **2016**, *28*, 1567–1576.
- [37] H.-p. Liu, G.-w. Wen, S.-f. Bi, C.-y. Wang, J.-m. Hao, P. Gao, *Electrochim. Acta* **2016**, *192*, 38–44.
- [38] H.-Y. Dong, Y.-B. He, B. Li, C. Zhang, M. Liu, F. Su, W. Lv, F. Kang, Q.-H. Yang, *Electrochim. Acta* **2014**, *142*, 247–253.
- [39] J. Zhu, R. Duan, Y. Zhang, J. Zhu, *Ceram. Int.* **2016**, *42*, 334–340.
- [40] N. Xu, X. Sun, X. Zhang, K. Wang, Y. Ma, *RSC Adv.* **2015**, *5*, 94361–94368.
- [41] C. Lin, B. Ding, Y. Xin, F. Cheng, M. O. Lai, L. Lu, H. Zhou, *J. Power Sources* **2014**, *248*, 1034–1041.
- [42] W. Wang, B. Jiang, W. Xiong, Z. Wang, S. Jiao, *Electrochim. Acta* **2013**, *114*, 198–204.
- [43] H. Duan, J. Li, H. Du, S. W. Chiang, C. Xu, W. Duan, F. Kang, *J. Phys. Chem. C* **2015**, *119*, 5238–5245.
- [44] P. Reale, S. Panero, F. Ronci, V. Rossi Albertini, B. Scrosati, *Chem. Mater.* **2003**, *15*, 3437–3442.

- [45] C. Lin, G. Liang, J. Gao, S. Deng, S. Lin, J. Li, *Functional Materials Letters* **2015**, *09*, 1650012.
- [46] G.-H. Dong, H.-J. Liu, L. Zhou, L. Chong, J. Yang, Y.-M. Qiao, D.-H. Zhang, *J. Alloys Compd.* **2014**, *615*, 817–824.
- [47] S. Sharmila, B. Senthilkumar, V. D. Nithya, K. VEDIAPPAN, C. W. Lee, R. K. Selvan, *J. Phys. Chem. Solids* **2013**, *74*, 1515–1521.
- [48] J. S. Park, S.-H. Baek, Y. Park, J. H. Kim, *J. Korean Phys. Soc.* **2014**, *64*, 1545–1549.
- [49] M. Guo, S. Wang, L.-X. Ding, C. Huang, H. Wang, *J. Power Sources* **2015**, *283*, 372–380.
- [50] Z. Yu, X. Zhang, G. Yang, J. Liu, J. Wang, R. Wang, J. Zhang, *Electrochim. Acta* **2011**, *56*, 8611–8617.
- [51] A. F. Oriukas, K. Z. Fung, V. Venckutė, V. Kazlauskienė, J. Miškinis, M. Lelis, *Solid State Ionics* **2015**, *271*, 34–41.
- [52] Q. Zhang, H. Lu, H. Zhong, X. Yan, C. Ouyang, L. Zhang, *J. Mater. Chem. A* **2015**, *3*, 13706–13716.
- [53] T. Yuan, Z. Tan, C. Ma, J. Yang, Z.-F. Ma, S. Zheng, *Adv. Energy Mater.* **2017**, *7*, 1601625.
- [54] J.-Y. Shin, J. H. Joo, D. Samuelis, J. Maier, *Chem. Mater.* **2012**, *24*, 543–551.
- [55] J. Wolfenstine, U. Lee, J. L. Allen, *J. Power Sources* **2006**, *154*, 287–289.
- [56] J. Qiu, C. Lai, E. Gray, S. Li, S. Qiu, E. Strounina, C. Sun, H. Zhao, S. Zhang, *J. Mater. Chem. A* **2014**, *2*, 6353.
- [57] L. Shen, E. Uchaker, X. Zhang, G. Cao, *Adv. Mater.* **2012**, *24*, 6502–6506.
- [58] S. Nie, C. Li, H. Peng, G. Li, K. Chen, *RSC Adv.* **2015**, *5*, 23278–23282.
- [59] M. Widmaier, B. Krüner, N. Jäckel, M. Aslan, S. Fleischmann, C. Engel, V. Presser, *J. Electrochem. Soc.* **2016**, *163*, A2956–A2964.
- [60] D. Weingarth, M. Zeiger, N. Jäckel, M. Aslan, G. Feng, V. Presser, *Adv. Energy Mater.* **2014**, *4*, 1400316.
- [61] S. Brunauer, P. H. Emmett, E. Teller, *J. Am. Chem. Soc.* **1938**, *60*, 309–319.
- [62] M. Thommes, K. Kaneko, A. V. Neimark, J. P. Olivier, F. Rodriguez-Reinoso, J. Rouquerol, K. S. W. Sing, *Pure Appl. Chem.* **2015**, *87*, 1051–1069.
- [63] M. A. Henderson, *Surf. Sci.* **1998**, *400*, 203–219.
- [64] M. B. Hugenschmidt, L. Gamble, C. T. Campbell, *Surf. Sci.* **1994**, *302*, 329–340.
- [65] W. Meng, Y. Xu, B. Yan, J. Guo, *Ionics* **2017**, DOI:10.1007/s11581-017-2278-4.
- [66] G. Li, J. Li, G. Li, G. Jiang, *J. Mater. Chem. A* **2015**, *3*, 22073–22080.
- [67] X.-P. Wang, Y. Yu, X.-F. Hu, L. Gao, *Thin Solid Films* **2000**, *371*, 148–152.
- [68] D. G. Kellerman, N. A. Mukhina, N. A. Zhuravlev, M. S. Valova, V. S. Gorshkov, *Phys. Solid State* **2010**, *52*, 459–464.
- [69] C. Y. Ouyang, Z. Y. Zhong, M. S. Lei, *Electrochem. Commun.* **2007**, *9*, 1107–1112.
- [70] D. Liu, C. Ouyang, J. Shu, J. Jiang, Z. Wang, L. Chen, *physica status solidi b* **2006**, *243*, 1835–1841.
- [71] T. Kostlánová, J. Dědeček, P. Krtíl, *Electrochim. Acta* **2007**, *52*, 1847–1856.
- [72] H. Ge, H. Tian, H. Song, D. Liu, S. Wu, X. Shi, X. Gao, L. Lv, X.-M. Song, *Mater. Res. Bull.* **2015**, *61*, 459–462.
- [73] Y.-R. Jhan, J.-G. Duh, *Electrochim. Acta* **2012**, *63*, 9–15.
- [74] Y. Aiura, Y. Nishihara, Y. Haruyama, T. Komeda, S. Kodaira, Y. Sakisaka, T. Maruyama, H. Kato, *Physica B: Condensed Matter* **1994**, *194–196*, 1215–1216.
- [75] X. Chen, L. Liu, P. Y. Yu, S. S. Mao, *Science* **2011**, *331*, 746.
- [76] S.-T. Myung, M. Kikuchi, C. S. Yoon, H. Yashiro, S.-J. Kim, Y.-K. Sun, B. Scrosati, *Energ Environ Sci* **2013**, *6*, 2609–2614.
- [77] G. Izquierdo, A. R. West, *Mater. Res. Bull.* **1980**, *15*, 1655–1660.
- [78] J. F. Moulder, W. F. Stickle, P. E. Sobol, K. D. Bomben, *Handbook of X Ray Photoelectron Spectroscopy: A Reference Book of Standard Spectra for Identification and Interpretation of XPS Data* (Physical Electronics, Eden Prairie, **1995**).
- [79] C. Moreno-Castilla, M. V. López-Ramón, F. Carrasco-Marín, *Carbon* **2000**, *38*, 1995–2001.
- [80] U. Zielke, K. J. Hüttinger, W. P. Hoffman, *Carbon* **1996**, *34*, 983–998.
- [81] Z. R. Yue, W. Jiang, L. Wang, S. D. Gardner, C. U. Pittman Jr, *Carbon* **1999**, *37*, 1785–1796.
- [82] U. Diebold, *Surf. Sci. Rep.* **2003**, *48*, 53–229.
- [83] R. L. Kurtz, R. Stock-Bauer, T. E. Msdey, E. Román, J. De Segovia, *Surf. Sci.* **1989**, *218*, 178–200.
- [84] A. L. Linsebigler, G. Lu, J. T. Yates, *Chem. Rev.* **1995**, *95*, 735–758.
- [85] W. Göpel, J. A. Anderson, D. Frankel, M. Jaehnig, K. Phillips, J. A. Schäfer, G. Rocker, *Surf. Sci.* **1984**, *139*, 333–346.
- [86] P. V. Braun, J. Cho, J. H. Pikul, W. P. King, H. Zhang, *Curr. Opin. Solid State Mater. Sci.* **2012**, *16*, 186–198.
- [87] D. He, N. N. Ekere, *J. Phys. D* **2004**, *37*, 1848.
- [88] G. Liu, H. Zheng, A. S. Simens, A. M. Minor, X. Song, V. S. Battaglia, *J. Electrochem. Soc.* **2007**, *154*, A1129–A1134.
- [89] R. Dominko, M. Gaberšček, J. Drofenik, M. Bele, J. Jamnik, *Electrochim. Acta* **2003**, *48*, 3709–3716.
- [90] R. Dominko, M. Gaberšček, J. Drofenik, M. Bele, S. Pejovnik, *Electrochim. Solid-State Lett.* **2001**, *4*, A187–A190.
- [91] A. Tolosa, M. Widmaier, B. Krüner, J. M. Griffin, V. Presser, *Sustainable Energy & Fuels* **2018**, *2*, 215–228.
- [92] X. Lu, L. Zhao, X. He, R. Xiao, L. Gu, Y.-S. Hu, H. Li, Z. Wang, X. Duan, L. Chen, J. Maier, Y. Ikuhara, *Adv. Mater.* **2012**, *24*, 3233–3238.
- [93] C. Liu, Z. G. Neale, G. Cao, *Mater. Today* **2016**, *19*, 109–123.
- [94] H. Ge, N. Li, D. Li, C. Dai, D. Wang, *Electrochem. Commun.* **2008**, *10*, 719–722.
- [95] X. L. Yao, S. Xie, H. Q. Nian, C. H. Chen, *J. Alloys Compd.* **2008**, *465*, 375–379.
- [96] D. Ahn, X. Xiao, *Electrochem. Commun.* **2011**, *13*, 796–799.
- [97] Y. Wang, A. Zhou, X. Dai, L. Feng, J. Li, J. Li, *J. Power Sources* **2014**, *266*, 114–120.
- [98] H. Song, T.-G. Jeong, Y. H. Moon, H.-H. Chun, K. Y. Chung, H. S. Kim, B. W. Cho, Y.-T. Kim, *Sci. Rep.* **2014**, *4*, 4350.
- [99] S. Dong, X. Wang, L. Shen, H. Li, J. Wang, P. Nie, J. Wang, X. Zhang, *J. Electroanal. Chem.* **2015**, *757*, 1–7.
- [100] R. K. B. Gover, J. R. Tolchard, H. Tukamoto, T. Murai, J. T. S. Irvine, *J. Electrochem. Soc.* **1999**, *146*, 4348–4353.
- [101] I. Tsuyumoto, T. Moriguchi, *Mater. Res. Bull.* **2015**, *70*, 748–752.
- [102] W. Zhu, H. Yang, W. Zhang, H. Huang, X. Tao, Y. Xia, Y. Gan, X. Guo, *RSC Adv.* **2015**, *5*, 74774–74782.
- [103] Y.-Q. Wang, L. Gu, Y.-G. Guo, H. Li, X.-Q. He, S. Tsukimoto, Y. Ikuhara, L.-J. Wan, *J. Am. Chem. Soc.* **2012**, *134*, 7874–7879.
- [104] G. Vitiņš, G. Ķizāne, A. Lūsis, J. Tiliks, *J. Solid State Electrochem.* **2002**, *6*, 311–319.
- [105] M. Vijayakumar, S. Kerisit, Z. Yang, G. L. Graff, J. Liu, J. A. Sears, S. D. Burton, K. M. Rosso, J. Hu, *J. Phys. Chem. C* **2009**, *113*, 20108–20116.
- [106] T. Zhang, B. Fuchs, M. Secchiarioli, M. Wohlfahrt-Mehrens, S. Dsoke, *Electrochim. Acta* **2016**, *218*, 163–173.
- [107] H.-G. Jung, S.-T. Myung, C. S. Yoon, S.-B. Son, K. H. Oh, K. Amine, B. Scrosati, Y.-K. Sun, *Energ Environ Sci* **2011**, *4*, 1345–1351.
- [108] J. Kim, S.-W. Kim, H. Gwon, W.-S. Yoon, K. Kang, *Electrochim. Acta* **2009**, *54*, 5914–5918.
- [109] C. C. Li, Q. H. Li, L. B. Chen, T. H. Wang, *ACS Appl. Mater. Interfaces* **2012**, *4*, 1233–1238.
- [110] D. H. Long, M.-G. Jeong, Y.-S. Lee, W. Choi, J. K. Lee, I.-H. Oh, H.-G. Jung, *ACS Appl. Mater. Interfaces* **2015**, *7*, 10250–10257.
- [111] L. Shen, H. Li, E. Uchaker, X. Zhang, G. Cao, *Nano Lett.* **2012**, *12*, 5673–5678.
- [112] L. Shen, C. Yuan, H. Luo, X. Zhang, S. Yang, X. Lu, *Nanoscale* **2011**, *3*, 572–574.
- [113] L. Yu, H. B. Wu, X. W. Lou, *Adv. Mater.* **2013**, *25*, 2296–2300.
- [114] S. Dsoke, B. Fuchs, E. Gucciardi, M. Wohlfahrt-Mehrens, *J. Power Sources* **2015**, *282*, 385–393.
- [115] S. Fleischmann, M. Zeiger, N. Jäckel, B. Krüner, V. Lemkova, M. Widmaier, V. Presser, *J. Mater. Chem. A* **2017**, *5*, 13039–1351.
- [116] J. Lee, A. Tolosa, B. Krüner, N. Jäckel, S. Fleischmann, M. Zeiger, D. Kim, V. Presser, *Sustainable Energy & Fuels* **2017**, *1*, 299–307.
- [117] A. Tolosa, B. Krüner, S. Fleischmann, N. Jäckel, M. Zeiger, M. Aslan, I. Grobelsek, V. Presser, *J. Mater. Chem. A* **2016**, *4*, 16003–16016.
- [118] F. X. Wang, S. Y. Xiao, Y. S. Zhu, Z. Chang, C. L. Hu, Y. P. Wu, R. Holze, *J. Power Sources* **2014**, *246*, 19–23.

Manuscript received: December 25, 2017
Accepted article published: January 30, 2018
Version of record online: ■ ■ ■

ARTICLES



Tuning in: Oxygen vacancies form in $\text{Li}_4\text{Ti}_5\text{O}_{12}$ at temperatures above 450 °C under hydrogen atmosphere. These defects increase the electrical conductivity and result in a color change of $\text{Li}_4\text{Ti}_5\text{O}_{12}$. We identified an optimum treatment temperature at 800 °C, which results in high conductivity,

without $\text{Li}_4\text{Ti}_5\text{O}_{12}$ particle growth. Modified $\text{Li}_4\text{Ti}_5\text{O}_{12}$ results in high performance (70 mAh/g at 100C) at low electrode carbon content and we demonstrated superior behavior of oxygen deficient $\text{Li}_4\text{Ti}_5\text{O}_{12}$ in a full-cell setup (70 Wh/kg, 47 kW/kg).

M. Widmaier, K. Pfeifer, Dr. L. Bommer, Prof. V. Presser*

1 – 17

Valence-Tuned Lithium Titanate Nanopowder for High-Rate Electrochemical Energy Storage



Valence-tuned lithium titanate nanopowder for high-rate electrochemical energy storage

Mathias Widmaier^{1,2}, Kristina Pfeifer^{1,3}, Lars Bommer¹, and Volker Presser^{2,4,*}

¹ Robert Bosch GmbH, Robert-Bosch-Campus 1, 71272 Renningen, Germany

² Department of Materials Science and Engineering, Saarland University, Campus D2 2, 66123 Saarbrücken, Germany

³ Chemisches Institut, Eberhard Karls Universität Tübingen, Auf der Morgenstelle 18, 72076 Tübingen, Germany

⁴ INM – Leibniz Institute for New Materials, Campus D2 2, 66123 Saarbrücken, Germany

* Corresponding author's email: volker.presser@leibniz-inm.de

Supporting Information

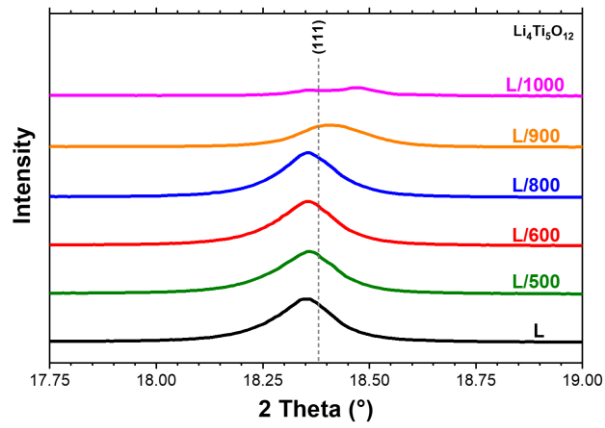


Fig. S1: Magnification of the X-ray diffraction pattern of the (111) diffraction peak of spinel $\text{Li}_4\text{Ti}_5\text{O}_{12}$.

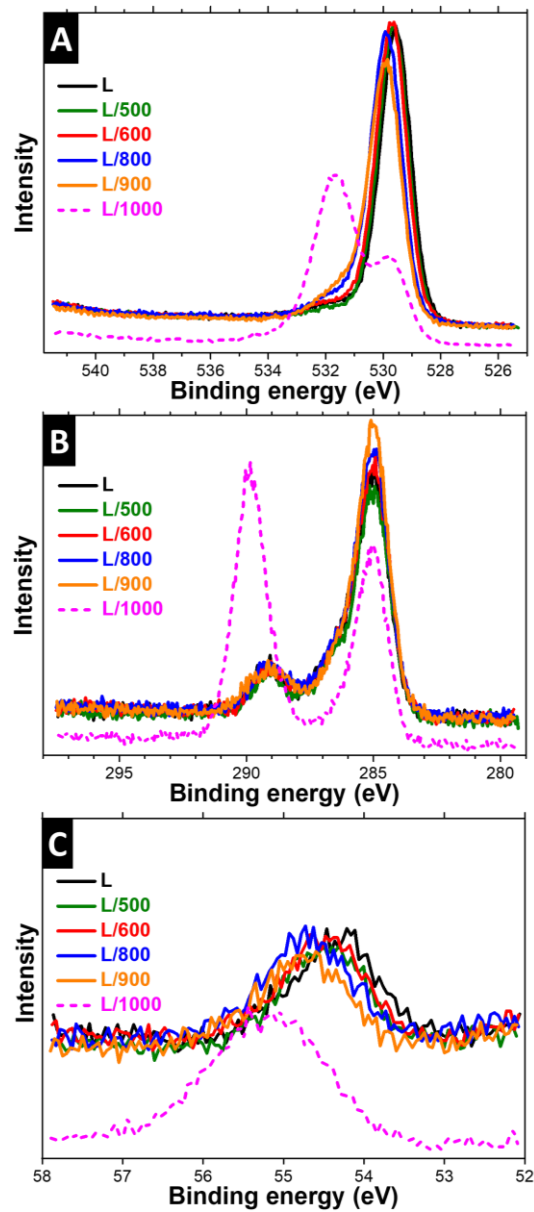


Fig. S2: Material characterization of pristine LTO and LTO powder heated to different temperatures under hydrogen atmosphere. O1s (A), C1s (B) and Li1s (C) high-resolution X-ray photoelectron spectra.

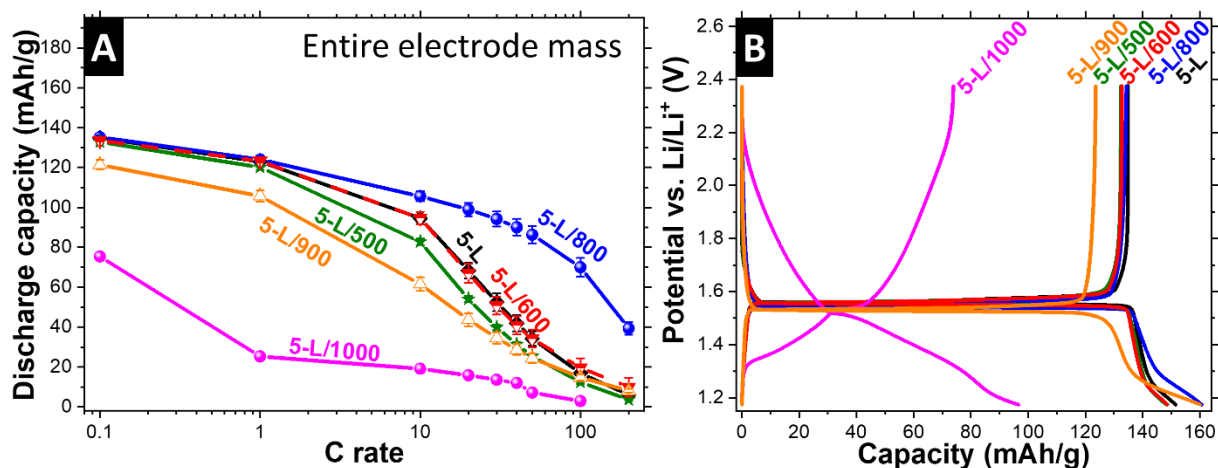


Fig. S3: Rate performance based on electrode mass (A) and galvanostatic charge and discharge curves of the 3rd cycle measured at 0.1 C of electrodes comprising 5 mass% carbon.

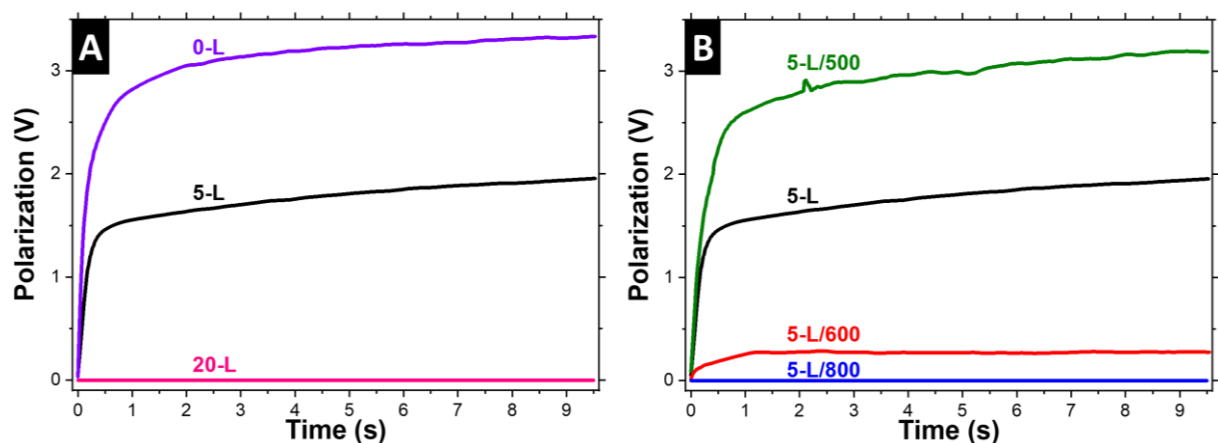


Fig. S4: Voltage development for electrodes sandwiched between titanium pistons when applying a current of 0.001 mA.

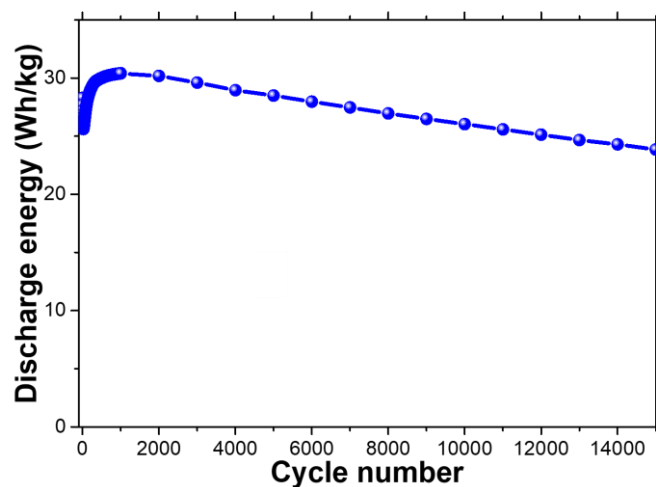


Fig. S5: Electrochemical cycling stability at charging/discharging rates of 100 C of full-cells employing 5-L/800 anodes and activated carbon/LMO composite cathodes normalized to the entire electrode mass.

5. Conclusions and Outlook

In this thesis, electrode hybridization was investigated to construct hybrid supercapacitors based on an optimized combination of commercial LIB and EDLC materials. Due to the large number of combination possibilities of electrolytes, active materials and mixing ratios thereof, pre-investigations were conducted to deduce the following cell design criterions:

- i) Highly conductive Li-salt containing ACN as the electrolyte.
- ii) AC as EDLC active material.
- iii) Nano-sized LTO as anode LIB material to avoid SEI formation and enable the use of ACN as the electrolyte.
- iv) Micrometer-sized LMO as cathode material due to its high safety and good compatibility with an ACN electrolyte.

From a cell design point of view, Li-salt containing ACN is irreplaceable due to its unmatched high ionic conductivity and electrochemical stability. The lacking stability of conventional Li-metal reference electrodes in ACN, however, severely aggravates fundamental and quantitative investigations of the individual electrode behavior. Based on this issue, a comprehensive study of (modified) carbons was carried out to establish this QRE as a stable quasi-reference electrode for unconventional Li-salt containing electrolytes. In this study, several key findings were deduced to serve as a guideline for the selection and limitations of different carbon materials as QRE:

- i) High surface area carbon-based QREs are generally more stable than low surface area carbon QREs.
- ii) Carbon pore size distribution, electrolyte solvent, and binder have only negligible influence the stability of the QRE.
- iii) The stability of the QRE is highly affected by the salt employed and decreases in the following order $\text{LiTFSI} > \text{LiClO}_4 > \text{LiPF}_6 > \text{LiBF}_4$.
- iv) The potential drift of common carbons is drastically suppressed if the surface area of AC is saturated by oxygen and nitrogen functional groups. After 15 days, the potential of heavily functionalized AC only marginally drifts by 10 mV.

Functionalized AC was used as QRE for all follow-up experiments and, for the first time, enabled accurate long-term characterization of individual HSC electrodes in Li-salt containing ACN electrolyte. With this QRE, the rate performance of AC/LTO and AC/LMO composite electrodes was investigated. AC/LMO cathodes were found to be limited by Li-ion diffusion in the micrometer-sized LMO particles and require a high AC content to enable high rate operation. By contrast, the rate capability of AC/LTO electrodes was not impaired by charge storage in the nano-sized LTO particles and anodes with high LTO content were identified to be an effective approach to enhance the specific energy of HSCs. Increasing the LTO content does drastically change the electrode microstructure and, unexpectedly, also the electrochemical stability as was outlined in a second publication. The corresponding key conclusions and findings are:

- i) The electrode microstructure and electrical percolation of LTO based anodes have a considerable impact on the electrochemical stability window.
- ii) At low LTO concentration, the electrochemical stability of composite electrodes is constantly improving when increasing LTO concentration.
- iii) At high LTO concentration (72 mass%) the electrolyte decomposes unexpectedly within the electrochemical boundaries of the single materials due to poor electrical percolation.
- iv) The electrical percolation can be reestablished via exchanging a fraction of AC and carbon black. This improves the cycle life from 10 to 36,000 cycles at high LTO concentration.

Thus, very high LTO concentrations severely deteriorate the electrochemical performance of the cells due to the low electrical conductivity of LTO in the de-lithiated phase. The most obvious approach to compensate this rate limitation is adding high amounts of conductive carbon into the electrode. This comes at the expense of a decreased overall electrode capacity since the conductive carbon is electrochemically inactive in the voltage range of LTO. Therefore, increasing the intrinsic electronic conductivity of LTO via modification of the oxygen defect concentration is the best solution as has been shown in the final study.

In the final publication, it was demonstrated that:

- i) Oxygen vacancies are formed in LTO at temperatures above 450 °C in a hydrogen atmosphere.
- ii) The concentration of oxygen vacancies, Ti^{3+}/Ti^{4+} ratio and associated electrical conductivity increase with rising treatment temperature.
- iii) Treatment at 800 °C under hydrogen drastically increases the electrical conductivity, while circumventing undesired LTO phase transformation, amorphization, and particle growth.

The associated increase of the intrinsic electrical conductivity of oxygen deficient LTO allowed operating LTO electrodes at C-rates above 50 C with a minimal carbon concentration of 5 mass%. Such electrodes are highly competitive to elaborate state-of-the-art LTO-carbon nanocomposites and can deliver a high electrode capacity of about 70 mAh/g (82 mAh/g when normalized to the active mass) at ultra-high rates of 100 C. The performance of pristine LTO electrodes is impaired by the low electronic conductivity of the Li-poor LTO phase, and large amounts of electrochemically inactive conductive carbon are needed (20 mass%). The superior performance of hydrogen-treated LTO was further demonstrated in a HSC full-cell setup against an activated carbon / lithium manganese oxide composite electrode. This device is characterized by outstanding energy and power ratings of 70 Wh/kg and 47 kW/kg (82 Wh/kg and 55 kW/kg normalized to the active mass) and high electrochemical cycling stability over 5,000 charge-discharge cycles (78 % after 15,000 cycles at 100 C). Accordingly, the specific energy and power were dramatically raised throughout this work by 70 % and 60 % as compared to prior state-of-the-art (**Figure 13**).

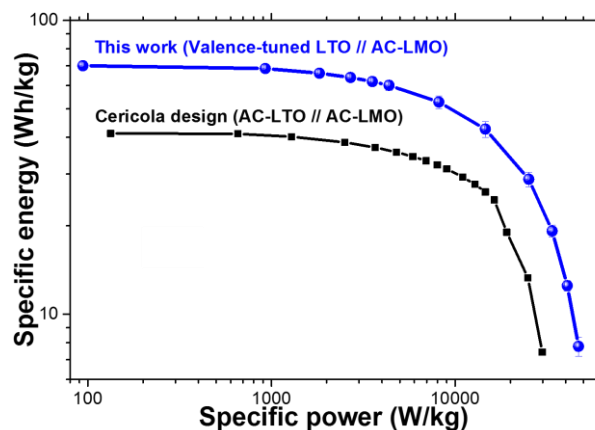


Figure 13: Ragone-chart of HSC full-cells comparing prior state-of-the-art based on Cericola's cell-design [19] with cells developed in this work.

HSC cells were successfully developed which are highly competitive with advanced state-of-the-art nanocomposites. As opposed to the latter, the developed cells solely employ cost-effective commercial materials in a highly optimized, synergetic combination. To further push this promising cell-concept to its electrochemical limits, follow-up work should investigate cathode composition and the cathode LIB material. Particularly the origin of the incompatibilities of cathode materials, like LFP, with the ACN electrolyte needs to be clarified since this material is reported to be well-suited for nanosizing. Composite electrodes employing nanoparticulate LFP could enable higher contents of LIB material, without impairing the electrochemical kinetics. Moreover, capacity fading mechanism of LMO in ACN electrolyte could be inherently different to the conventional carbonates and should further be investigated.

References

- [1] B. Scrosati, J. Garche, *Journal of Power Sources* 195 (2010) 2419–2430.
- [2] J.B. Goodenough, K.-S. Park, *Journal of the American Chemical Society* 135 (2013) 1167–1176.
- [3] R. Korthauer, *Handbuch Lithium-Ionen-Batterien*, Springer Berlin Heidelberg, Berlin, Heidelberg, 2013.
- [4] P. Kurzweil, M. Chwistek, *Journal of Power Sources* 176 (2008) 555–567.
- [5] F. Béguin, E. Frąckowiak, *Supercapacitors: Materials, systems, and applications*, Wiley-VCH, Weinheim, 2013.
- [6] A.G. Pandolfo, A.F. Hollenkamp, *Journal of Power Sources* 157 (2006) 11–27.
- [7] D.V. Ragone, in: *SAE International 400 Commonwealth Drive, Warrendale, PA, United States*, 1968.
- [8] J.R. Miller, J. Burgel, H. Catherino, F. Krestik, J. Monroe, J.R. Stafford, in: *SAE International 400 Commonwealth Drive, Warrendale, PA, United States*, 1998.
- [9] J.R. Miller, S.M. Butler, in: *SAE International 400 Commonwealth Drive, Warrendale, PA, United States*, 2001.
- [10] H.A. Catherino, J.F. Burgel, P.L. Shi, A. Rusek, X. Zou, *Journal of Power Sources* 162 (2006) 965–970.
- [11] C.E. Holland, J.W. Weidner, R.A. Dougal, R.E. White, *Journal of Power Sources* 109 (2002) 32–37.
- [12] D. Cericola, R. Kötz, *Electrochimica Acta* 72 (2012) 1–17.
- [13] G.G. Amatucci, F. Badway, A. Du Pasquier, T. Zheng, *J. Electrochem. Soc.* 148 (2001) A930.
- [14] N. Böckenfeld, R.-S. Kühnel, S. Passerini, M. Winter, A. Balducci, *Journal of Power Sources* 196 (2011) 4136–4142.
- [15] N. Böckenfeld, T. Placke, M. Winter, S. Passerini, A. Balducci, *Electrochimica Acta* 76 (2012) 130–136.
- [16] D. Cericola, P. Novák, A. Wokaun, R. Kötz, *Electrochimica Acta* 56 (2011) 8403–8411.
- [17] D. Cericola, P.W. Ruch, R. Kötz, P. Novák, A. Wokaun, *Electrochemistry Communications* 12 (2010) 812–815.
- [18] D. Cericola, P. Novák, A. Wokaun, R. Kötz, *Electrochimica Acta* 56 (2011) 1288–1293.
- [19] D. Cericola, P. Novák, A. Wokaun, R. Kötz, *Journal of Power Sources* 196 (2011) 10305–10313.
- [20] B. Wang, Q. Wang, B. Xu, T. Liu, D. Wang, G. Zhao, *RSC Adv.* 3 (2013) 20024.
- [21] M. Secchiarioli, R. Marassi, M. Wohlfahrt-Mehrens, S. Dsoke, *Electrochimica Acta* 219 (2016) 425–434.
- [22] M. Widmaier, N. Jäckel, M. Zeiger, M. Abuzarli, C. Engel, L. Bommer, V. Presser, *Electrochimica Acta* 247 (2017) 1006–1018.
- [23] X. Li, B. Wei, *Nano Energy* 2 (2013) 159–173.
- [24] *Elektrochemische Speicher: Superkondensatoren, Batterien, Elektrolyse-Wasserstoff, Rechtliche Grundlagen*, 1 Aufl., Springer Vieweg, [s.l.], 2016.
- [25] A. Burke, M. Miller, H. Zhao, *Electric Vehicle Symposium* 3 (2012) 2213–2220.
- [26] M. Broussely, P. Biensan, B. Simon, *Electrochimica Acta* 45 (1999) 3–22.
- [27] M.B. Armand, in: D.W. Murphy, J. Broadhead, B.C.H. Steele (Eds.), *Materials for Advanced Batteries*, Springer US, Boston, MA, 1980, pp. 145–161.
- [28] K. Mizushima, P.C. Jones, P.J. Wiseman, J.B. Goodenough, *Materials Research Bulletin* 15 (1980) 783–789.
- [29] M. Lazzari, *J. Electrochem. Soc.* 127 (1980) 773.
- [30] A.J. Bard, L.R. Faulkner, *Electrochemical methods: Fundamentals and applications* / Allen J. Bard, Larry R. Faulkner, 2nd ed., John Wiley, New York, Chichester, 2001.
- [31] D. Linden, T.B. Reddy, *Handbook of batteries*, 3rd ed. / Thomas B. Reddy, editor, McGraw-Hill, New York, London, 2002.
- [32] N. Omar, M. Daowd, P. van den Bossche, O. Hegazy, J. Smekens, T. Coosemans, J. van Mierlo, *Energies* 5 (2012) 2952–2988.
- [33] B. Xu, D. Qian, Z. Wang, Y.S. Meng, *Materials Science and Engineering: R: Reports* 73 (2012) 51–65.

- [34] J. MOLEND, J. MARZEC, *Funct. Mater. Lett.* 02 (2009) 1–7.
- [35] S. Patoux, L. Daniel, C. Bourbon, H. Lignier, C. Pagano, F. Le Cras, S. Jouanneau, S. Martinet, *Journal of Power Sources* 189 (2009) 344–352.
- [36] A.K. Padhi, *J. Electrochem. Soc.* 144 (1997) 1188.
- [37] N. Ravet, Y. Chouinard, J.F. Magnan, S. Besner, M. Gauthier, M. Armand, *Journal of Power Sources* 97-98 (2001) 503–507.
- [38] M.M. Thackeray, W.I.F. David, P.G. Bruce, J.B. Goodenough, *Materials Research Bulletin* 18 (1983) 461–472.
- [39] J.W. Fergus, *Journal of Power Sources* 195 (2010) 939–954.
- [40] X. Hu, Y. Huai, Z. Lin, J. Suo, Z. Deng, *J. Electrochem. Soc.* 154 (2007) A1026.
- [41] J.M. Tarascon, D. Guyomard, *Electrochimica Acta* 38 (1993) 1221–1231.
- [42] M.M. Thackeray, *Electrochem. Solid-State Lett.* 1 (1999) 7.
- [43] R. Benedek, M.M. Thackeray, *Electrochem. Solid-State Lett.* 9 (2006) A265.
- [44] D. Aurbach, B. Markovsky, G. Salitra, E. Markevich, Y. Talyossef, M. Koltypin, L. Nazar, B. Ellis, D. Kovacheva, *Journal of Power Sources* 165 (2007) 491–499.
- [45] J. TARASCON, D. Guyomard, *Solid State Ionics* 69 (1994) 293–305.
- [46] K.M. Abraham, *Electrochimica Acta* 38 (1993) 1233–1248.
- [47] T. Ohzuku, *J. Electrochem. Soc.* 142 (1995) 1431.
- [48] P. Verma, P. Maire, P. Novák, *Electrochimica Acta* 55 (2010) 6332–6341.
- [49] K. Xu, *Chemical reviews* 114 (2014) 11503–11618.
- [50] S.S. Zhang, *Journal of Power Sources* 162 (2006) 1379–1394.
- [51] Q. Wang, S.M. Zakeeruddin, I. Exnar, M. Grätzel, *J. Electrochem. Soc.* 151 (2004) A1598.
- [52] W.J.H. Borghols, M. Wagemaker, U. Lafont, E.M. Kelder, F.M. Mulder, *Journal of the American Chemical Society* 131 (2009) 17786–17792.
- [53] K. Naoi, S. Ishimoto, Y. Isobe, S. Aoyagi, *Journal of Power Sources* 195 (2010) 6250–6254.
- [54] K. Zaghib, M. Simoneau, M. Armand, M. Gauthier, *Journal of Power Sources* 81-82 (1999) 300–305.
- [55] S. Scharner, *J. Electrochem. Soc.* 146 (1999) 857.
- [56] X. Lu, L. Zhao, X. He, R. Xiao, L. Gu, Y.-S. Hu, H. Li, Z. Wang, X. Duan, L. Chen, J. Maier, Y. Ikuhara, *Advanced materials (Deerfield Beach, Fla.)* 24 (2012) 3233–3238.
- [57] N. Takami, H. Inagaki, T. Kishi, Y. Harada, Y. Fujita, K. Hoshina, *J. Electrochem. Soc.* 156 (2009) A128.
- [58] C.H. Chen, J.T. Vaughey, A.N. Jansen, D.W. Dees, A.J. Kahaian, T. Goacher, M.M. Thackeray, *J. Electrochem. Soc.* 148 (2001) A102.
- [59] E. Zhao, C. Qin, H.-R. Jung, G. Berdichevsky, A. Nese, S. Marder, G. Yushin, *ACS nano* 10 (2016) 3977–3984.
- [60] X. Jia, Y. Kan, X. Zhu, G. Ning, Y. Lu, F. Wei, *Nano Energy* 10 (2014) 344–352.
- [61] X. Meng, J. Liu, X. Li, M.N. Banis, J. Yang, R. Li, X. Sun, *RSC Adv.* 3 (2013) 7285.
- [62] J. Shu, L. Hou, R. Ma, M. Shui, L. Shao, D. Wang, Y. Ren, W. Zheng, *RSC Adv.* 2 (2012) 10306.
- [63] J.-H. Choi, W.-H. Ryu, K. Park, J.-D. Jo, S.-M. Jo, D.-S. Lim, I.-D. Kim, *Scientific reports* 4 (2014) 7334.
- [64] H. Ni, L.-Z. Fan, *Journal of Power Sources* 214 (2012) 195–199.
- [65] K. Naoi, *Fuel Cells* 10 (2010) 825–833.
- [66] K. Naoi, S. Ishimoto, J.-i. Miyamoto, W. Naoi, *Energy Environ. Sci.* 5 (2012) 9363.
- [67] K. Naoi, W. Naoi, S. Aoyagi, J.-i. Miyamoto, T. Kamino, *Accounts of chemical research* 46 (2013) 1075–1083.
- [68] Y. Tang, Y. Zhang, X. Rui, D. Qi, Y. Luo, W.R. Leow, S. Chen, J. Guo, J. Wei, W. Li, J. Deng, Y. Lai, B. Ma, X. Chen, *Advanced materials (Deerfield Beach, Fla.)* 28 (2016) 1567–1576.
- [69] H.-p. Liu, G.-w. Wen, S.-f. Bi, C.-y. Wang, J.-m. Hao, P. Gao, *Electrochimica Acta* 192 (2016) 38–44.
- [70] H.-Y. Dong, Y.-B. He, B. Li, C. Zhang, M. Liu, F. Su, W. Lv, F. Kang, Q.-H. Yang, *Electrochimica Acta* 142 (2014) 247–253.
- [71] J. Zhu, R. Duan, Y. Zhang, J. Zhu, *Ceramics International* 42 (2016) 334–340.

- [72]N. Xu, X. Sun, X. Zhang, K. Wang, Y. Ma, RSC Adv. 5 (2015) 94361–94368.
- [73]C. Lin, B. Ding, Y. Xin, F. Cheng, M.O. Lai, L. Lu, H. Zhou, Journal of Power Sources 248 (2014) 1034–1041.
- [74]W. Wang, B. Jiang, W. Xiong, Z. Wang, S. Jiao, Electrochimica Acta 114 (2013) 198–204.
- [75]H. Duan, J. Li, H. Du, S.W. Chiang, C. Xu, W. Duan, F. Kang, J. Phys. Chem. C 119 (2015) 5238–5245.
- [76]P. Reale, S. Panero, F. Ronci, V. Rossi Albertini, B. Scrosati, Chem. Mater. 15 (2003) 3437–3442.
- [77]C. Lin, G. Liang, J. Gao, S. Deng, S. Lin, J. Li, Funct. Mater. Lett. 09 (2016) 1650012.
- [78]G.-H. Dong, H.-J. Liu, L. Zhou, L. Chong, J. Yang, Y.-M. Qiao, D.-H. Zhang, Journal of Alloys and Compounds 615 (2014) 817–824.
- [79]S. Sharmila, B. Senthilkumar, V.D. Nithya, K. Vediappan, C.W. Lee, R.K. Selvan, Journal of Physics and Chemistry of Solids 74 (2013) 1515–1521.
- [80]J.S. Park, S.-H. Baek, Y. Park, J.H. Kim, Journal of the Korean Physical Society 64 (2014) 1545–1549.
- [81]M. Guo, S. Wang, L.-X. Ding, C. Huang, H. Wang, Journal of Power Sources 283 (2015) 372–380.
- [82]Z. Yu, X. Zhang, G. Yang, J. Liu, J. Wang, R. Wang, J. Zhang, Electrochimica Acta 56 (2011) 8611–8617.
- [83]A.F. Orliukas, K.-Z. Fung, V. Venckutė, V. Kazlauskienė, J. Miškinis, M. Lelis, Solid State Ionics 271 (2015) 34–41.
- [84]Q. Zhang, H. Lu, H. Zhong, X. Yan, C. Ouyang, L. Zhang, J. Mater. Chem. A 3 (2015) 13706–13716.
- [85]T. Yuan, Z. Tan, C. Ma, J. Yang, Z.-F. Ma, S. Zheng, Adv. Energy Mater. 9-10 (2017) 1601625.
- [86]M. He, E. Castel, A. Laumann, G. Nuspl, P. Novak, E.J. Berg, Journal of the Electrochemical Society 162 (2015) A870-A876.
- [87]I. Belharouak, G.M. Koenig, T. Tan, H. Yumoto, N. Ota, K. Amine, Journal of the Electrochemical Society 159 (2012) A1165-A1170.
- [88]Y.-B. He, B. Li, M. Liu, C. Zhang, W. Lv, C. Yang, J. Li, H. Du, B. Zhang, Q.-H. Yang, J.-K. Kim, F. Kang, Scientific reports 2 (2012) 913.
- [89]K. Wu, J. Yang, Y. Zhang, C. Wang, D. Wang, J Appl Electrochem 42 (2012) 989–995.
- [90]K. Wu, J. Yang, Y. Liu, Y. Zhang, C. Wang, J. Xu, F. Ning, D. Wang, Journal of Power Sources 237 (2013) 285–290.
- [91]F. Béguin, V. Presser, A. Balducci, E. Frackowiak, Advanced materials (Deerfield Beach, Fla.) 26 (2014) 2219-51, 2283.
- [92]A.K. Shukla, A. Banerjee, M.K. Ravikumar, A. Jalajakshi, Electrochimica Acta 84 (2012) 165–173.
- [93]L.L. Zhang, X.S. Zhao, Chemical Society reviews 38 (2009) 2520–2531.
- [94]B.E. Conway, Electrochemical supercapacitors: Scientific fundamentals and technological applications / B.E. Conway, Kluwer Academic/Plenum, New York, London, 1999.
- [95]D. Qu, H. Shi, Journal of Power Sources 74 (1998) 99–107.
- [96]J. Gamby, P.L. Taberna, P. Simon, J.F. Fauvarque, M. Chesneau, Journal of Power Sources 101 (2001) 109–116.
- [97]M. Zeiger, N. Jäckel, V.N. Mochalin, V. Presser, J. Mater. Chem. A 4 (2016) 3172–3196.
- [98]A.B. Fuertes, G. Lota, T.A. Centeno, E. Frackowiak, Electrochimica Acta 50 (2005) 2799–2805.
- [99]D.N. Futaba, K. Hata, T. Yamada, T. Hiraoka, Y. Hayamizu, Y. Kakudate, O. Tanaike, H. Hatori, M. Yumura, S. Iijima, Nature materials 5 (2006) 987–994.
- [100]H. Pröbstle, M. Wiener, J. Fricke, Journal of Porous Materials 10 (2003) 213–222.
- [101]H.-J. Choi, S.-M. Jung, J.-M. Seo, D.W. Chang, L. Dai, J.-B. Baek, Nano Energy 1 (2012) 534–551.
- [102]A. González, E. Goikolea, J.A. Barrena, R. Mysyk, Renewable and Sustainable Energy Reviews 58 (2016) 1189–1206.
- [103]K. Fic, G. Lota, M. Meller, E. Frackowiak, Energy Environ. Sci. 5 (2012) 5842–5850.
- [104]J.R. Miller, P. Simon, Science (New York, N.Y.) 321 (2008) 651–652.
- [105]C. Zhong, Y. Deng, W. Hu, J. Qiao, L. Zhang, J. Zhang, Chemical Society reviews 44 (2015) 7484–7539.

- [106]T. Brousse, D. Belanger, J.W. Long, *Journal of the Electrochemical Society* 162 (2015) A5185-A5189.
- [107]F. Béguin, *Supercapacitors* (2013).
- [108]E. Frackowiak, G. Lota, J. Machnikowski, C. Vix-Guterl, F. Béguin, *Electrochimica Acta* 51 (2006) 2209–2214.
- [109]E. Frackowiak, K. Fic, M. Meller, G. Lota, *ChemSusChem* 5 (2012) 1181–1185.
- [110]S.R. Sivakkumar, A.G. Pandolfo, *Electrochimica Acta* 65 (2012) 280–287.
- [111]P. Jeżowski, O. Crosnier, E. Deunf, P. Poizot, F. Béguin, T. Brousse, *Nature materials* 17 (2018) 167–173.
- [112]S. Fleischmann, M. Zeiger, N. Jäckel, B. Krüner, V. Lemkova, M. Widmaier, V. Presser, *J. Mater. Chem. A* 5 (2017) 13039–13051.
- [113]M. Zeiger, S. Fleischmann, B. Krüner, A. Tolosa, S. Bechtel, M. Baltes, A. Schreiber, R. Moroni, S. Vierrath, S. Thiele, V. Presser, *RSC Adv.* 6 (2016) 107163–107179.
- [114]S. Boukhalfa, K. Evanoff, G. Yushin, *Energy Environ. Sci.* 5 (2012) 6872.
- [115]S. Fleischmann, N. Jäckel, M. Zeiger, B. Krüner, I. Grobelsek, P. Formanek, S. Choudhury, D. Weingarth, V. Presser, *Chem. Mater.* 28 (2016) 2802–2813.
- [116]I.-H. Kim, J.-H. Kim, B.-W. Cho, Y.-H. Lee, K.-B. Kim, *J. Electrochem. Soc.* 153 (2006) A989.
- [117]M.-H. Bai, T.-Y. Liu, F. Luan, Y. Li, X.-X. Liu, *J. Mater. Chem. A* 2 (2014) 10882–10888.
- [118]M. Zeiger, D. Weingarth, V. Presser, *CHEMELECTROCHEM* 2 (2015) 1117–1127.
- [119]J. Huang, B.G. Sumpter, V. Meunier, G. Yushin, C. Portet, Y. Gogotsi, *J. Mater. Res.* 25 (2010) 1525–1531.
- [120]D. Guo, *Development of electrolytes for hybrid supercapacitors. Master thesis, 2017.*
- [121]P.W. Ruch, D. Cericola, M. Hahn, R. Kötz, A. Wokaun, *Journal of Electroanalytical Chemistry* 636 (2009) 128–131.
- [122]N. Jäckel, D. Weingarth, A. Schreiber, B. Krüner, M. Zeiger, A. Tolosa, M. Aslan, V. Presser, *Electrochimica Acta* 191 (2016) 284–298.
- [123]M. Hahn, O. Barbieri, F.P. Campana, R. Kötz, R. Gallay, *Appl. Phys. A* 82 (2006) 633–638.
- [124]P.W. Ruch, D. Cericola, A. Foelske-Schmitz, R. Kötz, A. Wokaun, *Electrochimica Acta* 55 (2010) 4412–4420.
- [125]P.W. Ruch, D. Cericola, A. Foelske, R. Kötz, A. Wokaun, *Electrochimica Acta* 55 (2010) 2352–2357.
- [126]D. Weingarth, H. Noh, A. Foelske-Schmitz, A. Wokaun, R. Kötz, *Electrochimica Acta* 103 (2013) 119–124.
- [127]Abbos Shodiev, *Development of the positive electrode of hybrid supercapacitors. Master thesis, 2017.*
- [128]Parviz Hajiyev, *Electrochemical stability of hybrid supercapacitor active materials. Master thesis, 2016.*

Curriculum Vitae

Mathias Widmaier

- Date of birth 06.07.1987
- Nationality German
- Family status Unmarried



Professional experience

02/2015-05/2018 PhD thesis on the subject "*Improvement of hybrid supercapacitors by optimization of electrode design and material properties*", Robert Bosch GmbH and Saarland University

Education

01/2012-12/2014 Master of Science in Materials Science at the University of Stuttgart
Master thesis: "*Development of hybrid supercapacitors*", Robert Bosch GmbH

10/2008-12/2011 Bachelor of Science in Materials Science at the University of Stuttgart
Bachelor thesis: "*Single crystal silicon windows for transmission electron microscopic study of epitaxial metal layers*", Max-Planck-Institute for Metals Research

07/2007 German High School Diploma, Gottlieb-Daimler-Schule 1 in Sindelfingen, Germany

Military Service

10/2007-06/2008

Conscript, Allgäu-Kaserne Füssen (Germany)

Supervision

- 2018 Master thesis (Synthesis and characterization of a new anode material for hybrid supercapacitors, K. Pfeifer)
- 2017 Master thesis (Development of electrolytes for hybrid supercapacitors, D. Guo)
- 2017 Master thesis (Development of the positive electrode of hybrid supercapacitors, A. Shodiev)
- 2017 Master thesis (Influence of the electrode structure on different scaled hybrid supercapacitors, C. Barras)
- 2016 Internship (Development of a high power energy storage device, M. Abuzarli)
- 2016 Internship (Development of high temperature hybrid supercapacitors, Y. C. Chien)
- 2016 Master thesis (Electrochemical stability of hybrid supercapacitor active materials, P. Hajiyev)
- 2016 Master thesis (Development of a high temperature stable hybrid supercapacitor, T. Schonhardt)
- 2016 Master thesis (Understanding and optimization of the hybrid supercapacitor microstructure, S. Hahn)

Scientific contributions

- Publication: *“Valence-Tuned Lithium Titanate Nanopowder for High-Rate Electrochemical Energy Storage”*
M. Widmaier, K. Pfeifer, L. Bommer, and V. Presser
Batteries & Supercaps (2018) DOI:10.1002/batt.201700007
- Publication: *“Continuous Silicon Oxycarbide Fiber Mats with Tin Nanoparticles as High Capacity Anode for Lithium-Ion Batteries”*
A. Tolosa, **M. Widmaier**, B. Krüner, J. M. Griffin, and V. Presser
Sustainable Energy Fuels 2 (2018) 215
- Publication: *“Influence of Carbon Distribution on the Electrochemical Performance and Stability of Lithium Titanate Based Energy Storage Devices”*
M. Widmaier, N. Jäckel, M. Zeiger, M. Abuzarli, C. Engel, L. Bommer, and V. Presser
Electrochimica Acta 247 (2017) 1006
- Publication: *“Tuning Pseudocapacitive and Battery-Like Lithium Intercalation in Vanadium Dioxide/Carbon Onion Hybrids for Asymmetric Supercapacitor Anodes”*
S. Fleischmann, M. Zeiger, N. Jäckel, B. Krüner, V. Lemkova, **M. Widmaier**, and V. Presser
Journal of Material Chemistry A 5 (2017) 13039
- Publication: *“Porous Carbon as Quasi-Reference Electrode in Aqueous Electrolytes”*
J. Lee, N. Jäckel, D. Kim, **M. Widmaier**, S. Sathyamoorthi, P. Srimuk, C. Kim, S. Fleischmann, M. Zeiger, and V. Presser
Electrochimica Acta 222 (2016) 1800

- Publication: “*Carbon as Quasi-Reference Electrode in Unconventional Lithium-Salt Containing Electrolytes for Hybrid Battery/Supercapacitor Devices*”
M. Widmaier, B. Krüner, N. Jäckel, M. Aslan, S. Fleischmann, C. Engel, and V. Presser
Journal of The Electrochemical Society 163 (2016) A2956

- Conference talk: “*Activated Carbon Based Quasi-Reference Electrodes For Unconventional Lithium-Salt Containing Organic Electrolytes*”
M. Widmaier, B. Krüner, N. Jäckel, M. Aslan, S. Fleischmann, C. Engel, and V. Presser
231st ECS Meeting, New Orleans, 2017

- Several patent applications about cell chemistry and applications of batteries, supercapacitors, and hybrid supercapacitors